Volume 4, Issue 2, 2018

Journal of Biomedical Photonics & Engineering

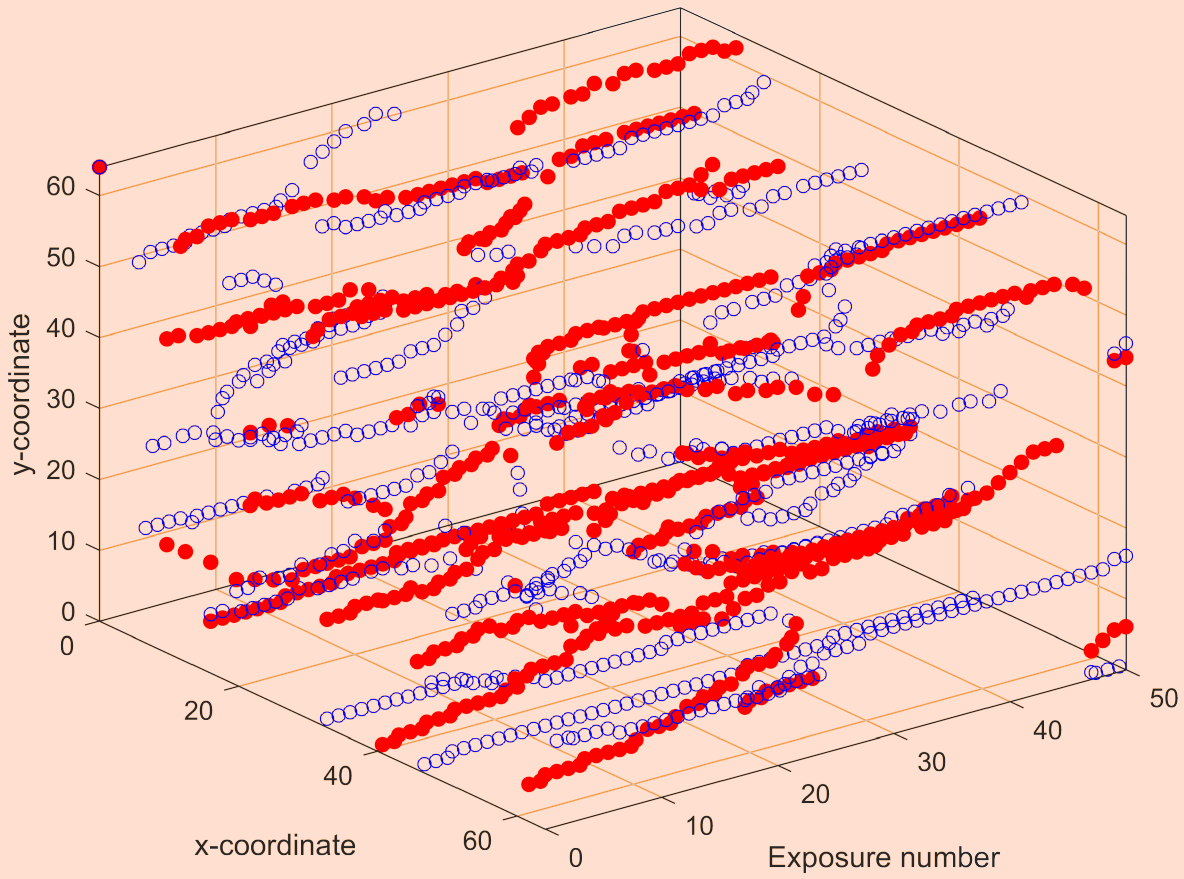

 doi: 10.18287/JBPE18.04.020001

Journal of Biomedical Photonics & Engineering

by Samara National Research University

Volume 4, Issue 2 (June 2018)

Editorial Board

Used Figure from this issue on the Cover

A. Majumdar, S.J. Kirkpatrick Statistical studies on optical vortices in dynamic speckle fields, 020301, Fig. 3a.

Postal address:
39B Lukacheva st., room #301
Samara 443086, Russian Federation

Contents

Optical and structural properties of biological tissues under diabetes mellitus

Daria K. Tuchina[1,2*] and Valery V. Tuchin[1,3,4]

[1] Saratov State University, 83 Astrakhanskaya Str., Saratov 410012, Russia
[2] Tomsk State University, 36 Prosp. Lenina, Tomsk 634050, Russia
[3] Samara National Research University, 34 Moskovskoye Shosse, Samara 443086, Russia
[4] Laboratory of Laser Diagnostics of Technical and Living Systems, Institute of Precision Mechanics and Control, Russian Academy of Sciences, 24 Rabochaya Str., Saratov 410028, Russia

*** e-mail:** tuchinadk@mail.ru

Abstract. Diabetes mellitus is a serious social and economic problem of modern society because it is widespread and fraught with numerous complications. Therefore, it is necessary to search for new methods of diabetes mellitus diagnostics and treatment and to improve the existing ones, which, in turn, requires thorough investigation of the disease development mechanisms, as well as elaboration of simple and reliable methods and criteria for detecting the complication precursors. In connection with the solution of these problems, in the paper we present an analytical review of recent publications devoted to the study of the changes of structural and optical properties of biological tissues under the conditions of diabetes mellitus development using *in vitro* models of glycated tissues, *in vivo* experimental models of diabetes in laboratory animals, and clinical studies. © 2018 Journal of Biomedical Photonics & Engineering.

Keywords: diabetes mellitus; protein glycation; tissues; skin; myocardium; cardiovascular system; optical properties; diffusion of metabolites.

Paper #3284 received 14 Mar 2018; revised manuscript received 16 May 2018; accepted for publication 11 Jun 2018; published online 29 Jun 2018. doi: 10.18287/JBPE18.04.020201.

References

1. J. E. Shaw, R. A. Sicree, and P. Z. Zimmet, "Global estimates of the prevalence of diabetes for 2010 and 2030," Diabetes Research and Clinical Practice 87, 4–14 (2010).
2. Diabetes Fact Sheet, World Health Organization (2017).
3. C. D. Mathers, D. Loncar, "Projections of Global Mortality and Burden of Disease from 2002 to 2030," PLoS Medicine 3(11), e442 (2006).
4. D. LeRoith, S. I. Taylor, and J. M. Olefsky (Eds.), Diabetes Mellitus: A Fundamental and Clinical Text, 3rd edition, Lippincott Williams & Wilkins (2004).
5. K. T. Patton, G. A. Thibodeau, The Human Body in Health & Disease, 6th Edition, Elsevier Inc. (2014).
6. D. G. Gardner, D. M. Shoback, Greenspan's Basic & Clinical Endocrinology, 9th Edition, McGraw-Hill Medical, NY (2011).
7. B. B. Tripathy, RSSDI Textbook of Diabetes Mellitus, 2nd Edition, Jaypee Brothers Medical Publishers, New Delhi (2012).
8. Diabetes Care, Volume 40, Supplement 1, American Diabetes Association Inc. (2017).
9. A. J. King, "The use of animal models in diabetes research," British Journal of Pharmacology 166, 877–894 (2012).
10. T. Szkudelski, "The mechanism of alloxan and streptozotocin action in B cells of the rat pancreas," Physiological Research 50(6), 537–546 (2001).
11. S. Lenzen, "The mechanisms of alloxan- and streptozotocin-induced diabetes," Diabetologia 51, 216–226 (2008).
12. A. Burgeiro, A. Fuhrmann, S. Cherian, D. Espinoza, I. Jarak, R. A. Carvalho, M. Loureiro, M. Patrício, M. Antunes, and E. Carvalho, "Glucose uptake and lipid metabolism are impaired in epicardial adipose tissue

from heart failure patients with or without diabetes," American Journal of Physiology-Endocrinology and Metabolism 310(7), E550–E564 (2016).
13. V. Vinokur, G. Leibowitz, L. Grinberg, R. Eliashar, E. Berenshtein, and M. Chevion, "Diabetes and the heart: could the diabetic myocardium be protected by preconditioning?" Redox Report 12(6), 246–256 (2007).
14. T. Nishikawa, D. Edelstein, X. L. Du, S. Yamagishi, T. Matsumura, Y. Kaneda, M. A. Yorek, D. Beebe, P. J. Oates, H. P. Hammes, I. Giardino, and M. Brownlee, "Normalizing mitochondrial superoxide production blocks three pathways of hyperglycemic damage," Nature 404(6779), 787–790 (2000).
15. X. Du, T. Matsumura, D. Edelstein, D. Edelstein, L. Rossetti, Z. Zsengellér, C. Szabó, and M. Brownlee, "Inhibition of GAPDH activity by poly(ADP-ribose) polymerase activates three major pathways of hyperglycemic damage in endothelial cells," Journal of Clinical Investigation 112(7), 1049–1057 (2003).
16. M. Chevion, "A site-specific mechanism for free radical induced biological damage: the essential role of redox-active transition metals," Free Radical Biology and Medicine 5(1), 27–37 (1988).
17. N. Vigneshwaran, G. Bijukumar, N. Karmakar, S. Anand, and A. Misra, "Autofluorescence characterization of advanced glycation end products of hemoglobin," Spectrochimica Acta Part A: Molecular and Biomolecular Spectroscopy 61(1–2), 163–170, (2005).
18. N. I. Dikht, A. B. Bucharskaya, G. S. Terentyuk, G. N. Maslyakova, O. V. Matveeva, N. A. Navolokin, N. G. Khlebtsov, and B. N. Khlebtsov, "Morphological study of the internal organs in rats with alloxan diabetes and transplanted liver tumor after intravenous injectin of gold nanorods," Russian Open Medical Journal 3(3), 0301 (2014).
19. D. McGuire, N. Marx, Diabetes in Cardiovascular Disease: A Companion to Braunwald's Heart Disease, Elsevier Health Sciences (2014).
20. V. V. Tuchin (Ed.), Handbook of Optical Sensing of Glucose in Biological Fluids and Tissues, Taylor & Francis Group LLC, CRC Press (2009).
21. H. Ullah, A. Mariampillai, M. Ikram, and I. A. Vitkin, "Can Temporal Analysis of Optical Coherence Tomography Statistics Report on Dextrorotatory-Glucose Levels in Blood?" Laser Physics 21(11), 1962–1971 (2011).
22. G. Purvinis, B. D. Cameron, and D. M. Altrogge, "Noninvasive polarimetric-based glucose monitoring: an in vivo study," Journal of Diabetes Science and Technology 5(2), 380–387 (2011).
23. N. C. Dingari, I. Barman, G. P. Singh, J. W. Kang, R. R. Dasari, and M. S. Feld, "Investigation of the specificity of Raman spectroscopy in non-invasive blood glucose measurements," Analytical and Bioanalytical Chemistry 400(9), 2871–2880 (2011).
24. Y. Zhang, G. Wu, H. Wei, Z. Guo, H. Yang, Y. He, S. Xie, and Y. Liu, "Continuous noninvasive monitoring of changes in human skin optical properties during oral intake of different sugars with optical coherence tomography," Biomedical Optics Express 5(4), 990–999 (2014).
25. R. Y. He, H. J. Wei, H. M. Gu, Z. G. Zhu, Y. Q. Zhang, X. Guo, and T. Cai, "Effects of optical clearing agents on noninvasive blood glucose monitoring with optical coherence tomography: a pilot study," Journal of Biomedical Optics 17(10), 101513 (2012).
26. M. A. Pleitez, T. Lieblein, A. Bauer, O. Hertzberg, H. von Lilienfeld-Toal, and W. Mäntele, "Windowless ultrasound photoacoustic cell for in vivo mid-IR spectroscopy of human epidermis: Low interference by changes of air pressure, temperature, and humidity caused by skin contact opens the possibility for a non-invasive monitoring of glucose in the interstitial fluid," Review of Scientific Instruments 84(8), 084901 (2013).
27. N. C. Dingari, I. Barman, J. W. Kang, C. R. Kong, R. R. Dasari, and M. S. Feld, "Wavelength selection-based nonlinear calibration for transcutaneous blood glucose sensing using Raman spectroscopy," Journal of Biomedical Optics 16(8), 087009 (2011).
28. J. M. Yuen, N. C. Shah, J. T. Walsh, M. R. Glucksberg, and R. P. Van Duyne, "Transcutaneous glucose sensing by surface-enhanced spatially offset Raman spectroscopy in a rat model," Analytical Chemistry 82(20), 8382–8385 (2010).
29. S. Firdous, M. Nawaz, M. Ahmed, S. Anwar, A. Rehman, R. Rashid, and A. Mahmood, "Measurement of diabetic sugar concentration in human blood using Raman spectroscopy," Laser physics 22(6), 1090–1094 (2012).
30. X. X. Guo, A. Mandelis, and B. Zinman, "Noninvasive glucose detection in human skin using wavelength modulated differential laser photothermal radiometry," Biomedical Optics Express 3(11), 3012–3021 (2012).
31. S. A. A. Shah, A. Laude, I. Faye, and T. B. Tang, "Automated microaneurysm detection in diabetic retinopathy using curvelet transform," Journal of Biomedical Optics 21(10), 101404 (2016).
32. Y. J. Heo, S. Takeuchi, "Towards smart tattoos: implantable biosensors for continuous glucose monitoring," Advanced Healthcare Materials 2(1), 43–56 (2013).
33. E. Selvin, M. W. Steffes, H. Zhu, K. Matsushita, L. Wagenknecht, J. Pankow, J. Coresh, and F. L. Brancati, "Glycated Hemoglobin, Diabetes, and Cardiovascular Risk in Nondiabetic Adults," The New England Journal of Medicine 362(9), 800–811 (2010).

34. J.-Y. Tseng, A. A. Ghazaryan, W. Lo, Y.-F. Chen, V. Hovhannisyan, S.-J. Chen, H.-Y. Tan, and C.-Y. Dong, "Multiphoton spectral microscopy for imaging and quantification of tissue glycation," Biomedical Optics Express 2(2), 218–230 (2011).
35. G. Mazarevica, T. Freivalds, and A. Jurka, "Properties of erythrocyte light refraction in diabetic patients," Journal of Biomedical Optics 7(2), 244–247 (2002).
36. J. Blackwell, K. M. Katika, L. Pilon, K. M. Dipple, S. R. Levin, and A. Nouvong, "In vivo time-resolved autofluorescence measurements to test for glycation of human skin," Journal of Biomedical Optics 13(1), 014004 (2008).
37. U. Kanska, J. Boratynski, "Thermal glycation of proteins by D-glucose and D-fructose," Archivum Immunologiae et Therapiae Experimentalis 50(1), 61–66 (2002).
38. O. S. Khalil, "Non-Invasive Glucose Measurement Technologies: An Update from 1999 to the Dawn of the New Millennium," Diabetes Technology & Therapeutics 6(5), 660–697 (2004).
39. D. K. Tuchina, R. Shi, A. N. Bashkatov, E. A. Genina, D. Zhu, Q. Luo, and V. V. Tuchin, "Ex vivo optical measurements of glucose diffusion kinetics in native and diabetic mouse skin," Journal of Biophotonics 8(4), 332-346 (2015).
40. D. K. Tuchina, A. N. Bashkatov, A. B. Bucharskaya, E. A. Genina, and V. V. Tuchin, "Study of glycerol diffusion in skin and myocardium ex vivo under the conditions of developing alloxan-induced diabetes," Journal of Biomedical Photonics & Engineering 3(2), 020302 (2017).
41. T. Pan, M. Li, J. Chen, and H. Xue, "Quantification of glycated hemoglobin indicator HbA1c through near-infrared spectroscopy," Journal of Innovative Optical Health Sciences 7(4), 1350060 (2014).
42. E. Shirshin, O. Cherkasova, T. Tikhonova, E. Berlovskaya, A. Priezzhev, and V. Fadeev, "Native fluorescence spectroscopy of blood plasma of rats with experimental diabetes: identifying fingerprints of glucose-related metabolic pathways," Journal of Biomedical Optics 20(5), 051033 (2015).
43. G. V. Maksimov, O. G. Luneva, N. V. Maksimova, E. Matettuchi, E. A. Medvedev, V. Z. Pashchenko, and A. B. Rubin. "Role of viscosity and permeability of the erythrocyte plasma membrane in changes in oxygen-binding properties of hemoglobin during diabetes mellitus," Bulletin of Experimental Biology and Medicine, 140(5), 510–513 (2005).
44. J. F. Villa-Manríquez, J. Castro-Ramos, F. Gutiérrez-Delgado, M. A. Lopéz-Pacheco, and A. E. Villanueva-Luna, "Raman spectroscopy and PCA-SVM as a non-invasive diagnostic tool to identify and classify qualitatively glycated hemoglobin levels *in vivo*," Journal of Biophotonics 10(8), 1074–1079 (2016).
45. P. A. Timoshina, A. B. Bucharskaya, D. A. Alexandrov, and V. V. Tuchin, "Study of blood microcirculation of pancreas in rats with alloxan diabetes by Laser Speckle Contrast Imaging," Journal of Biomedical Photonics & Engineering 3(2), 020301 (2017).
46. F. Wei, S. Rui, and D. Zhu, "Monitoring skin microvascular dysfunction of type 1 diabetic mice using in vivo skin optical clearing," Proceedings of SPIE 10493, 104931O (2018).
47. O. A. Smolyanskaya, I. J. Schelkanova, M. S. Kulya, E. L. Odlyanitskiy, I. S. Goryachev, A. N. Tcypkin, Y. V. Grachev, Ya. G. Toropova, and V. V. Tuchin, "Glycerol dehydration of native and diabetic animal tissues studied by THz-TDS and NMR methods," Biomedical optics express 9(3), 1198 (2018).
48. V. V. Tuchin, Optical Clearing of Tissues and Blood, PM 154, SPIE Press, Bellingham, WA (2006).
49. D. Zhu, K. V. Larin, Q. Luo, and V. V. Tuchin, "Recent progress in tissue optical clearing," Laser & Photonics Reviews 7(5), 732–757 (2013).
50. L. M. Oliveira, M. I. Carvalho, E. Nogueira, and V. V. Tuchin, "The characteristic time of glucose diffusion measured for muscle tissue at optical clearing," Laser Physics 23(7), 075606 (2013).
51. L. Oliveira, M. I. Carvalho, E. Nogueira, and V. V. Tuchin, "Optical measurement of rat muscle samples under treatment with ethylene glycol and glucose," Journal of Innovative Optical Health Sciences 6(2), 1350012 (2013).
52. M. G. Ghosn, N. Sudheendran, M. Wendt, A. Glasser, V. V. Tuchin, and K. V. Larin, "Monitoring of glucose permeability in monkey skin in vivo using Optical Coherence Tomography," Journal of Biophotonics 3(1–2), 25–33 (2010).
53. A. N. Bashkatov, E. A. Genina, Yu. P. Sinichkin, V. I. Kochubey, N. A. Lakodina, and V. V. Tuchin, "Glucose and mannitol diffusion in human dura mater," Biophysical Journal 85(5), 3310–3318 (2003).
54. M. Kreft, M. Luksic, T. M. Zorec, M. Prebil, and R. Zorec, "Diffusion of D–glucose measured in the cytosol of a single astrocyte," Cellular and Molecular Life Sciences 70(8), 1483–1492 (2012).
55. M. G. Ghosn, E. F. Carbajal, N. A. Befrui, and K. V. Larin, "Permeability of Hyperosmotic Agent in Normal and Atherosclerotic Vascular Tissues," Journal Of Biomedical Optics 13(1), 010505 (2008).
56. X. Guo, G. Wu, H. Wei, X. Deng, H. Yang, Y. Ji, Y. He, Z. Guo, S. Xie, H. Zhong, Q. Zhao, and Z. Zhu, "Quantification of Glucose Diffusion in Human Lung Tissues by Using Fourier Domain Optical Coherence Tomography," Photochemistry and Photobiology 88(2), 311–316 (2012).
57. F. Quondamatteo, "Skin and diabetes mellitus: what do we know?" Cell and Tissue Research 355(1), 1–21 (2014).

58. G. M. Campos de Macedo, S. Nunes, and T. Barreto, "Skin disorders in diabetes mellitus: an epidemiology and physiopathology," Diabetology & Metabolic Syndrome 8(1), 63 (2016)
59. J. A. Suaya, D. F. Eisenberg, C. Fang, and L. G. Miller, "Skin and Soft Tissue Infections and Associated Complications among Commercially Insured Patients Aged 0–64 Years with and without Diabetes in the U.S.," PLOS One 8(4), e60057 (2013).
60. M. Marre, "Genetics and the prediction of complications in type 1 diabetes," Diabetes Care 22(2), B53–B58 (1999).
61. I. J. Goldberg, "Why does diabetes increase atherosclerosis? I don't know!" Journal of Clinical Investigation 114(5), 613–615 (2004).
62. W. W. Song, A. Ergul, "Type-2 diabetes-induced changes in vascular extracellular matrix gene expression: Relation to vessel size," Cardiovascular Diabetology 5, 3 (2006).
63. G. Spinetti, N. Kraenkel, C. Emanueli, and P. Madeddu, "Diabetes and vessel wall remodelling: from mechanistic insights to regenerative therapies," Cardiovascular Research 78(2), 265–273 (2008).
64. D. Pedicino, A. F. Giglio, V. A. Galiffa, F. Trotta and G. Liuzzo, "Type 2 Diabetes, Immunity and Cardiovascular Risk: A Complex Relationship," Chap. 3 in Pathophysiology and Complications of Diabetes Mellitus, O. O. Oguntibeju (Ed.), InTech (2012).
65. M. S. Anderson, J. A. Bluestone, "The NOD mouse: a model of immune dysregulation," Annual Review of Immunology 23(1), 447–485 (2005).
66. J. A. Bluestone, K. Herold, and G. Eisenbarth, "Genetics, pathogenesis and clinical interventions in type 1 diabetes," Nature 464(7293), 1293–1300 (2010).
67. S. Makino, K. Kunimoto, Y. Muraoka, Y. Mizushima, K. Katagiri, and Y. Tochino, "Breeding of a non-obese, diabetic strain of mice," Experimental Animals 29(1), 1–13 (1980).
68. T. T. Berezov, B. F. Korovkin, Biological Chemistry, Meditsina, Moscow (1998) [in Russian].
69. B. Coudrillier, J. Pijanka, J. Jefferys, T. Sorensen, H. A. Quigley, C. Boote, and T. D. Nguyen, "Collagen Structure and Mechanical Properties of the Human Sclera: Analysis for the Effects of Age," Journal of Biomechanical Engineering 137(4), 041006 (2015).
70. M. Maciążek-Jurczyk, A. Szkudlarek, M. Chudzik, J. Pożycka, and A. Sułkowska, "Alteration of human serum albumin binding properties induced by modifications: A review," Spectrochimica Acta Part A: Molecular and Biomolecular Spectroscopy 188, 675–683 (2018).
71. S. F. Diniz, F. P. L. G. Amorim, F. F. Cavalcante-Neto, A. L. Bocca, A. C. Batista, G. E. P. M. Simm, and T. A. Silva, "Alloxan-induced diabetes delays repair in a rat model of closed tibial fracture," Brazilian Journal Of Medical and Biological Research 41(5), 373–379 (2008).
72. D. Dufrane, M. van Steenberghe, Y. Guiot, R. M. Goebbels, A. Saliez, and P. Gianello, "Streptozotocin-induced diabetes in large animals (pigs/primates): role of GLUT2 transporter and beta-cell plasticity," Transplantation 81(1), 36–45 (2006).
73. L. M. Hansen, D. Gupta, G. Joseph, D. Weiss, and W. R. Taylor, "The receptor for advanced glycation end products impairs collateral formation in both diabetic and non-diabetic mice," Laboratory Investigation 97(1), 34–42 (2017).
74. H. Yu, J. Zhen, B. Pang, J. Gu, and S. Wu, "Ginsenoside Rg1 ameliorates oxidative stress and myocardial apoptosis in streptozotocin-induced diabetic rats," Journal of Zhejiang University-SCIENCE B, 16(5), 344–354 (2015).
75. J. Wu, L. Yan, "Streptozotocin-induced type 1 diabetes in rodents as a model for studying mitochondrial mechanisms of diabetic β cell glucotoxicity," Diabetes, Metabolic Syndrome and Obesity: Targets and Therapy 8, 181–188 (2015).
76. M. I. Asrarov, M. K. Pozilov, N. A. Ergashev, and M. M. Rakhmatullaeva, "The influence of the hypoglycemic agent glycorazmulin on the functional state of mitochondria in the rats with streptozotocin-induced diabetes," Problems of Endocrinology 60(3), 38–42 (2014) [in Russian].
77. L. Dancakova, T. Vasilenko, I. Kova, K. Jakubcova, M. Holly, V. Revajova, F. Sabol, Z. Tomori, M. Iversen, P. Gal, and J. M. Bjordal, "Low-Level Laser Therapy with 810 nm Wavelength Improves Skin Wound Healing in Rats with Streptozotocin-Induced Diabetes," Photomedicine and Laser Surgery 32(4), 198–204 (2014).
78. D. E. Kelley, J. He, E. V. Menshikova, and V. B. Ritov, "Dysfunction of Mitochondria in Human Skeletal Muscle in Type 2 Diabetes," Diabetes 51(10), 2944–2950 (2002).
79. C. Moran, G. Münch, J. M. Forbes, R. Beare, L. Blizzard, A. J. Venn, T. G. Phan, J. Chen, and V. Srikanth, "Type 2 Diabetes, Skin Autofluorescence, and Brain Atrophy," Diabetes 64(1), 279–283 (2015).
80. D. Ziegler, N. Papanas, A. Zhivov, S. Allgeier, K. Winter, I. Ziegler, J. Brüggemann, A. Strom, S. Peschel, B. Köhler, O. Stachs, R. F. Guthoff, and M. Roden, "Early Detection of Nerve Fiber Loss by Corneal Confocal Microscopy and Skin Biopsy in Recently Diagnosed Type 2 Diabetes," Diabetes 63(7), 2454–2463 (2014).
81. M. F. Chowdhry, H. A. Vohra, and M. Galiñanes, "Diabetes increases apoptosis and necrosis in both ischemic and nonischemic human myocardium: Role of caspases and poly–adenosine diphosphate–ribose polymerase," The Journal of Thoracic and Cardiovascular Surgery 134(1), 124–131 (2007).

82. V. M. Monnier, D. R. Sell, C. Strauch, W. Sun, J. M. Lachin, P. A. Cleary, S. Genuth, and the DCCT Research Group, "The association between skin collagen glucosepane and past progression of microvascular and neuropathic complications in type 1 diabetes," Diabetes Complications 27(2), 141–149 (2013).
83. J. R. Acosta, I. Douag, D. P. Andersson, J. Bäckdahl, M. Rydén, P. Arner, and J. Laurencikiene, "Increased fat cell size: a major phenotype of subcutaneous white adipose tissue in non-obese individuals with type 2 diabetes," Diabetologia 59(3), 560–570 (2016).
84. E. V. Zharkikh, V. V. Dremin, M. A. Filina, I. N. Makovik, E. V. Potapova, E. A. Zherebtsov, A. I. Zherebtsova, and A. V. Dunaev, "Application of optical non-invasive methods to diagnose the state of the lower limb tissues in patients with diabetes mellitus," Journal of Physics: Conference Series 929, 012069 (2017).
85. V. Dremin, E. Zherebtsov, V. Sidorov, A. Krupatkin, I. Makovik, A. Zherebtsova, E. Zharkikh, E. Potapova, A. Dunaev, A. Doronin, A. Bykov, I. Rafailov, K. Litvinova, S. Sokolovski, and E. Rafailov, "Multimodal optical measurement for study of lower limb tissue viability in patients with diabetes mellitus," Journal of Biomedical Optics 22(8), 085003 (2017).
86. E. V. Potapova, V. V. Dremin, E. A. Zherebtsov, I. N. Makovik, E. V. Zharkikh, A. V. Dunaev, O. V. Pilipenko, V. V. Sidorov, and A. I. Krupatkin, "A complex approach to noninvasive estimation of microcirculatory tissue impairments in feet of patients with diabetes mellitus using spectroscopy," Optics and spectroscopy 123(6), 955–964 (2017).
87. L. A. Muir, C. K. Neeley, K. A. Meyer, N. A. Baker, A. M. Brosius, A. R. Washabaugh, O. A. Varban, J. F. Finks, B. F. Zamarron, C. G. Flesher, J. S. Chang, J. B. DelProposto, L. Geletka, G. Martinez-Santibanez, N. Kaciroti, C. N. Lumeng, and R. W. O'Rourke, "Adipose Tissue Fibrosis, Hypertrophy, and Hyperplasia: Correlations with Diabetes in Human Obesity," Obesity 24(3), 597–605 (2016).
88. P. Martín-Mateos, F. Dornuf, B. Duarte, B. Hils, A. Moreno-Oyervides, O. Elias Bonilla-Manrique, F. Larcher, V. Krozer, and P. Acedo, "In-vivo, non-invasive detection of hyperglycemic states in animal models using mm-wave spectroscopy," Scientific Reports 6(1), 34035 (2016).
89. A. Rohilla, S. Ali, "Alloxan Induced Diabetes: Mechanisms and Effects," International journal of research in pharmaceutical and biomedical sciences 3(2), 819–823 (2012).
90. R. Bansal, N. Ahmad, and J. R. Kidwai, "Alloxan-glucose interaction: effect on incorporation of 14C-leucine into pancreatic islets of rat," Acta Diabetologica Latina 17(2), 135–143 (1980).
91. J. H. Lee, S. H. Yang, J. M. Oh, and M. G. Lee, "Pharmacokinetics of drugs in rats with diabetes mellitus induced by alloxan or streptozocin: comparison with those in patients with type I diabetes mellitus," Journal of Pharmacy and Pharmacology 62(1), 1–23 (2010).
92. J. R. Garrett, J. Ekström, and L. C. Anderson (Eds.), Frontiers of Oral Biology: Glandular Mechanisms of Salivary Secretion, 10 (1998).
93. N. Rakieten, M. L. Rakieten, and M. V. Nadkarni, "Studies on the diabetogenic action of streptozotocin," Cancer Chemotherapy Reports 29, 91–98 (1963).
94. K. Srinivasan, P. Ramarao, "Animal models in type 2 diabetes research: an overview," Indian Journal of Medical Research 125, 451–472 (2007).
95. Y. Dekel, Y. Glucksam, I. Elron-Gross, and R. Margalit, "Insights into modeling streptozotocin-induced diabetes in ICR mice," Lab Animal 38(2), 55–60 (2009).
96. K. Hayashi, R. Kojima, and M. Ito, "Strain differences in the diabetogenic activity of streptozotocin in mice," Biological & Pharmaceutical Bulletin 29(6), 1110–1119 (2006).
97. M. Elsner, M. Tiedge, and S. Lenzen, "Mechanism underlying resistance of human pancreatic beta cells against toxicity of streptozotocin and alloxan," Diabetologia 46(12), 1713–1714 (2003).
98. Y. Yang, P. Santamaria, "Lessons on autoimmune diabetes from animal models," Clinical Science 110(6), 627–639 (2006).
99. T. Hanafusa, J. Miyagawa, H. Nakajima, K. Tomita, M. Kuwajima, Y. Matsuzawa, and S. Tarui, "The NOD mouse," Diabetes Research and Clinical Practice 24, S307–S311 (1994).
100. J. P. Mordes, R. Bortell, E. P. Blankenhorn, A. A. Rossini, and D. L. Greiner, "Rat models of type 1 diabetes: genetics, environment, and autoimmunity," ILAR Journal 45(3), 278–291 (2004).
101. X. Wang, D. C. DuBois, S. Sukumaran, V. Ayyar, W. J. Jusko, and R. R Almon, "Variability in Zucker diabetic fatty rats: differences in disease progression in hyperglycemic and normoglycemic animals," Diabetes, Metabolic Syndrome and Obesity: Targets and Therapy 7, 531–541 (2014).
102. S. Yoshida, H. Tanaka, H. Oshima, T. Yamazaki, Y. Yonetoku, T. Ohishi, T. Matsui, and M. Shibasaki, "AS1907417, a novel GPR119 agonist, as an insulinotropic and beta-cell preservative agent for the treatment of type 2 diabetes," Biochemical and Biophysical Research Communications 400(4), 745–751 (2010).
103. V. A. Gault, B. D. Kerr, P. Harriott, and P. R. Flatt, "Administration of an acylated GLP-1 and GIP preparation provides added beneficial glucose-lowering and insulinotropic actions over single incretins in mice with Type 2 diabetes and obesity," Clinical Science 121(3), 107–117 (2011).

104. J. S. Park, S. D. Rhee, N. S. Kang, W. H. Jung, H. Y. Kim, J. H. Kim, S. K. Kang, H. G. Cheon, J. H. Ahn, and K. Y. Kim, "Anti-diabetic and anti-adipogenic effects of a novel selective 11beta-hydroxysteroid dehydrogenase type 1 inhibitor, 2-(3-benzoyl)-4-hydroxy-1,1-dioxo-2H-1,2-benzothiazine-2-yl-1-phenylethanone (KR-66344)," Biochemical Pharmacology 81(8), 1028–1035 (2011).
105. P. Lindstrom, "The physiology of obese-hyperglycemic mice [ob/ob mice]," Scientific world journal 7, 666–685 (2007).
106. T. Bock, B. Pakkenberg, and K. Buschard, "Increased islet volume but unchanged islet number in ob/ob mice," Diabetes 52(7), 1716–1722 (2003).
107. F. F. Chehab, M. E. Lim, and R. Lu, "Correction of the sterility defect in homozygous obese female mice by treatment with the human recombinant leptin," Nature Genetics 12(3), 318–320 (1996).
108. H. Chen, O. Charlat, L. A. Tartaglia, E. A. Woolf, X. Weng, S. J. Ellis, N. D. Lakey, J. Culpepper, K. J. More, R. E. Breitbart, G. M. Duyk, R. I. Tepper, and J. P. Morgenstern, "Evidence that the diabetes gene encodes the leptin receptor: identification of a mutation in the leptin receptor gene in db/db mice," Cell 84(3), 491–495 (1996).
109. A. Pick, J. Clark, C. Kubstrup, M. Levisetti, W. Pugh, S. Bonner-Weir, and K. S. Polonsky, "Role of apoptosis in failure of beta-cell mass compensation for insulin resistance and beta-cell defects in the male Zucker diabetic fatty rat," Diabetes 47(3), 358–364 (1998).
110. T. Shibata, S. Takeuchi, S. Yokota, K. Kakimoto, F. Yonemori, and K. Wakitani, "Effects of peroxisome proliferator-activated receptor-alpha and -gamma agonist, JTT-501, on diabetic complications in Zucker diabetic fatty rats," British Journal of Pharmacology 130(3), 495–504 (2000).
111. V. M. Monnier, D. R. Sell, "Prevention and repair of protein damage by the Maillard reaction in vivo," Rejuvenation Research 9(2), 264-273 (2006).
112. Q. A. Kleter, J. J. M. Damen, M. J. Buijs, and J. M. Ten Cate, "The Maillard reaction in demineralized dentin *in vitro*," European Journal of Oral Sciences 105(3), 278-284 (1997).
113. A. Ioannou, C. Varotsis, "Modifications of hemoglobin and myoglobin by Maillard reaction products (MRPs)," PLoS ONE 12(11), e0188095 (2017).
114. R. D. G. Leslie, D. C. Robbins (Eds.), Diabetes: Clinical Science in Practice, Cambridge University Press (1995).
115. A. M. Schmidt, O. Hori, J. X. Chen, J. F. Li, J. Crandall, J. Zhang, R. Cao, S. D. Yan, J. Brett, and D. Stem, "Advanced Glycation Endproducts Interacting with Their Endothelial Receptor Induce Expression of Vascular Cell Adhesion Molecule-1 (VCAM-1) in Cultured Human Endothelial Cells and in Mice. A Potential Mechanism for the Accelerated Vasculopathy of Diabetes," Journal of Clinical Investigation 96, 1395–1403 (1995).
116. J. Kinnunen, H. T. Kokkonen, V. Kovanen, M. Hauta-Kasari, P. Vahimaa, M. J. Lammi, J. Töyräs, and J. S. Jurvelinb, "Nondestructive fluorescence-based quantification of threose-induced collagen cross-linking in bovine articular cartilage," Journal of Biomedical Optics 17(9), 0970031 (2012).
117. G. T. Wondrak, M. J. Roberts, D. Cervantes-Laurean, M. K. Jacobson, and E. L. Jacobson, "Proteins of the extracellular matrix are sensitizers of photo-oxidative stress in human skin cells," Journal of Investigative Dermatology 121(3), 578–586 (2003).
118. M. Yokota, Y. Tokudome, "The Effect of Glycation on Epidermal Lipid Content, Its Metabolism and Change in Barrier Function," Skin Pharmacology and Physiology 29(5), 231–242 (2016).
119. E. L. Hull, M. N. Ediger, A. N. T. Unione, E. K. Deemer, M. L. Stroman, and J. W. Baynes, "Noninvasive, optical detection of diabetes: model studies with porcine skin," Optics Express 12(19), 4496–4510 (2004).
120. V. M. Monnier, W. Sun, X. Gao, D. R Sell, P. A. Cleary, J. M. Lachin, S. Genuth, and The DCCT/EDIC Research Group, "Skin collagen advanced glycation endproducts (AGEs) and the long- term progression of sub- clinical cardiovascular disease in type 1 diabetes," Cardiovascular Diabetology 14, 118 (2015).
121. S. Genuth, W. Sun, P. Cleary, X. Gao, D. R. Sell, J. Lachin, and V. M. Monnier, "Skin Advanced Glycation End Products Glucosepane and Methylglyoxal Hydroimidazolone Are Independently Associated With Long-term Microvascular Complication Progression of Type 1 Diabetes," Diabetes 64(1), 266–278 (2015).
122. O. S. Zhernovaya, V. V. Tuchin, and I. V. Meglinski, "Monitoring of blood proteins glycation," Laser Physics Letters 5(6), 460–464 (2008).
123. B.-M. Kim, J. Eichler, K. M. Reiser, A. M. Rubenchik, and L. B. Da Silvam, "Collagen structure and nonlinear susceptibility: effects of heat, glycation, and enzymatic cleavage on second harmonic signal intensity," Lasers in Surgery and Medicine 27(4), 329–335 (2000).
124. B. Gopalkrishnapillai, V. Nadanathangam, N. Karmakar, S. Anand, and A. Misra, "Evaluation of autofluorescent property of hemoglobin-advanced glycation end product as a long-term glycemic index of diabetes," Diabetes 52(4), 1041–1046 (2003).
125. Y.-J. Hwang, J. Granelli, and J. Lyubovitsky, "Multiphoton optical image guided spectroscopy method for characterization of collagen-based materials modified by glycation," Analytical Chemistry 83(1), 200–206 (2011).

126. P. A. Cleary, B. H. Braffett, T. Orchard, T. J. Lyons, J. Maynard, C. Cowie, R. A. Gubitosi-Klug, J. Way, K. Anderson, A. Barnie, and S. Villavicencio, "Clinical and Technical Factors Associated with Skin Intrinsic Fluorescence in Subjects with Type 1 Diabetes from the Diabetes Control and Complications Trial/Epidemiology of Diabetes Interventions and Complications Study," Diabetes Technology & Therapeutics 15(6), 466–474 (2013).
127. E. Sugisawa, J. Miura, Y. Iwamoto, and Y. Uchigata, "Skin Autofluorescence Reflects Integration of Past Long-Term Glycemic Control in Patients With Type 1 Diabetes," Diabetes Care 36(8), 2339–2345 (2013).
128. J. D. Maynard, M. N. Ediger, R. D Johnson, and M. R. Robinson, Determination of a measure of a glycation end-product or disease state using a flexible probe to determine tissue fluorescence of various sites, Patent US11677498 USA, MPK A61B 6/00, Assignee: VeraLight, Inc., Albuquerque, NM (US), Appl. No.: 11/677,498 (2012).
129. J. Lin, J. Lin, Z. Huang, P. Lu, J. Wang, X. Wang, and R. Chen, "Raman spectroscopy of human hemoglobin for diabetes detection," Journal of Innovative Optical Health Sciences 7(1), 1350051 (2014).
130. K. Sangkyu, L. Joonhyung, Noninvasive apparatus and method for testing glycated hemoglobin, Patent 9841415, Assignee: Samsung Electronics Co., Ltd. (Suwon-si, KR), United States (2017).
131. M. Mallya, R. Shenoy, G. Kodyalamoole, M. Biswas, J. Karumathil, and S. Kamath, "Absorption Spectroscopy for the Estimation of Glycated Hemoglobin (HbA1c) for the Diagnosis and Management of Diabetes Mellitus: A Pilot Study," Photomedicine and Laser Surgery 31(5), 219–224 (2013).
132. T. Pan, M. Li, J. Chen, and H. Xue, "Quantification of glycated hemoglobin indicator HbA1c through near-infrared spectroscopy," Journal of Innovative Optical Health Sciences 7(4), 1350060 (2014).
133. M. Rendell, T. Bergman, G. O'Donnell, E. Drobny, J. Borgos, and R. Bonnor, "Microvascular blood flow, volume, and velocity, measured by laser Doppler techniques in IDDM," Diabetes 38(7), 819–824 (1989).
134. H. M. Raabe, H. Molsen, S.-M. Mlinaric, Y. Acil, G. H. G. Sinnecker, H. Notbohm, K. Kruse, and P. K. Muller, "Biochemical alterations in collagen IV induced by *in vitro* glycation," Biochemical Journal 319(3), 699–704 (1996).
135. O. S. Zhernovaya, A. N. Bashkatov, E. A. Genina, V. V. Tuchin, I. V. Meglinski, D. Yu. Churmakov, and L. J. Ritchie, "Investigation of glucose-hemoglobin interaction by optical coherence tomography," Proceedings of SPIE 6535, 65351C (2007).
136. E. I. Galanzha, A. V. Solovieva, V. V. Tuchin, R. K. Wang, and S. G. Proskurin, "Application of optical coherence tomography for diagnosis and measurements of glycated hemoglobin," Proceedings of SPIE 5140, 125–132 (2003).
137. V. V. Tuchin, R. K. Wang, E. I. Galanzha, J. B. Elder, and D. M. Zhestkov, "Monitoring of glycated hemoglobin by OCT measurement of refractive index," Proceedings of SPIE 5316, 66–77 (2004).
138. P. J. Higgins, H. F. Bunn, "Kinetic analysis of the nonenzymatic glycosylation of hemoglobin," The Journal of Biological Chemistry 256(10), 05204–5208 (1981).
139. G. K. Reddy, "Cross-Linking in Collagen by Nonenzymatic Glycation Increases the Matrix Stiffness in Rabbit Achilles Tendon," Experimental Diabesity Research 5(2), 143–153 (2004).
140. B. E. Sherlock, J. N. Harvestine, D. Mitra, A. Haudenschild, J. Hu, K. A. Athanasiou, J. K. Leach, and L. Marcua, "Nondestructive assessment of collagen hydrogel cross-linking using time-resolved autofluorescence imaging," Journal of Biomedical Optics 23(3), 036004 (2018)
141. M. Mernea, A. Ionescu, I. Vasile, C. Nica, G. Stoian, T. Dascalu, and D. F. Mihailescu, "In vitro human serum albumin glycation monitored by Terahertz spectroscopy," Optical and Quantum Electronics 47(4), 961–973 (2015).
142. A. Goldin, J. A. Beckman, A. M. Schmidt, and M. A. Creager, "Advanced Glycation End Products Sparking the Development of Diabetic Vascular Injury," Circulation 114(6), 597–605 (2006).
143. V. L. Emanuel, I. Yu. Karyagina, and Yu. V. Emanuel, "Comparison of method for determining glycosylated hemoglobin," Laboratornaya meditsina 5, 98–104 (2002) [in Russian].
144. V. V. Tuchin, Lasers and Fibre Optics in Biomedical Science, Fizmatlit, Moscow (2010) [in Russian].
145. V. V. Tuchin, Optics of Biological Tissues. Methods of Light Scattering in Medical Diagnostics, Fizmatlit, Moscow (2012) [in Russian].
146. J. Wang, N. Ma, R. Shi, Y. Zhang, T. Yu, and D. Zhu, "Sugar-induced skin optical clearing: from molecular dynamics simulation to experimental demonstration," IEEE Journal of Selected Topics in Quantum Electronics 20(2), 256–262 (2014).
147. E. A. Genina, A. N. Bashkatov, and V. V. Tuchin, "Tissue optical immersion clearing," Expert Review of Medical Devices 7(6), 825–842 (2010).
148. F. S. Pavone, P. J. Campagnola (Eds.), "SHG and Optical Clearing," Chap. 8 in Second Harmonic Generation Imaging, CRC Press, Taylor & Francis Group, Boca Raton, London, NY, 169−189 (2014).
149. E. A. Genina, A. N. Bashkatov, K. V. Larin, and V. V. Tuchin, "Light–Tissue Interaction at Optical Clearing," Chap. 7 in Laser Imaging and Manipulation in Cell Biology, F.S. Pavone (Ed.), Wiley-VCH Verlag GmbH & Co. KGaA, Weinheim, 113–164 (2010).

150. L. Shi, L.A. Sordillo, A. Rodriguez-Contreras, and R. Alfano, "Transmission in near-infrared optical windows for deep brain imaging," Journal of Biophotonics 9(1–2), 38–43 (2015).
151. D. C. Sordillo, L. A. Sordillo, P. P. Sordillo, and R. R. Alfano, "Fourth Near-Infrared Optical Window for Assessment of Bone and other Tissues," Proceedings of SPIE 9689, 96894J (2016).
152. L. A. Sordillo, Y. Pu, S. Pratavieira, Y. Budansky, and R. R. Alfano, "Deep optical imaging of tissue using the second and third near-infrared spectral windows," Journal of Biomedical Optics, 19(5), 056004 (2014).
153. S. Y. Lee, H. J. Park, K. Kim, Y. H. Sohn, S. Jang, and Y. K. Park, "Refractive index tomograms and dynamic membrane fluctuations of red blood cells from patients with diabetes mellitus," Scientific Reports 7(1), 1039 (2017).
154. R. M. A. Henry, P. J. Kostense, A. M. W. Spijkerman, J. M. Dekker, G. Nijpels, R. J. Heine, O. Kamp, N. Westerhof, L. M. Bouter, and C. D. A. Stehouwer, "Arterial Stiffness Increases With Deteriorating Glucose Tolerance Status," Circulation 107(16), 2089–2095 (2003).
155. E. Danese, M. Montagnana, A. Nouvenne, and G. Lippi, "Advantages and Pitfalls of Fructosamine and Glycated Albumin in the Diagnosis and Treatment of Diabetes," Journal of Diabetes Science and Technology 9(2), 169–176 (2015).
156. A. Yuen, C. Laschinger, I. Talior, W. Lee, M. Chan, J. Birek, E. W. K. Young, K. Sivagurunathan, E. Won, C. A. Simmons, and C. A. McCulloch, "Methylglyoxal-modified collagen promotes myofibroblast differentiation," Matrix Biology 29(6), 537–548 (2010).
157. A. Ghazaryan, M. Omar, G. J. Tserevelakis, and V. Ntziachristos, "Optoacoustic detection of tissue glycation," Biomedical Optics Express 6(9), 3149 (2015).
158. M. Gniadecka, O. F. Nielsen, S. Wessel, M. Heidenheim, D. H. Christensen, and H. C. Wulf, "Water and protein structure in photoaged and chronically aged skin," Journal of Investigative Dermatology 111(6), 1129–1133 (1998).
159. D. K. Tuchina, A. N. Bashkatov, E. A. Genina, and V. V. Tuchin, Biosensor for noninvasive optical monitoring of the pathology of biological tissues, Patent RF No. 2633494, MPK A61B 5/05, G01N 21/01, Patent holder: N.G. Chernyshevsky Saratov State University, Application No. 2016102046, 22.01.2016, Bul. No. 29 (2017).
160. L. M. Oliveira, M. I. Carvalho, E. M. Nogueira, and V. V. Tuchin, "Diffusion characteristics of ethylene glycol in skeletal muscle," Journal of Biomedical Optics 20(5), 051019 (2015).
161. J.-M. Andanson, K. L. A. Chan, and S. G. Kazarian, "High-throughput spectroscopic imaging applied to permeation through the skin," Applied Spectroscopy 63(5), 512–517 (2009).
162. M. J. Choi, H. I. Maibach, "Elastic vesicles as topical/transdermal drug delivery systems," International Journal of Cosmetic Science 27(4), 211–221 (2005).
163. N. Akhtar, "Vesicles: a recently developed novel carrier for enhanced topical drug delivery," Current Drug Delivery 11(1), 87–97 (2014).
164. L. C. Freitas Lima, V. Andrade Braga, M. S. França Silva, J. Campos Cruz, S. H. Sousa Santos, M. M. Oliveira Monteiro, and C. Moura Balarini, "Adipokines, diabetes and atherosclerosis: an inflammatory association," Frontiers in Physiology 6, 304 (2015).
165. D. Schweitzer, L. Deutsch, M. Klemm, S. Jentsch, M. Hammer, S. Peters, J. Haueisen, U. A. Müller, and J. Dawczynskid, "Fluorescence lifetime imaging ophthalmoscopy in type 2 diabetic patients who have no signs of diabetic retinopathy," Journal of Biomedical Optics 20(6), 061106 (2015).
166. C. Ghosh, P. Mukhopadhyay, S. Ghosh, and M. Pradhan, "Insulin sensitivity index ($ISI_{0,120}$) potentially linked to carbon isotopes of breath CO_2 for prediabetes and type 2 diabetes," Scientific Reports 5(1), 11959 (2015).
167. C.-M. Cheng, Y.-F. Chang, H.-C. Chiang, and C.-W. Chang, "Optical coherence tomography for the structural changes detection in aging skin," Proceedings of SPIE 10456, 104565B (2018).
168. D. G. Dyer, J. A. Dunn, S. R. Thorpe, K. E. Bailie, T. J. Lyons, D. R. McCance, and J. W. Baynes, "Accumulation of Maillard Reaction Products in Skin Collagen in Diabetes and Aging," Journal of Clinical Investigation 91(6), 2463 (1993).
169. S. Sakai, K. Kikuchi, J. Satoh, H. Tagami, and S. Inoue, "Functional properties of stratum corneum in patients with diabetes mellitus: similarities to senile xerosis," British Journal of Dermatology 153(2), 319–323 (2005).
170. H. Y. Park, H. J. Kim, M. Jung, C. H. Chung, R. Hasham, C. S. Park, and E. H. Choi, "A long-standing hyperglycaemic condition impairs skin barrier by accelerating skin ageing process," Experimental Dermatology 20(12), 969–974 (2011).
171. S. Sakai, Y. Endo, N. Ozawa, T. Sugawara, A. Kusaka, T. Sayo, H. Tagami, and S. Inoue, "Characteristics of the epidermis and stratum corneum of hairless mice with experimentally induced diabetes mellitus," Journal of Investigative Dermatology 120(1), 79–85 (2003).
172. K. R. Taylor, A. E. Costanzo, and J. M. Jameson, "Dysfunctional γδ T cells contribute to impaired keratinocyte homeostasis in mouse models of obesity," Journal of Investigative Dermatology 131(12), 2409–2418 (2011).

173. P. Zakharov, M. S. Talary, I. Kolm, and A. Caduff, "Full-field optical coherence tomography for the rapid estimation of epidermal thickness: study of patients with diabetes mellitus type 1," Physiological Measurement 31(2), 193–205 (2010).
174. X. Chen, W. Lin, S. Lu, T. Xie, G. Kui, Y. Shi, J. Zou, Z. Liu, and W. Liao, "Mechanisitic study of endogenous skin lesions in diabetic rats," Experimental Dermatology 19(12), 1088–1095 (2010).
175. U. Bertheim, A. Engstorm-Laurent, P. Hofer, P. Hallgren, J. Asplund, and S. Hellstrom, "Loss of hyaluronan in the basement membrane zone of the skin correlates to the degree of stiff hands in diabetic patients," Acta Dermato-Venereologica 82(5), 329–334 (2002).
176. J. G. B. Derraik, M. Rademaker, W. S. Cutfield, T. E. Pinto, S. Tregurtha, A. Faherty, J. M. Peart, P. L. Drury, and P. L. Hofman, "Effects of Age, Gender, BMI, and Anatomical Site on Skin Thickness in Children and Adults with Diabetes," PLoS ONE 9(1), e86637 (2014).
177. A. A. Tahrani, W. Zeng, J. Sakher, M. K. Piya, S. Hughes, K. Dubb, and M. J. Stevens, "Cutaneous structural and biochemical correlates of foot complications in high-risk diabetes," Diabetes Care 35(9), 1913–1918 (2012).
178. N. C. Avery, A. J. Bailey, "The effects of the Maillard reaction on the physical properties and cell interactions of collagen," Pathologie Biologie 54(7), 387–395 (2006).
179. A. J. Argyropoulos, P. Robichaud, R. M. Balimunkwe, G. J. Fisher, C. Hammerberg, Y. Yan, and T. Quan, "Alterations of Dermal Connective Tissue Collagen in Diabetes: Molecular Basis of Aged-Appearing Skin," PLoS ONE 11(4), e0153806 (2016).
180. L. V. Wang (Ed.), Photoacoustic Imaging and Spectroscopy, CRC Press (2009).

Contents

1 Introduction

Diabetes mellitus is a chronic endocrine diseasecaused by the increased content of free glucose in organism, which results in the violation of metabolism in the organism. According to the prognosis of the World Health Organisation, the diabetes mellitus will move from the eighth to the seventh position in the list of the most widespread causes of death, the mortality growth in 2030 compared to 2010 amounting to 54% [1]. The numbers of patients suffering from diabetes mellitus has grown by approximately four times from 1980 (108 million people) to 2014 (422 million people) [2, 3].

The normal content of free glucose (glycaemia) in blood amounts to 3.3–5.5 mmol/l (60–100 mg/dl) [4]. The glucose is a monosaccharide that plays an important role in the functioning of a living organism. It is a source of energy providing metabolic processes in the organism. To regulate the glucose metabolism, the pancreas beta cells produce the peptide hormone insulin. The insufficient insulin production by the pancreas, or the abnormal reaction of the organism cells to the produced insulin, leads to the excess glucose content in the blood. Long-term increase of the glucose content in blood (above 11 mmol/l (200 mg/dl)) (hyperglycemia) leads to excess glucose content in the interstitial fluid, which violates the metabolism in the organism, causing the development of diabetes mellitus [2, 5-12].

It was supposed that the hyperglycemia could lead to increased oxidation of glucose and formation of superoxide radicals in mitochondria [13-15]. Anions of superoxide radicals are benign and nonreactive chemical substances, however, under some conditions, mainly in the presence of reductive-oxidative transition metals, such as iron and copper, they turn into highly reactive free radicals [13, 16]. The transformation occurs via metal-mediated Haber-Weiss or Fenton reactions (Eqs. (1) and (2), respectively) [13]:

$$O_2^{\cdot-} + H_2O_2 \xrightarrow{Fe/Cu} O_2 + HO^- + HO^{\cdot} \quad (1)$$

$$Fe^{2+}/Cu^{+} + H_2O_2 \rightarrow Fe^{3+}/Cu^{2+} + HO^- + HO^{\cdot} \quad (2)$$

For example, the hyperglycemia-induced overproduction of superoxide activates the hyperglycemic damage in endothelium cells of aorta. The damaging effect of superoxide leads to the redirection of glucose metabolism from the glycolytic path to alternative metabolic paths, including the formation of the advanced glycation end products.

Since the glucose level in blood is related to its level in the interstitial fluid, the hyperglycemia facilitates the metabolic disbalance and disturbance of the organs functioning [12, 17-19]. In this connection, many papers are aimed at determining the concentration of free glucose in blood, interstitial fluid, and other fluids of the body [20-30], revealing the morphological changes in vital organs [10, 12, 17, 31], designing biosensors for permanent monitoring of free glucose in the organism [20, 32], studying the effect of glucose on blood and proteins of tissues, developing the methods for diabetes monitoring based on the difference of optical properties between healthy and diabetic tissues [17, 20, 33-48],

assessing the glucose diffusion rate in healthy [20, 48-54] and pathological tissues (the walls of atherosclerotic blood vessels [48,55] and malignant tumours [56]).

One third of all patients with diabetes mellitus have complications in the form of skin lesions, the most severe of them being the chronic ulcers that recover very slowly, thus increasing the risk of infection [19, 57-59]. Diabetes mellitus increases the risk of cardiovascular diseases, retinopathy that leads to blindness, neuropathy and nephropathy [8-13, 19, 31, 60-64]. According to the data of the World Health Organisation, diabetes mellitus is the main cause of heart attacks, myocardial infarction, brain stroke, blindness, renal failure, and amputation of lower extremities, i.e., a risk factor of many other diseases enhanced by the diabetes [9, 13, 19, 60, 63, 64].

Thus, diabetes mellitus is a cause of serious complications that should be prevented by inventing new methods of diabetes diagnostics and treatment and improving the existing ones, which requires careful examination of the disease development mechanisms, as well as developing simple and reliable methods and criteria for detecting the complication precursors.

The clinical course and complications of diabetes mellitus are widely studied using different physical methods, including the optical ones, which often allow a noninvasive monitoring of the key parameters of biological tissues in real time. The latter explains why the optical methods are considered as promising in medicine and the field of their application permanently expands. This paper presents a review of recent publications on the study of the changes of structural and optical properties under the development of diabetes mellitus using *in vitro* models of glycated tissues, *in vivo* experimental models of diabetes in laboratory animals, and clinical studies. Such analysis seems to be useful for further research and engineering activity in the field of noninvasive optical diagnostics of pathological conditions in human organism.

2 Classification of diabetes mellitus

Diabetes mellitus can be divided into two principal types: type I is the insulin-dependent diabetes ("diabetes of young", "immune-mediated diabetes"), type II is the insulin-independent diabetes ("diabetes of aged") [8, 9, 19, 57]. They separately consider the gestational diabetes mellitus, diagnosed during pregnancy and not observed before it. One can also select specific types of the disease due to other causes. The examples include the monogenic diabetes syndrome, which is a result of mutant genes inheritance (diabetes of neonates), the diabetes caused by the diseases of exocrine pancreas (such as cystous fibrosis), the diabetes induced by a chemical agent (e.g., when medicines are used in HIV/AIDS treatment or after organ transplantation) [8].

Types I и II of diabetes mellitus are most widespread. Type I insulin-dependent diabetes mellitus is a consequence of the destruction of the pancreas beta cells that disturbs the insulin production. The amount of the produced insulin appears insufficient to process the amount of glucose received by the organism. The content of glucose in the organism increases, the chronical hyperglycemia arises, and the metabolism in a number of organs is disturbed [2, 5-9, 19, 64-67]. Type I diabetes mellitus is more frequent in young people, so that it is also referred to as "the diabetes of young". Type I diabetes mellitus comprises nearly 5-10% of the total number of patients, suffering from all types of diabetes mellitus [2, 8]. For type I diabetes mellitus such symptoms are characteristic as polyuria (excess urinary excretion), polydipsia (thirst), permanent hunger, loss of weight, visual impairment, and tiredness [2, 8, 17, 19, 67].

Type II insulin-independent diabetes mellitus develops because of cell resistance to the produced insulin, the insulin deficiency being also present in the organism of the patient. Type II diabetes mellitus is wider spread and comprises about 90–95% of the total amount of diabetic patients. In this case, the disease develops in the middle age, so that this type of disease is often referred to as "the diabetes of aged." However, in recent time this type of diabetes mellitus more and more often appears in children. Diabetes mellitus is largely a result of excessive body mass and physical inactivity [2, 8, 9, 19, 64]. The symptoms of type I and II diabetes mellitus are alike, but in the second case they are often less expressed, because of which the disease is diagnosed in a few years after its beginning, when the complications already arise [2]. In the case of type II diabetes mellitus, the obesity of the patient is an additional symptom [9]. It is important to determine the type of diabetes mellitus for prescribing the most efficient therapy [8].

Under the excess injection of insulin or its excess production induced by medical preparations in patients with diabetes mellitus, the hypoglycaemic coma (crisis) can happen, when the glucose content in blood falls below 3.9 mmol/l (70 mg/dl). In this case, the organism has not enough energy to support normal vital activity, which leads to weakness, trembling, irritability, tachycardia, and hunger, with possible loss of consciousness and fatal outcome [8]. The main cause of diabetes mellitus development is genetic predisposition [8, 19]; the rest causes comprise mainly different diseases that disturb metabolism, as well as the insufficient physical activity [8].

The processes that accompany the aging of the organism become faster with the development of diabetes mellitus [63]. With age the water content in skin decreases, and, correspondingly, the ratio of the base substance and fibrous structures changes. The coefficient decreases at the expense of increasing the collagen content and decreasing the concentration of glycosaminoglycans. The content of hyaluronic acid considerably reduces. The physical and chemical properties of collagen change: the number and strength of inter- and intramolecular crosslinks increases, the elasticity and swelling ability reduces, the resistance against collagenase develops, the structural stability of collagen fibres, i.e., the maturation of fibrillar structures

of the connective tissue progresses. The collagen aging is a result of metabolic processes that occur in the organism and affect the molecular structure of collagen. The connective tissue injury includes the damage of all structural parts of the tissue: the fibrils, the intercellular substance, and the cells [68]. In the studies of the human sclera aging using the wide-angle X-ray scattering, the structure of collagen fibers was investigated. It was found that with age the rigidity of the scleral matrix increases, the degree of fiber straightening and the mechanical anisotropy in the peripapillary sclera decreases [69]. The aging of organism is accompanied by structural and functional modifications of macromolecules [70]. The changes that occur in the tissues of the organism under the development of diabetes mellitus are investigated both in laboratory animals using experimental models [9-11, 17, 39, 40, 42, 45-47, 71-77] and directly in patients in the course of clinical examination [12, 35, 78-87].

3 Experimental models of diabetes mellitus

Among the models of diabetes mellitus, the chemically induced ones that allow relatively cheap and simple induction of pathology development in rodents are widely used. Similar models can be implemented also in higher animals [9-11, 17, 39, 40, 42, 45, 71-77, 88]. The most well-known and widely used methods of chemical diabetes induction are implemented using two compounds, streptozotocin [47, 73-77, 88] and alloxan [17, 39, 40, 42, 45, 46, 71]. Accumulated mainly in the pancreas, they provoke the production of radicals that cause the destruction of the pancreas beta cells and, therefore, disturb the insulin production [9, 10, 11, 75, 89]. Since alloxan and streptozotocin have the structure resembling that of glucose, their accumulation occurs in the pancreas by means of glucose transporters, so that, as a rule, the animals are more susceptible to them on an empty stomach [9, 11, 90]. Thus, the injection of alloxan or streptozotocin to the animals induces the insulin-dependent (type I) diabetes mellitus [11, 89]. Since the solutions of alloxan and streptozotocin are relatively unstable, they should be prepared immediately before the injection. Note that these substances can possess different degrees of toxicity with respect to other organs, too [9, 90, 91]. Besides the destruction of beta cells, alloxan and streptozotocin are capable of modifying biological macromolecules and DNA fragmenting [9, 10, 11, 89].

Dunn *et al*. gave the first description of the alloxan diabetes model in 1943 [11, 89, 92]. A single doze varies from 50 to 200 mg/kg of body mass for mice and from 40 to 200 mg/kg for rats, depending on the breed [9, 10, 42]. Alloxan is injected intravenously, intraperitoneally, or subcutaneously [10, 42, 76].

In 1963 Rakieten published a paper, reporting the capability of streptozotocin to induce diabetes mellitus [11, 75, 93]. The single maximal dose of streptozotocin is from 100 to 200 mg/kg for mice [9, 94, 95] depending on the breed [9, 96] and from 35 to 65 mg/kg of body mass for rats [9, 94]. There is also a method of injecting streptozotocin to animals by small dozes from 20 to 40 mg/kg during 5 days [9].

Note that in contrast to animals, in humans the beta cells of the pancreas are resistant against the toxicity of streptozotocin and alloxan [97]. It is also interesting that the glucose content variation in blood during the first week after the injection of alloxan and streptozotocin is nonlinear (Fig. 1). Immediately after the injection, the glucose content in blood increases during about 3-4 hours, which is accompanied by morphological changes of beta cells: intercellular vacuolisation, dilatation of rough endoplasmic reticulum, reduction of Golgi apparatus area, diminution of secretor granules and insulin content, swelling of mitochondria. Then the hypoglycaemic stage begins, during which in a few hours the glucose content in blood falls, and the hypoglycaemia can lead to fatal outcomes. Such dramatic transient hypoglycaemia appears in the process of insulin accumulation because of the secretory granule toxication and the cell membrane rupture. In addition to the morphological changes, the nuclei of beta cells become pyknotic [11]. In about 6 days after the injection the permanent diabetic hyperglycemic phase comes, for which the morphologically full degranulation and the loss of integrity of beta cells during 12-48 hours is observed [9, 11]. In this connection, it is important to choose the appropriate terms of measuring the glucose content in blood in the process of diabetes modeling.

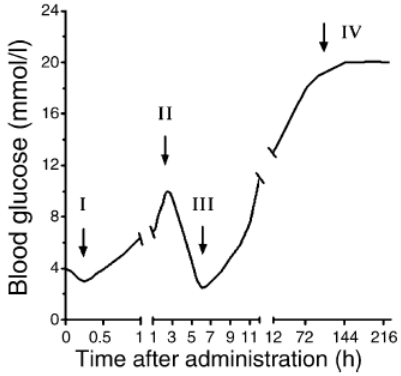

Fig. 1 Phases of free blood glucose variation after the injection of alloxan (I-IV) or streptozotocin (II-IV) [11].

The animals with the model diabetes are characterised by such symptoms as polyuria, polydipsia [67], and loss of body weight [9, 67], typical for type I diabetes mellitus.

Besides the above models of type I diabetes, there are also other ones, which are used less widely, e.g., the autoimmune modes of diabetes. The lines of mice with "spontaneous" diabetes mellitus ("non-obese diabetes") and biobreeding (BB) rats are created, in which from the very birth or in some time after the birth the prediabetic state of the organism develops [9, 66, 67, 98-100]. The Akita mouse lines, in which diabetes mellitus genetically develops in a few weeks after the birth are bred. The diabetes is also induced using viruses [9]. To model type II diabetes mellitus, mono- and polygenic models of obesity, the rats of the Zucker line, etc. are

used [9, 101]. The most widely used monogenic models of obesity possess defects in the transmission of leptin hormone signals. Leptin is responsible for the feeling of saturation, so that the absence of functional leptin in animals gives rise to hyperphagia (overeating) followed by obesity. The $Lep^{ob/ob}$ and $Lepr^{db/db}$ mice, the Zucker rats that possess no leptin receptor experience the lack of leptin. These models are often used to test new methods of type II diabetes treatment [9, 101-104].

In $Lep^{ob/ob}$ mice, the mass increase begins from the age of two weeks, the hyperinsulinemia develops, in four weeks the hyperglycemia manifests itself, the concentration of free glucose in blood continues to grow, achieving the maximum in 3–5 months [9, 105]. The volume of the pancreas significantly increases [9, 106], the hyperlipidaemia progresses, the temperature regulation is disturbed, and the physical activity is reduced [9, 105], the infertility develops [9, 107].

In $Lepr^{db/db}$ mice, the autosomal recessive mutation in the leptin receptor takes place [9, 108]. These mice suffer from hyperphagia, obesity, hyperinsulinemia, and hyperglycemia. The hyperinsulinemia in such mice manifests itself in the age of about two weeks, the obesity from the age of three-four weeks, and the hyperglycemia develops in 4–8 weeks [9].

The Zucker rats possess expressed resistance to insulin that cannot be compensated by the increased level of apoptosis in beta cells [9, 109], which is characterised by hyperinsulinemia at the age of about 8 weeks with subsequent decrease of the insulin level [9, 110]. The diabetes mellitus in Zucker rats commonly develops in nearly 8–10 weeks in males, while in females the explicit diabetes does not develop [9, 94]; in these rats the signs of diabetic complications are observed [9, 110].

Depending on the problems under solution, it is necessary to choose for the experimental studies a suitable model of diabetes with the specific features of the models taken into account. Note also that a given model of diabetes could develop in different ways in animals of different lines. Thus, the authors of Ref. [73] obtained different results for outbred and linear mice.

4 Glycation and non-enzymatic glycation of proteins

The main complications of the diabetes mellitus disease are related to the glycation of proteins. The glycation is a result of the interaction between the glucose molecules and the proteins, which leads to the change of protein structure and to the restriction of tissue functioning [19, 33-36, 38]. It is known that the protein glycation is initiated by the non-enzymatic reaction between the protein amino group and the carbonyl group of sugar and, correspondingly, leads to the formation of crosslinks between the protein molecules [17, 34, 37]. The glycation results in the Malliard reaction [111–113], comprising two stages. As a result of the interaction of protein with glucose via the adducts of the Schiff base, the stable Amadori product is formed. In the course of further incubation, the Amadori product is transformed into an advanced glycation end product [17, 113-115]. The glycation can be accompanied by both the protein modification and the attachment of the advanced glycation end product to the protein receptor [70]. The collagen glycation mechanisms involve complex processes, accompanying the occurring reactions [34, 37, 114, 116, 117]. Such end products of glycation as N(ε)-carboximetillysine (CML) and pentosidine are known to accumulate in the skin collagen with age and diabetes mellitus. Pentosidine is a fluorescent molecule; it can be detected using the methods of fluorescence analysis [37, 70, 114, 116, 118-121]. Glucosepane related to nephropathic, retinopathic, and neuropathic complications [82, 120, 121], glyoxal [118], and pyrroline [70], are also known as advanced glycation end products, as well as other products of glycation and the substances, facilitating their accumulation [70, 121].

Since proteins comprise a considerable part of many tissues, their glycation leads to the change of the tissue structure, the restriction of tissue functioning [6, 34-38, 70, 118], the metabolic disbalance and, finally, the organ malfunction [17]. Due to the fact that the structure of biological tissues determines their optical properties, it becomes possible to monitor these changes by optical methods, such as fluorescence spectroscopy [34, 36, 42, 79, 84-87, 116, 118, 119, 122-128], refractometry [35, 122], Raman spectroscopy [43, 44, 129], spectrophotometry in a wide range of wavelengths [39-41, 47, 84, 86, 130-132], electron microscopy [18, 73, 78], laser speckle-contrast imaging [45, 46], laser Doppler flowmetry [38, 84-86, 133], confocal microscopy [80] and optoacoustic spectroscopy [56].

To study the glycation of proteins, both the samples of tissues and cells from the objects with natural or artificially induced diabetes mellitus (*in vivo* glycation), as well as the samples that has been glycated under *in vitro* conditions are used. Studies of *in vitro* glycation refer, for example, to human placental type IV collagen, performed by fluorescence analysis, as well as by electrophoresis and densitometry [134]; collagen of bovine skin - using multiphoton microscopy [34]; hemoglobin - by optical coherent tomography [135-137], refractometry and IR spectroscopy [122], as well as biochemical analysis [138]; albumin - using fluorescence spectroscopy [70], refractometry [122], and terahertz spectroscopy [138]; collagen of the tendon – through biochemical and biomechanical analyzes [139], as well as to collagen hydrogels - using multispectral fluorescence life time imaging (FLIM) [140]; by incubation in ribose [37, 134, 139, 140], glucose [70, 122, 135, 138, 141] or fructose [70, 141] solutions. All of them show a sufficiently effective glycation of proteins during 10-11 days of incubation, a change in the mechanical properties of tissues due to the formation of collagen cross-links. In work [82], an increase in the glucosapane content in the skin with age and with the development of hyperglycemia in patients with type 1 diabetes mellitus was recorded.

To determine the degree of glycation of proteins, the studies of the fluorescent properties of the glycated hemoglobin and different tissues [34, 36, 42, 116, 118, 119, 123-127] have been performed earlier. The vascular walls modified as a result of glycation [142], the refractive properties of erythrocytes in healthy volunteers and patients with diabetes mellitus [35], and the optical properties of skin in patients suffering from diabetes mellitus [38, 126, 127] were investigated. Multiple papers are devoted to the development of methods for monitoring diabetes and its different complications, based on the detected changes of the optical properties in diabetic tissues in comparison with healthy ones [6, 17, 34-38, 41, 48, 77].

After eight months of glycation of the rabbit Achilles tendon in ribose solution [139] the increased maximum load, deformation stress, Young modulus of elasticity, and viscosity, indicating the fact that the glycation increases the stiffness of the tendon matrix, were observed. The tendon glycation was found to lead to significant reduction of the soluble collagen content and considerable increase of insoluble collagen and pentosidine content. Thus, the obtained results show that the collagen crosslinks caused by glycation directly increase the stiffness of the matrix and change other mechanical properties of the tendon.

The analysis of literature shows that the study of glycated biological tissues is a demanded and promising field of research in view of developing novel technologies for noninvasive or low-invasive monitoring of hard complications, their prevention, and treatment maintenance

5 Optical and structural properties of biological tissues

5.1 Blood and cardiovascular system

The development of diabetes mellitus is related to increased risk of micro- and macrovascular complications (angiopathy) [8, 9, 13, 19, 62-64, 82], such as retinopathy that leads to blindness [8, 9, 10, 13, 31, 60], neuropathy [8, 9, 13, 60], and nephropathy [8, 9, 13, 60]. Diabetes mellitus considerably enhances the risk of vascular diseases that finally result in the cerebral stroke [13, 19, 60, 63]. The hyperglycemia accelerates the atherosclerotic processes [13, 61, 63], the atherosclerosis and the corresponding loss of elasticity of coronary artery walls cause stenosis and, therefore, reduce the blood supply to the cardiac muscle, which finally leads to angina pectoris, cardiomyopathy, and increased risk of myocardial infarction [12, 13, 63, 64]. These serious complications are due to the glycation of proteins in vascular walls permanently washed by blood in the presence of increased free glucose content in blood [41, 129, 135, 138].

Different methods are used to determine glycated hemoglobin or albumin, such as ion exchange, affine, or liquid chromatography, electrophoresis, colorimetric and immunochemical methods [70, 143]. First, these methods are invasive, since they imply blood sampling from the patient's vein. Since the mean lifetime of erythrocytes amounts to three months, it is possible to get information on the glycation accumulated during three months only. Moreover, the accuracy of the measurement is affected by the increased concentration of bilirubin, glucose, lipids, and other substances [143]. Also, the level of free glucose in the blood is influenced by external factors, for example, such as eating and exercise, which limits the applicability of many diagnostic methods where blood measurements are required [7, 8], so it is necessary to develop new algorithms for processing measurement results reducing the influence of external factors.

Optical methods of diagnosing the condition of biological tissues are widely used in biology and medicine, e.g., for determination of oxygenation degree and blood perfusion [144, 145]. The safety of these methods and the possibility to get information in real time explain their wide usage and permanent expansion of the application field in medicine [20, 38, 48, 146-149]. Using optical radiation one can also extract information on the structure, composition, and properties of biological tissues, investigate metabolic processes avoiding negative effect on them [144]. An essential advantage of visible and near-infrared optical radiation is its capability of sufficiently deep penetration into biological tissues. The range from 600 to 2500 nm includes four "transparency windows", i.e., the regions where the light attenuation by biological tissues is minimal. Since many biological tissues contain a lot of water, the spectral transparency windows correspond to the wavelengths, at which the light absorption by water is minimal. The first transparency window includes the wavelengths from 650 to 950 nm, for which the absorption of light by water is relatively weak, but the absorption by hemoglobin and myoglobin is present. The second transparency window is located between two maxima of water absorption and corresponds to the wavelengths from 1100 to 1350 nm. The third transparency window lies in the range from 1600 to 1870 nm and the fourth window from 2100 to 2300 nm, which is convenient for probing the collagen-containing tissues [145, 150-152].

To assess the degree of hemoglobin glycation the Raman spectroscopy can be used [129]. In Ref. [35], microscopic studies with the Nomarsky interference microscope, combining a two-beam interferometer and a polarization microscope to enhance the contrast of phase images, showed a significant difference in the refractive properties of erythrocytes in healthy and diabetic patients.

In Ref. [41], the quantitative assessment of the glycated hemoglobin concentration in human blood was performed using the spectral analysis in the infrared wavelength range (from 780 to 2498 nm). The authors of Ref. [42] measured the fluorescence of blood plasma in 12 days after the alloxan injection to rats. It was shown that the shape of the fluorescence band at the excitation wavelength 320 nm is most indicative for

hyperglycemia in the blood plasma samples due to the formation of protein fluorescent link by non-enzymatic glycation. In Ref. [122], the optical properties of hemoglobin and albumin in aqueous solutions of glucose were studied. With the increase of glucose concentration in the solution, the authors observed the increase of the refractive index and the reduction of the absorption in the studied solutions, probably due to the protein-glucose binding. A decrease in the albumin absorbance in the terahertz range of wavelengths was observed with an increase in the incubation time of albumin (glycation *in vitro*) in solutions of glucose and fructose [138]. Also in this work, slow glycation in glucose in comparison with fructose and the dependence of albumin glycation rate on the pH of the sugar solution were obtained.

The authors of Ref. [44] have shown the applicability of Raman spectroscopy to the assessment of glycated hemoglobin *in vivo* with the measurements performed on hand, ear and forehead. Using the Raman spectroscopy, the porphyrin conformations in erythrocyte hemoglobin were revealed in patients with diabetes mellitus [43]. Using the electronic paramagnetic resonance spectroscopy, the reduction of the erythrocyte membrane viscosity was found in patients with diabetes mellitus. The change of permeability was fixed in the plasmatic membrane of the erythrocyte, namely, the higher rate of Na-H exchange, the activity of Ca^{2+}-dependent K^{+}-channels, the reduction of the Ca-ATPase activity in patients suffering from type II diabetes mellitus [43]. It was supposed that the change of viscosity and permeability of the erythrocyte plasmatic membrane could be the cause of the conformation change of the hemoglobin porphyrin, the reduction of binding activity and oxygen transport by hemoglobin under the conditions of diabetes mellitus [43].

In the patent [130], a noninvasive method and a device for assessing the content of glycated hemoglobin were proposed based on measuring the light reflection spectra from the studied blood sample. The device consists of two measuring units, one of which contains a spectrophotometer, recording the absorption spectra, and the other one contains a Raman spectrometer.

The possibility to use the absorption spectroscopy method for the assessment of the amount of glycated hemoglobin in the spectral range 200–850 nm was demonstrated in [131]. Good correlation between the results of spectroscopic method and the standard method of high-efficiency liquid chromatography was obtained.

The method of quantitative analysis of the content of glycated hemoglobin in human hemolysate samples using near infrared (NIR) spectroscopy and the subsequent processing of the spectra by the moving-window-partial-least-squares (MWPLS) method was proposed in [132]. The method allows to find the optimal wavelength ranges for determining the content of glycated and non-glycated hemoglobin. The optimal wavelengths for the analysis were in the over-current range of the NIR band and were from 958 to 1036 nm for hemoglobin and from 1492 to 1858 nm for glycated hemoglobin.

In [153], the optical characteristics of diabetic erythrocytes using a three-dimensional quantitative phase imaging based on Common-Path Diffraction Optical Tomography (cDOT) were noninvasively studied. The morphological (volume, surface area and sphericity), biochemical (concentration and hemoglobin content) and mechanical (membrane fluctuations) parameters of individual cells were quantitatively determined from the measured three-dimensional tomograms for the refractive index and two-dimensional time-dependent phase images. As a result, statistically significant changes in morphological and biochemical parameters of diabetic erythrocytes were not obtained in comparison with nondiabetic, however, the deformability of the membrane of diabetic erythrocytes was shown to be lower.

Since in the case of diabetes mellitus the advanced glycation end products are dissolved in the blood plasma, they interact with the endothelium, affect the endothelium functioning, and cause the accompanying tissue hypoperfusion and hypoxia [63, 114]. In this way, the advanced glycation end products accumulate in vascular walls, i.e., the formation of crosslinks in the vascular walls occurs [114]. In turn, the endothelium damage gives rise to the development of atherosclerosis [13, 114, 142]. In the presence of diabetes mellitus, the risk of ischemia increases [64, 81].

In comparison with the hemoglobin, which is subject to glycation only during 3 months, the glycation of other proteins occurs during a long time; therefore, the diagnostics of such proteins can provide more information on the condition of the organism in the process of diabetes mellitus development.

In Ref. [73], basing on the histological sections stained by the lectin antibody, the exhaustion of lectin content in the endothelium of mice with four-week streptozotocin-induced diabetes was reported (Fig. 2). The perfusion recovery after ischemia was poorer in diabetic outbred mice (WT) than in linear mice (RAGE KO). Thus, the result can depend on particular animals under study. The studies [81] of human atrium samples *in vitro* performed after reoxygenation and perfusion that modelled ischemia revealed the cell apoptosis and necrosis stronger expressed in patients with type I and type II diabetes mellitus. In rats with streptozotocin-induced diabetes, the apoptosis of myocardial cells was also observed [74].

Diabetes mellitus disturbs the mechanisms of reperfusion, i.e., the activation of earlier existing arterial collaterals and generation of new vessels (arteriogenesis, angiogenesis), thus hampering the recovery after an ischemic stroke [63, 64]. The development of diabetes in outbred mice [73] was found to cause the smaller number of vessels and the accumulation of the advanced glycation end product in muscles and blood of all mice with diabetes.

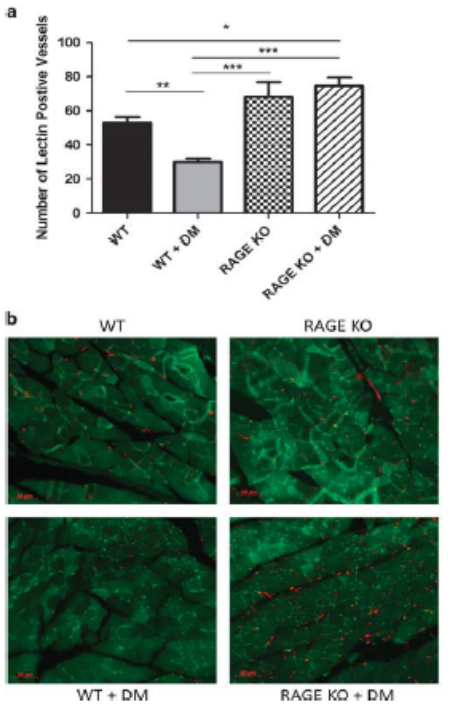

Fig. 2 Histogram (a) and images of histological sections (b) reflecting the content of lectin (red) in WT and WT+DM outbred mice of the control and diabetic groups, and in RAGE KO and RAGE KO+DM linear mice of the control and diabetic groups, respectively [73].

Because of the change of the vessel structure, its physical properties also change. In Ref. [45], the effect of the iohexol solution (X-ray contrast solution, Omnipaque®) on the blood flow velocity in rats with alloxan-induced diabetes was studied using the laser speckle contrast imaging. In contrast to the control group, in diabetic rats the increase of blood flow rate was fixed, which could indicate the increased endothelial permeability under the development of alloxan-induced diabetes [45]. Using ultrasound to measure the elastic modulus of arteries, the authors showed that under type II diabetes mellitus the elasticity of arterial walls decreases [63, 154]. By means of laser Doppler flowmetry, the reduced blood flow rate was observed in the case of diabetes mellitus [38, 133]. Anomalous thickening of vascular walls in skin was also found [38].

The studies aimed at assessing the noradrenalin effect on the blood flow in mice with alloxan-induced diabetes were carried out [45]. Using the laser speckle contrast imaging, the reduction of venous and arterial blood flow caused by the noradrenalin injection was observed in mice with two- and four-week alloxan-induced diabetes without subsequent restoration of blood flow after the noradrenalin injection (Fig. 3).

Since heart is the main organ of the cardiovascular system, through which the process of blood circulation is implemented in the entire organism, it directly experiences the negative effect of the disease with numerous complications [12, 13, 63, 64]. In Ref. [12], the change of adipocytes and the excess accumulation of lipids on the heart epicardium in patients with diabetes mellitus was reported. Such changes enhance the development of heart diseases. In optical measurements [40], the reduction of the glycerol diffusion rate in *ex vivo* myocardium of rats with alloxan-induced diabetes mellitus was observed, which indicates the change of cardiac muscle tissue in the very first weeks of the development of alloxan-induced diabetes in rats.

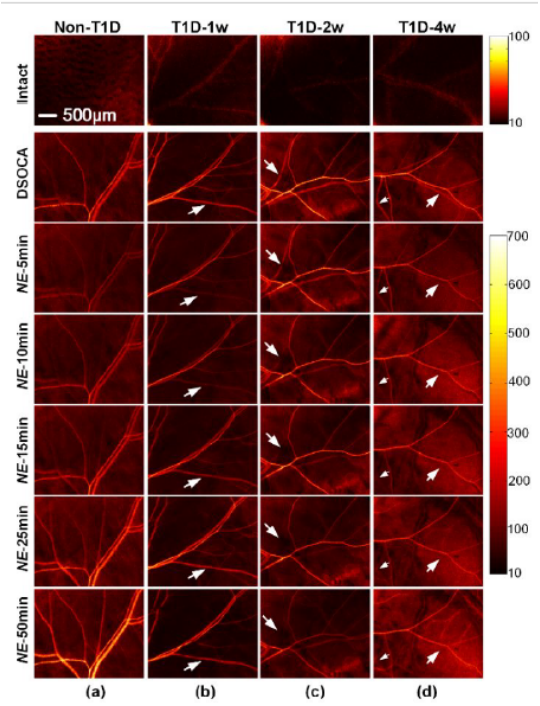

Fig. 3 Typical images of vascular blood flow after the noradrenalin injection to the control group of mice "non-T1D" (a), the mice with one-week "T1D-1w" (b), two-week "T1D-2w" (c), and three-week "T1D-4w" (d) diabetes [45].

The possibility of assessing the functional condition of the microcirculatory system in patients with diabetes mellitus using such optical noninvasive methods as the laser Doppler flowmetry, the diffuse reflection spectroscopy, and the fluorescence spectroscopy was demonstrated in Refs. [84, 86]. The obtained data have shown that the combined application of these three diagnostic technologies allows for revealing and prognosis the development of trophic disorders and the diabetic foot syndrome at earlier stages. The use of wavelet analysis for evaluating the regulatory mechanisms of peripheral blood flow during the heat tests makes it possible to study the changes in the vascular tonus autoregulation and the regulation of bypass blood flow by the sympathic fibers. This allows for indirect consideration of the blood flow innervation and can indicate the presence of neuropathies [84]. The authors of Ref. [86] stated that the hemoglobin introduces a considerable contribution to the spectra of diffuse reflection of human skin in the visible and near-

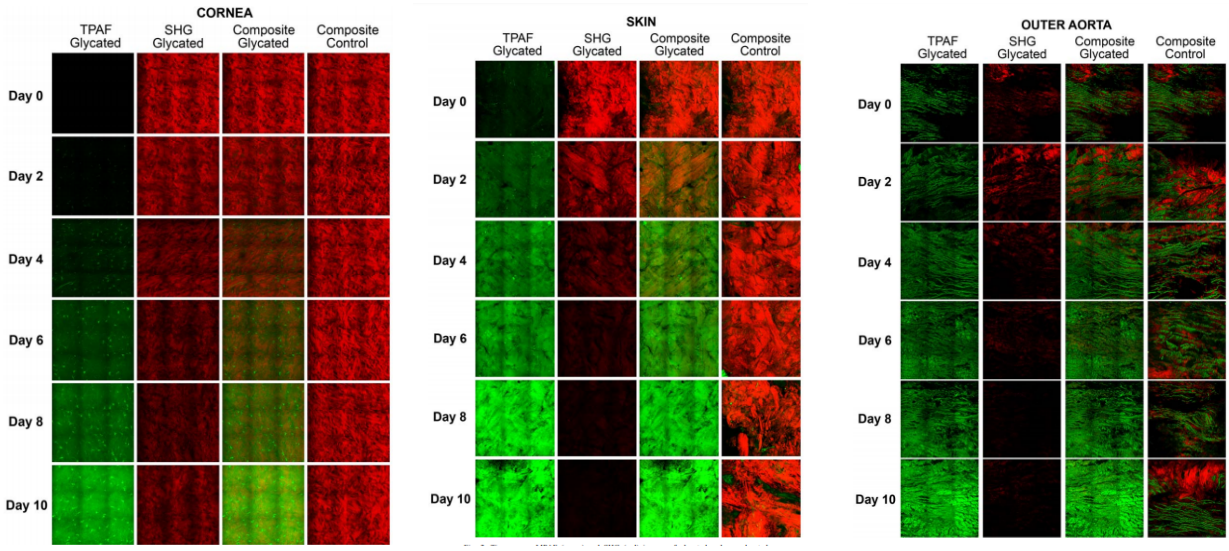

Fig. 4 Images of glycated and control samples of bovine cornea, skin, and outer surface of aorta, obtained by means of multiphoton autofluorescence (green) and the second harmonic generation (red); "Composite" means two superimposed images: the autofluorescence one (green) and the second harmonic generation one (red). The laser wavelength is 700 nm and the power is 180 mW, the image size is 620 × 620 μm^2 [34].

infrared range. The variation of its content under the impairments in the microcirculatory layer of the foot skin due to the diabetic microangiopathy can be seen in the reflection spectra as the change of absorption and scattering properties of skin.

5.2 Different tissues

Type I diabetes mellitus develops due to the pancreas malfunction that leads to the chronical hyperglycemia and then to the excess glucose in the interstitial fluid disturbing the metabolism and the functioning of many organs [2, 5-11, 17, 57, 65-67, 89, 92]. Since all vital organs, such as myocardium, eye retina, and cerebral tissues are abundantly supplied with blood and, therefore, glucose, in the patients with diabetes mellitus they are glycated first.

To find new efficient methods of the diabetes mellitus diagnostics and treatment, to prevent serious complications of this disease, multiple studies of the effect of diabetes mellitus on different properties and functioning of biological tissues and organs have been carried out.

For example, in 12 days after the intra-abdominal injection of streptozotocin to rats [76] the swelling of liver and pancreas mitochondria was fixed that led to the damage of mitochondria and ATP deficiency. In Ref. [17], the effect of diabetes mellitus on the rat internals was studied. After the intra-abdominal injection of alloxan to the rats, the hyperglycemia, polydipsia, and polyuria were fixed in the animals. On the 15-th day after the alloxan injection, the histological sections of liver, kidney, spleen, and pancreas tissues were taken. After the analysis of the histological sections of the tissues, the morphological changes of different degree of severity in comparison with the control group of animals were revealed in the tissues. In the liver, the authors found significant decrease in the glycogen accumulation, in the pancreas the perivascular fibrous indurations were noted, the size and the number of pancreatic islands was decreased [17]. These results confirm the fact that within the frameworks of the alloxan-induced diabetes model in rats already in two weeks after the intra-abdominal injection of alloxan one can detect structural changes of tissues and organs caused by the accumulation of glycogen. In kidneys, the necrosis of individual cells with the development of diabetes was revealed.

Since the high level of blood glucose leads to the growth of its content in the interstitial fluid, the glycation affects not only the blood proteins, such as albumin and hemoglobin [70, 129, 135, 138, 155], but also other proteins of the organism tissues. For example, in Refs. [58, 156] it was concluded that the glycation of collagen under diabetes mellitus facilitates the development of fibrosis. In turn, the structural changes of tissue proteins lead to the change of their optical properties.

Based on the studies of the fluorescence properties of the advanced glycation end products of hemoglobin, skin, cornea, aorta, articular tendon [34, 36, 116, 118, 119, 124, 157], and the corresponding changes in the nonlinear susceptibility of the tissue structures [34, 123, 158], it was found that the glycation facilitates the increase of the tissue fluorescence intensity [34, 116, 118, 119, 124, 125, 157] and the decrease of the second harmonic generation intensity [34, 123, 158] (Fig. 4).

The authors of Ref. [79] studied the autofluorescence of skin and the condition of brain *in vivo* in patients with type II diabetes mellitus. The

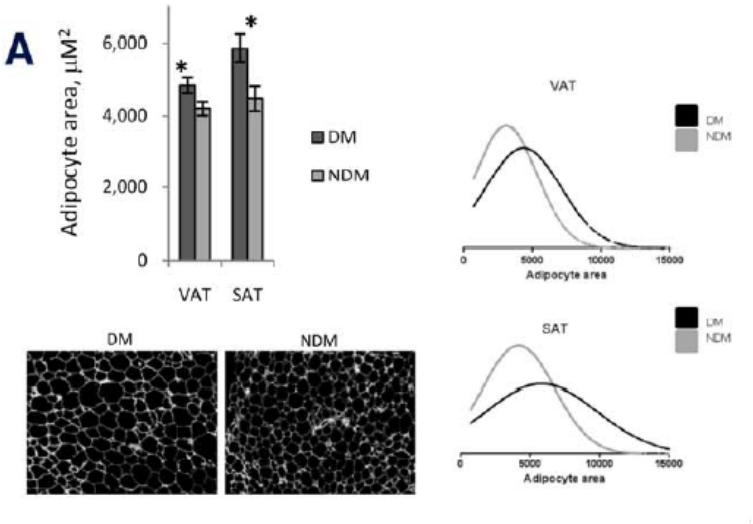

Fig. 5 Histogram, microscopic images, and plots describing the increased size of adipocytes of the visceral (VAT) and subcutaneous (SAT) adipose tissue of the patients suffering from diabetes mellitus [87].

autofluorescence was found to grow both with age and with the development of diabetes mellitus. Using the magnetic resonance tomography (MRT) in patients with diabetes mellitus the reduction of the grey matter in the brain was observed, which, in turn, causes cognitive defects of different degree.

In Ref. [80], it was found that in the group of patients with recently diagnosed type II diabetes mellitus the length and density of nerve fibers is significantly smaller than in the control group. Such studies have been performed by means of the skin biopsy and confocal microscopy of the eye cornea, for which the loss of nerve fibers and the accompanying injure of nerve conductivity were observed, indicating the early parallel involvement of both small and large nerve fibers into the pathological changes.

In turn, the damage of nerve fibers (neuropathy) can lead to a neuropathic foot ulcer, the most severe skin injure arising when the reduced recovery capability of diabetic skin gives rise to infection, formation of gangrene, and, finally, leads to the amputation of lower extremities [58, 59]. The authors of Ref. [79] proposed a hypothesis that the autofluorescence of skin can reflect the formation of advanced glycation end products of other cell proteins, e.g., in neurons.

Since proteins are the main components of many tissues, the glycation of proteins leads to significant change of the tissues structure [34, 37]. The permeability of a tissue for chemical agents is largely determined by the tissue structure and its changes caused by pathological processes, such as glycation. Therefore, the change of the agent diffusion rate in a tissue during a certain time interval can reflect the change of the tissue structure and, thus, can be used as a biomarker of the glycation degree [40, 95, 159]. The study of permeability of biological tissues for different agents is aimed at extracting information on the mechanisms of interaction of tissues with different chemicals, on the transport of drugs in tissues, on the effect of the agents on the optical, diffusion, morphological, and functional properties of biological tissues [48, 49, 52, 146, 147, 160-162]. These data are necessary for efficient application of different pharmacological preparations to treat diabetes mellitus and for developing noninvasive optical methods of disease diagnostics and monitoring [48, 163], since efficiency of treatment (diagnostics) is determined by drug (agent) diffusion rate, i.e., the time during which the drug (agent) molecules reach the target part of the organism.

The slower diffusion of glucose in the kidney sample of diabetic mouse as compared to non-diabetic one was obtained in Ref. [47]. It was assumed that the diabetic kidney has a denser structure at the expense of the tissue glycation. The efficiency of the optical clearing of skin, kidney, and cornea samples in the terahertz wavelength range was higher for non-diabetic samples than for the diabetic ones at application of glycerol solution of different concentration [47].

About 80% glucose in the organism is transported to muscles [19]. The reduction of insulin production under the diabetes mellitus affects the absorption of glucose by muscle cells, which leads to muscle dystrophy and muscle mass reduction [164]. Using electron microscopy, the authors of Ref. [78] observed the 35% reduction of mitochondria size in patients with obesity and type II diabetes. The enlargement of vacuoles in muscle fibres, the lowering of NADH:O_2-oxydoreductase in patients with type II diabetes was also found. The authors concluded that at type II diabetes mellitus a failure of the bioenergetics capability of the mitochondria of skeletal muscles takes place.

Larger fat cells were observed in patients with diabetes mellitus as compared to the healthy volunteers [83]. It was shown that the main phenotype of white fat tissue in humans without obesity and with type II diabetes mellitus is the hypertrophy of adipocytes, which can affect the inflammation of fat tissue, the

release of free fatty acids, the deposition of ectopic fat, and the sensitivity to insulin.

In Ref. [87], using a fluorescence microscope it was found that the mean cross section of the fat tissue adipocytes extracted from the patients during surgical operation is higher in patients with diabetes mellitus than in those of the control group (Fig. 5). The reduction of fibrous tissue formation and the increase of adipocyte hypertrophy was also revealed in patients with diabetes mellitus suffering from obesity. The hypertrophy is a cause of the fat tissue malfunction [87].

The revealed changes of the ocular tissues autofluorescence in the patients with type II diabetes mellitus having no signs of diabetic retinopathy evidence in favour of the accumulation of advanced glycation end products in the eye tissues [165].

The studies of air expired by the patients with type II diabetes mellitus, prediabetic patients, and the control group patients revealed a correlation between the insulin sensitivity index ($1/ISI_{0,120}$) and the content of the isotope ^{13}C ($\delta_{DOB}{}^{13}C(‰)$) in the expired air (Fig. 6). This correlation potentially can serve as a marker for noninvasive assessment of both prediabetic condition and the development of type II diabetes mellitus in humans [166]. This marker was implemented by oral intake of ^{13}C-labelled D-glucose that is metabolised and produces ^{13}C-labelled carbon dioxide ($^{13}CO_2$), which arrives at the lungs via the blood flow and then is expired [166].

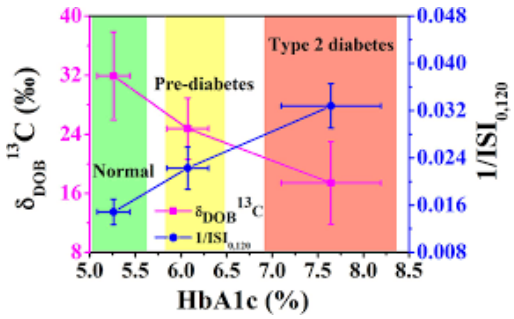

Fig. 6 Distribution of ^{13}C isotope content in the expired air ($\delta_{DOB}{}^{13}C(‰)$) and the insulin sensitivity index ($1/ISI_{0,120}$) depending on the level of glycated hemoglobin HbA1c (%) in the blood of the control group (Normal), prediabetic patients (Pre-diabetes), and of the patients with type II diabetes mellitus (Type 2 diabetes) [166].

5.3 Skin

With the development of diabetes mellitus, the skin becomes susceptible to various infections, the skin fibrosis is observed, the skin becomes more dry and vulnerable (because of the malfunction of leucocytes), and the patient suffers from skin itch. These symptoms are manifestations of diabetes mellitus complications related to the hyperglycemia and glycation of proteins. There are many skin diseases facilitated by diabetes mellitus [19, 58, 59]. With age, structural changes occur in the skin, such as enlargement of pores, thinning of dermis, loss of bulk collagen, atrophy of blood vessels and flattening of dermis-epidermis junction [167]. These age-related changes are enhanced by the development of diabetes mellitus [63]. The skin fluorescence can reflect the age-related changes, the kidney diseases, as well as the changes induced by smoking [126]. The skin autofluorescence enhancement was observed in diabetic patients with retinopathy and nephropathy [127]. The excitation light wavelength varied from 300 to 420 nm with the peak excitation at 370 nm. The normalized autofluorescence signal was calculated by division of the mean radiated light intensity in the range 420–600 nm by the mean intensity of the excitation in the range 300–420 nm [127].

As can be seen from the works [79, 126], the increase in the fluorescence intensity associated with the development of diabetes, and with the aging, so it is important to distinguish the contribution of age and disease in the results of the study. It was shown in [168] that the number of glycated collagen increased only by 33% in patients not suffering from diabetes mellitus at the age of 20 to 85 years. While the fluorescence of the final glycation products in diabetics increased five-fold, strongly correlating with age. In patients with diabetes, glycation of collagen increased three-fold compared to non-diabetic subjects, strongly correlating with the content of glycated hemoglobin in the blood, but not with age. Thus, for a certain age, appropriate glycation levels in tissues can be identified. With diabetes, these indicators are significantly increased.

Many papers are devoted to the study of optical and structural parameters of skin in the process of diabetes mellitus development and its modelling. Unfortunately, the conclusions based on different studies are often contradictory [57]. Thus, in Refs. [169, 170] the hydration of stratum corneum was shown to reduce in humans and mice *in vivo* in the process of diabetes mellitus development, the reduction of water content being not related to the barrier malfunction of epidermis. However, in Refs. [169, 171] it was stated that in the case of diabetes mellitus the transepidermal loss of water does not increase. The authors of Ref. [170] state that long-term hyperglycemia disturbs the barrier function of the skin and its permeability.

In mice with model diabetes mellitus, the reduction of keratinocyte proliferation in epidermis was observed [57, 171, 172], while in Refs. [170, 172] no such changes were observed in the experiments with rats and mice of other age. Contradicting results were also obtained in the studies of epidermis thickness in the case of diabetes [57]. In some papers the authors conclude that the epidermis thickness does not change [170, 172, 173] under the conditions of long-term hyperglycemia in rats and the diabetes mellitus in humans and mice, however, other authors using other model of diabetes mellitus or animals of other age state that the thickness either decreases [171, 172, 174], or increases [175]. The ultrasonic measurement of skin thickness in patients with diabetes mellitus revealed the skin thickness increase [176]. In Ref. [172], the

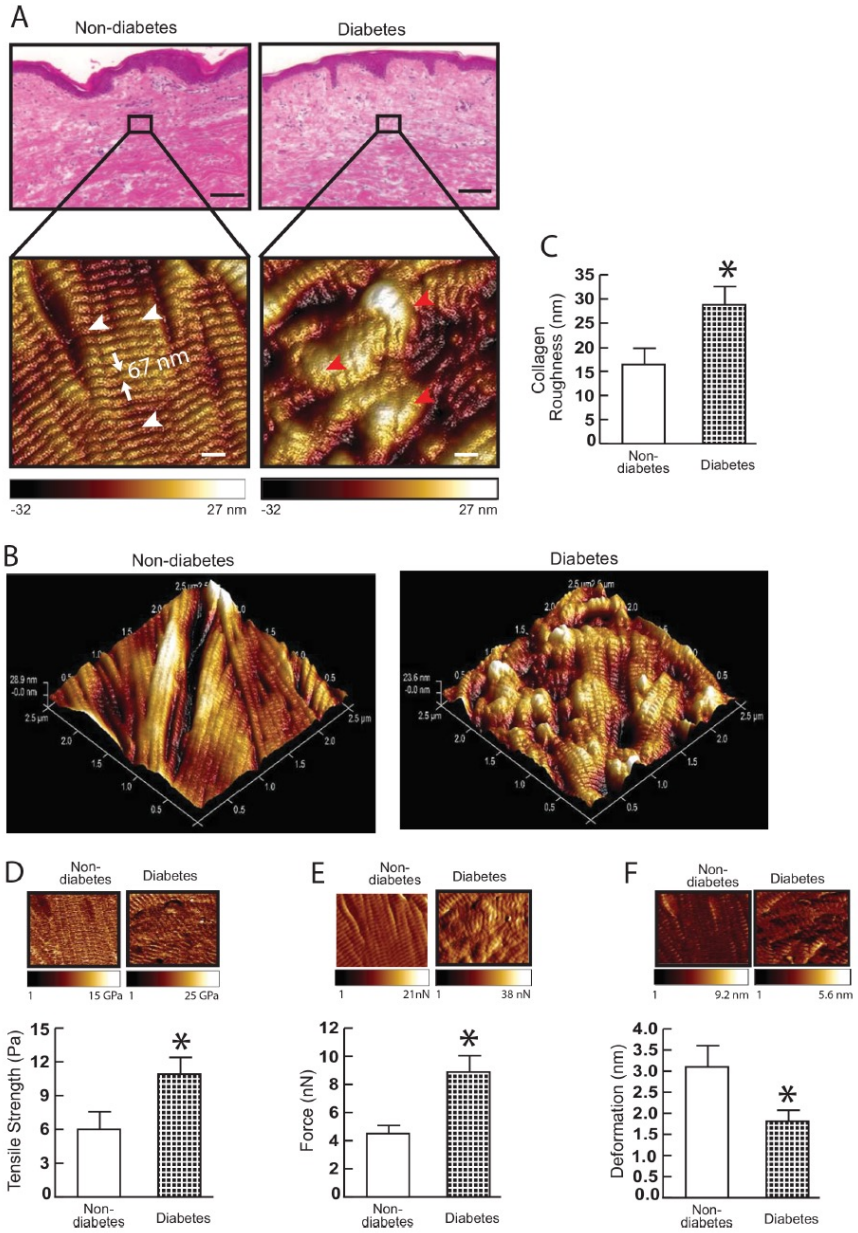

Fig. 7 (A) Image of collagen fibrils obtained using atomic force microscopy (AFM). White and red arrows point at the intact and fragmented/disordered fibrils, respectively. (B) 3D images of collagen fibrils, obtained using the AFM. (C) Roughness of collagen fibrils estimated using the Nanoscope Analysis software (Nanoscope_Analysis_v120R1sr3, Bruker-AXS, Santa Barbara, CA). (D) The tensile strength. (E) The traction force. (F) The deformation of collagen fibrils determined using the AFM PeakForce^{TM} Quantitative NanoMechanics mode and Nanoscope Analysis software [179].

conclusions could be different due to different age of mice under study. The contradiction of results could be also due to the use of different models of diabetes mellitus. The change of collagen distribution in dermis was observed by means of histology and microscopy in diabetic patients with complications, in contrast to those having no complications [177]. The inconsistent results require checking or specifying the features of the experiment that could cause the contradictions.

The formation of advanced glycation end products reduces the elasticity and solubility of collagen, enhances its stiffness [58, 178]. The results presented in Ref. [179] confirm that the accumulation of fragmented skin collagen and the presence of molecular crosslinks in the case of diabetes mellitus impairs the structural integrity of skin collagen and its mechanical properties. In the studies of aging diabetic skin, the expressed crosslinks of collagen fibres were demonstrated. The atomic force microscopy (AFM) has shown that in the case of diabetes the collagen fibrils of skin are fragmented and disordered (Fig. 7(A, B)), and the key mechanical properties are essentially changed [179]. The quantitative analysis of AFM data has shown that the mean roughness of collagen fibrils as a measure of

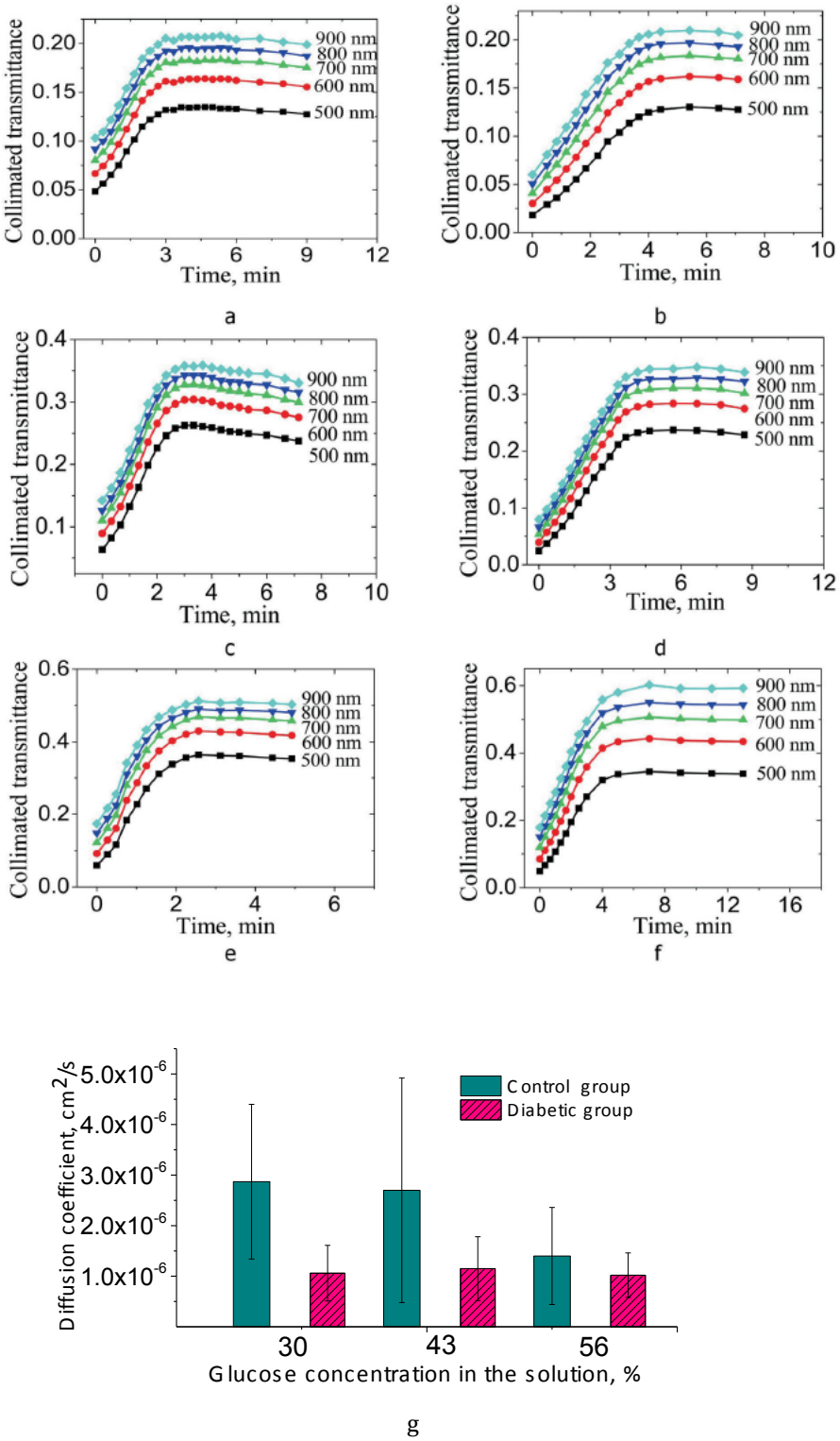

Fig. 8 Kinetic curves of optical clearing (a-f) and diffusion coefficients of glucose (g) in the skin of mice of the control group (a, c, e) and diabetic group (b, d, f) obtained with the 30%- (a, b), 43%- (c, d), and 56%- (e, f) solutions of glucose [39].

their arrangement increases in diabetic dermis by 176% (Fig. 7(C)), from 16 nm to 29 nm, which can be related to the increased content of matrix metalloproteinases (MMPs) that lead to fragmentation of collagen fibrils. The fragmentation of fibrils impairs the structural integrity of collagen and, thus, changes the mechanical properties of the dermis. The basic mechanical properties, such as the tensile strength (Fig. 7(D)) and traction force (Fig. 7(E)), were found to increase by 197% and 182%, respectively, while the deformation of collagen fibrils was reduced by 58% (Fig. 7(F)) in

diabetic dermis in comparison with the non-diabetic one.

The mechanical properties of the collagen hydrogel after incubation in solutions of ribose and glutaraldehyde (GTA), which promote the formation of collagen cross-links, were studied in paper [140] using multispectral fluorescence lifetime imaging (FLIM). In the case of collagen incubation in GTA, in contrast to ribose, correlations were observed between the fluorescence lifetime and the mechanical properties of collagen. It has been shown that the nature and degree of collagen cross-links have a significant effect on the elasticity of the tissue also under the action of ribose.

Under the *in vitro* glycation of murine skin in the glyoxal solution [118] the transepidermal loss of water was increased, the content of saturated fatty acids in the peidermis significantly increased. Moreover, the barrier function of the epidermis was impaired. The skin immersed in the solution of glyoxal acquired a yellow hue. The presence of advanced glycation end products in the skin was detected using autofluorescence, the intensity of which was increased.

Ref. [39] presents the result of studies of glucose diffusion in *ex vivo* skin of mice with alloxan-induced diabetes mellitus by measuring the collimated transmission of visible light through the skin samples. The glucose diffusion in the skin of mice with alloxan-induced diabetes was found to occur by up to 2.5 times slower in comparison with the control group (Fig. 8). Close results were obtained for the glucose solutions of three different concentrations: 30%, 43% and 56%. Analogous reduction of glycerol diffusion rate was observed in the *ex vivo* skin samples from rats with alloxan-induced diabetes mellitus [40].

The optoacoustic spectroscopy was used for the study of advanced glycation end products in skin in the case of *in vitro* glycation [157]. The principle of optoacoustic spectroscopy is based on the transformation of the energy of pulsed or time-modulated optical radiation into thermal and further acoustic waves when interacting with an object, while as a spectrally non-selective detector of absorbed energy at different wavelengths a microphone or an ultrasonic transducer is served [180]. The conditions of physiological hyperglycemia were provided by immersion of porcine skin samples in the ribose solution during 17 days. As a result, the increase of the optoacoustic signal with the incubation time and the maximal absorption of light by the glycated skin in the wavelength range 540–620 nm was observed [157]. Possibly, the increased intensity of the optoacoustic signal with the growth of skin glycation degree is related not only to the high light absorption by glycated skin (in the wavelength range 540–620 nm), but also to the increased efficiency of light-to-sound conversion due to greater tissue elasticity because of the crosslinks between the fibres. In this paper, the increase of fluorescence intensity and the decrease of the second harmonic generation intensity are also demonstrated for the glycated skin (Fig. 9).

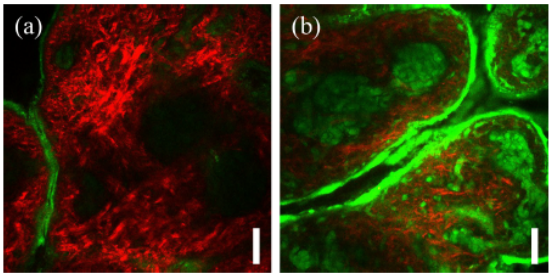

Fig. 9 Microscopic images of porcine skin incubated during 17 days in a) phosphate buffer solution, and b) ribose solution. Superimposed images of autofluorescence (green) and second harmonic (red) intensity are shown. The images were obtained at the depth 35 μm, the scale bars correspond to 50 μm [157].

The patent [128] proposes a device whose operation principle is based on fluorescence, by which it is possible to determine the final products of glycation of collagen, to measure their concentration in skin, the oral mucosa or sclera tissues in order to diagnose diabetes mellitus or pre-diabetic condition. The area of the tissue contactly or contactlessly illuminated by light of wavelengths selected from a wide range, fluorescence of the tissue caused by the exciting radiation is recorded, after that the analyzing system of the device determines the degree of glycation of the tissue from the measured spectral properties.

In Ref. [85], authors evaluated the possibility of combined measurements of skin fluorescence and blood perfusion using the laser Doppler flowmetry for the diagnostics of type II diabetes complications in the lower extremities of the patients. The blood microcirculation was topically stimulated by heating. The experimental studies have shown that the patients with diabetes mellitus demonstrate enhanced fluorescence and lower perfusion response to the local heating, which can play the role of markers for different degrees of diabetic complications.

Ref. [88] describes a method of noninvasive *in vivo* monitoring of hyperglycemic state in mice with streptozotocin diabetes, based on mm-wave spectroscopy, which has been experimentally confirmed using live animal models as objects. The transmission coefficient of the skin fold at the nape of mice of various lines was measured at 25 uniformly located frequencies in the range 0.075–0.110 THz. Skin transmission was several times higher for animals in the hyperglycemic state and depended little on the presence of white or black hair, or its absence in mice.

6 Conclusion

The effect of diabetes mellitus development on the biological fluids and tissues is widely studied, and the development of different research techniques additionally stimulates the growing interest to this disease. In view of diagnostics, it is of primary value to detect the earliest changes in the tissues, related to the progress of diabetes mellitus at its initial stage. As can

be seen from the review, many optical methods are applicable to the diagnostic study and monitoring of the degree of glycation of biological tissues and fluids in the development of diabetes. These include refractometry, Raman spectroscopy, fluorescent spectroscopy, spectrophotometry over a wide range of wavelengths, laser speckle-contrast imaging, laser Doppler flowmetry, optical coherence tomography, confocal microscopy and optoacoustic spectroscopy, multiphoton fluorescence microscopy and harmonic generation. Among a variety of optical methods, one of the promising, because of the simplicity of implementation and the possibility of non-invasive diagnostics, is the fluorescence spectroscopy method, which allows for recording the presence of final glycation products in tissues. Also promising are refractometric and phase methods, including using optical coherence tomography and three-dimensional diffraction tomography. The methods of terahertz spectroscopy and imaging can also be referred to promising methods for studying glycated biological tissues and fluids. The problem of non-invasive monitoring of early structural changes in biological tissues associated with diabetes gradually loses its status as "unresolved".

Disclosures

All authors declare that there is no conflict of interests in this paper.

Acknowledgment

The studies were carried out under the support from RFBR grants 18-32-00587 (DKT); 17-00-00275 (17-00-00186 (DKT) and 17-00-00272 (VVT)); and 18-52-16025 (DKT, VVT).

Statistical studies on optical vortices in dynamic speckle fields

Anindya Majumdar and Sean J. Kirkpatrick*
Department of Biomedical Engineering, Michigan Technological University, Houghton, MI 49931, USA

* **e-mail:** sjkirkpa@mtu.edu

Abstract. New parameters to statistically describe and differentiate between different decorrelation behaviors in dynamic speckle fields are described. These decorrelation behaviors are surrogate descriptors of the dynamics of the underlying processes in object space being observed. The statistical parameters are based on the temporal variations in the location of optical vortices in the speckle fields. The length and number of optical vortex trails, motion of the vortices in the plane of observation and the distance between the mean locations of the positive and negative vortices are investigated. The implementation of the statistical analysis presents new methods to quantify and describe biophysical dynamics. © 2018 Journal of Biomedical Photonics & Engineering.

Keywords: laser speckle; optical vortices; singular optics; light scattering; dynamics.

Paper #3283 received 7 Mar 2018; revised manuscript received 16 May 2018; accepted for publication 17 May 2018; published online 27 May 2018. doi: 10.18287/JBPE18.04.020301.

References

1. A. F. Fercher, J. D. Briers, "Flow visualization by means of single-exposure speckle photography," Optics Communications 37(5), 326-330 (1981).
2. S. E. Murialdo, G. H. Sendra, L. I. Passoni, R. Arizaga, and J. F. Gonzalez, "Analysis of bacterial chemotactic response using dynamic laser speckle," Journal of Biomedical Optics 14(6), 064015 (2009).
3. H. Sendra, S. Murialdo, and L. Passoni, "Dynamic laser speckle to detect motile bacterial response of Pseudomonas aeruginosa," Journal of Physics: Conference Series 90, 012064 (2007).
4. A. Oulamara, A. Tribillon, and G. Doverney, "Biological activity measurements on botanical specimen surfaces using a temporal decorrelation effect of laser speckle," Journal of Modern Optics 36(2), 165-179 (1989).
5. J. D. Briers, S. Webster, "Laser Speckle Contrast Analysis (LASCA): A nonscanning, full-field technique for monitoring capillary blood flow," Journal of Biomedical Optics 1(2), 174-179 (1996).
6. D. A. Boas, A. K. Dunn, "Laser speckle contrast imaging in biomedical optics," Journal of Biomedical Optics 15(1), 011109 (2010).
7. A. K. Dunn, H. Bolay, M. A. Moskowitz, and D. A. Boas, "Dynamic imaging of cerebral blood flow using laser speckle," Journal of Cerebral Blood Flow and Metabolism 21(3), 195-201 (2001).
8. J. F. Nye, M. V. Berry, "Dislocations in Wave Trains," Proceedings of Royal Society of London A 336(1605), 165-190 (1974).
9. M. Berry, J. Nye, and F. Wright, "The elliptic umbilic diffraction catastrophe," Philosophical Transactions of the Royal Society 291(1382), 453-484 (1979).
10. N. B. Baranova, B. Ya. Zel'dovich, "Dislocations of the wave-front surface and zeros of the amplitude," Journal of Experimental and Theoretical Physics 53(5), 925-929 (1981).
11. S. J. Kirkpatrick, K. Khaksari, D. Thomas, and D. D. Duncan, "Optical vortex behavior in dynamic speckle fields," Journal of Biomedical Optics 17(5), 050504 (2012).
12. M. S. Soskin, V. N. Gorshkov, M. V. Vasnetsov, J. T. Malos, and N. R. Heckenberg, "Topological charge and angular momentum of light beams carrying optical vortices," Physical Review A 56(5), 4064-4075 (1997).
13. K. O'Holleran, M. Padgett, and M. Dennis, "Topology of optical vortex lines formed by the interference of three, four and five plane waves," Optics Express 14(7), 3039-3044 (2006).

14. M. Brambilla, M. Cattaneo, L. A. Lugiato, V. Penna, F. Prati, C. Tamm, and C. O. Weiss, "Transverse laser patterns. I. Phase singularity crystals," Physical Review A 43, 5090-5113 (1991).
15. J. M. Vaushan, D. Willetts, "Interference properties of a light-beam having a helical wave surface," Optics Communications 30(3), 263-267 (1979).
16. V. Bazhenov, M. V. Vasnetsov, and M. S. Soskin, "Laser-beams with screw dislocations in their wave-fronts," Journal of Experimental and Theoretical Physics Letters 52, 429-431 (1990).
17. M. W. Beijersbergen, L. Allen, H. van der Veen, and J. P. Woerdman, "Astigmatic laser mode converters and transfer of orbital angular-momentum," Optics Communications 96(1-3), 123-132 (1993).
18. J. E. Curtis, B. A. Koss, and D. G. Grier, "Dynamic holographic optical tweezers," Optics Communications 207, 169-175 (2002).
19. L. Allen, M. W. Beijersbergen, R. J. C. Spreeuw, and J. P. Woerdman, "Orbital angular-momentum of light and the transformation of Laguerre-Gaussian laser modes," Physical Review A 45(11), 8185-8189 (1992).
20. H. He, M. Friese, N. R. Heckenberg, and H. Rubinsztein-Dunlop, "Direct observation of transfer of angular momentum to absorptive particles from a laser beam with a phase singularity," Physical Review Letters 75(5), 826-829 (1995).
21. N. Simpson, K. Dholakia, L. Allen, and M. Padgett, "Mechanical equivalence of spin and orbital angular momentum of light: an optical spanner," Optics Letters 22(1), 52-54 (1997).
22. D. Grier, "A revolution in optical manipulation," Nature 424(6950), 810-816 (2003).
23. A. T. O'Neil, I. MacVicar, L. Allen, and M. J. Padgett, "Intrinsic and extrinsic nature of the orbital angular momentum of a light beam," Physical Review Letters 88(5), 053601 (2002).
24. B. A. Knyazev, Y. Y. Choporova, V. S. Pavelyev, N. D. Osintseva, and B. O. Volodkin, "Transmission of high-power terahertz beams with orbital angular momentum through atmosphere," International conference on Infrared, Millimeter, and Terahertz Waves, 7758816 (2016).
25. G. S. Agarwal and J. Banerji, "Spatial coherence and information entropy in optical vortex fields," Optics Letters 27(10), 800-802 (2002).
26. A. Kumar, S. Prabhakar, P. Vaity, and R. P. Singh, "Information content of optical vortex fields," Optics Letters 36(7), 1161-1163 (2011).
27. D. Rozas, C. T. Law, and G. A. Swartzlander, Jr., "Propagation dynamics of optical vortices," Journal of Optical Society of America B 14(11), 3054-3065 (1997).
28. D. D. Duncan, S. J. Kirkpatrick, "The copula: a tool for simulating speckle dynamics," Journal of Optical Society of America A 25(1), 231-237 (2008).
29. D. D. Duncan, S. J. Kirkpatrick, "Can laser speckle flowmetry be made a quantitative tool?" Journal of Optical Society of America A 25(8), 2088-2094 (2008).
30. M. A. Woo, W. G. Stevenson, D. K. Moser, R. B. Trelease, and R. H. Harper, "Patterns of beat-to-beat heart rate variability in advanced heart failure," American Heart Journal 123(3), 704-710 (1992).
31. M. Brennan, M. Palaniswami, and P. Kamen, "Do Existing Measures of Poincaré Plot Geometry Reflect Nonlinear Features of Heart Rate Variability?" IEEE Transactions on Biomedical Engineering 48(11), 1342-1347 (2001).
32. J. W. Goodman, Speckle Phenomena in Optics Theory and Applications, Roberts & Co., Englewood, CO, USA (2007).
33. M. E. Thomas, D. D. Duncan, "Atmospheric transmission," Chapter in Infrared & Electro-Optical Systems Handbook, Vol. 2, Atmospheric Propagation of Radiation, SPIE Press, Bellingham, WA (1993).

1 Introduction

Random optical interference gives rise to granular patterns with bright and dark regions called speckle. Light scattering techniques, including those involving laser speckle analysis have been used to study dynamic biological systems over the last several decades [1-4]. Speckle based imaging techniques have seen tremendous advancements since the 1990s and are now well-established in the field of biomedical optics [5-7]. Within speckle fields are locations of phase discontinuity where the intensity of the field is zero and the phase is undefined. Such phase singularities were first described by Nye and Berry [8]. A few years later they reported an analysis of phase singularity lines within fields of multiple beam interference [9]. Detailed studies regarding the statistics of the amplitude distribution in such interference fields were conducted by Baranova *et al* [10]. Although the existence of these phase singularities have been known since the 1970s, their in-depth study in speckle fields [11] has garnered interest much more recently.

Speckle fields, $\psi(\mathbf{r},t)$, like other electromagnetic fields, can be written as a general solution of the Helmholtz equation as

$$\psi(\boldsymbol{r},t)=\mathrm{A}(\mathbf{r},\mathrm{t})e^{i\phi(\boldsymbol{r},t)}, \qquad (1)$$

where $\mathrm{A}(\mathbf{r},\mathrm{t})$ is the amplitude and $\phi(\boldsymbol{r},t)$ is the phase of the field, both at location $\boldsymbol{r}$ and time t. The real and

imaginary parts of this speckle field can be separated, with phase singularities occurring in locations where both the real and imaginary parts are zero (Fig. 1).

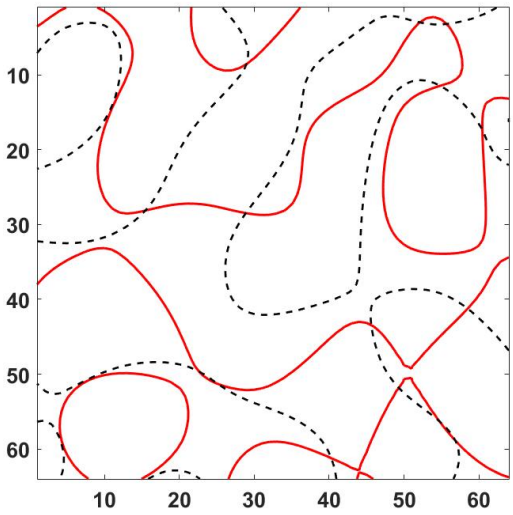

Fig. 1 Zero-contours of real and imaginary field components. The red (solid) lines represent where $\mathrm{Re}(\psi)=0$ and the black (broken) lines represent where $\mathrm{Im}(\psi)=0$. The points of their intersection are the locations of phase singularities.

In the immediate vicinity of and surrounding these singular points, the optical phase rotates in either a clockwise or counter-clockwise direction over at least a full 2π radians and the structures are subsequently referred to as either negatively charged or positively charged optical vortices, respectively [12]. The number of 2π rotations of the phase is known as the topological charge of the vortex, expressed mathematically as

$$n_t = \frac{1}{2\pi}\oint_C \nabla\phi(x,y)\,dl, \qquad (2)$$

where the line integral is along a closed loop, *l*, around the vortex. Optical vortices always occur in pairs of opposite topological charge, and as a consequence of conservation of charge, there must always be an equal number of positively and negatively charged vortices in the scattered field

It should be noted here that the generation of optical vortices does not require special circumstances. It is a phenomenon that accompanies any interference of randomly scattered plane waves [13]. However, experimentally, it has been observed that helically phased beams play a vital role in the formation of phase singularities [14]. These beams, particularly the Laguerre- Gaussian mode (LG_{01}) have been shown to be produced from a combination of Hermite-Gaussian modes HG_{01} and HG_{10} [15]. An alternative method of generation was demonstrated in 1990 where a diffractive element such as a grating with a dislocation was used to obtain a helically phased mode from the Gaussian beam of a laser [16]. Subsequently, the generation of optical vortex beams has also been achieved using spiral phase plates [17] and spatial light modulators [18].

While the angular divergence of the wave-front was already described by Baranova *et al* [10], it was noted by Allen *et al.* [19] that helically phased beams carried orbital angular momentum with them. This was in addition to the already commonly known momenta associated with the polarization state and photon spin. A helical mode whose azimuthal component has the profile $e^{i\phi}$ with ϕ being the phase, has been shown to have an angular momentum of $l\hbar$ per photon. This fact that the helical beams contained angular momentum, has been the basis of multiple applications of optical vortices involving trapping and rotating micro-particles [20-22]. Further advancements were done when particles were made to revolve in an annular ring by using a circularly polarized LG_{01} beam with a large azimuthal component [23]. Developments in remote sensing and wireless communication have also focused on these beams containing orbital angular momentum [24]. Additionally, analyzing the spatial coherence in a one-dimensional projection of the optical vortex field has been used as a method to delve into the information content of an optical vortex [25-26].

Thus, we note that the field of singular optics is a rapidly expanding one, both as a science for understanding the properties of beams creating these fields, as well as in engineering to apply this understanding. It has been previously shown [27] that the optical vortices in an interference field translate in both time and space due to an interplay of three factors, the amplitude gradient, phase gradient and intensity gradient. However, these motions have not yet been correlated to the dynamics of the physical systems which caused the interference. The work presented in this paper is targeted towards gaining a better understanding of the behavior of these optical vortices and their potential use in understanding dynamical biological systems.

2 Methods

Sequences of 50 speckle patterns with user-defined correlation behaviors were simulated using the concept of a copula [28] in the MATLAB environment. Decorrelation rates are defined in terms of the number of frames it takes for the overall speckle pattern autocorrelation coefficient, Γ_I, to reduce to a value of $1/e$. Three different rates of decorrelation behavior between the frames were studied, with their autocorrelation coefficients falling to $1/e$ in 11, 6 and 3 frames, during the 50 frame simulation. Herein, they shall be referred to as the slow, medium and fast rates of decorrelation, respectively. For each of the rates, three different decorrelation behaviors (or modes) were studied. One mode was of constant sequential autocorrelation coefficient ($\Gamma_I = 0.9984$ for slow

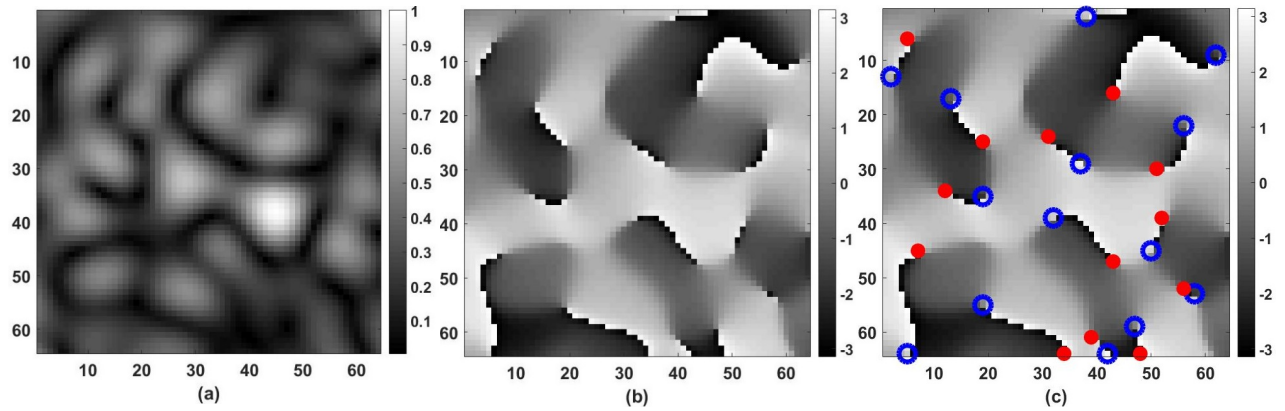

Fig. 2 Locating optical vortices in a speckle field. (a) A speckle image. (b) Its pseudo-phase representation. (c) Location of positive (blue circles) and negative (red points) vortices. The colorbar in (a) indicates relative intensity while those in (b) and (c) indicate phase. The axes represent spatial coordinates.

decorrelation rate; $\Gamma_1 = 0.99$ for medium decorrelation rate and $\Gamma_1 = 0.96$ for fast decorrelation rate) between frames. The second behavior was one that displayed a Gaussian decorrelation line shape. This decorrelation behavior has generally been understood to be associated with ordered dynamics [29]. The third behavior examined, Lorentzian decorrelation, is linked to Brownian dynamics. In general, biological systems likely exhibit a combination of ordered and Brownian (or disordered) dynamics.

Once the 50 speckle patterns were generated for each decorrelation behavior studied, we created a pseudo-phase representation for each of the patterns using a two-dimensional Hilbert filter (Fig. 2(b)) [11]. The location of optical vortices in the speckle were identified and tracked on a frame-by-frame basis through these sequences (Fig. 2(c)).

This was done using a series of convolution operations on the phase distribution over the speckle fields as shown in Eq. (3) and Eq. (4) [11]. This series of convolution operations gives non-zero values only at the locations of phase singularities. These values are the topological charge n_t at those locations.

$$n_t = \phi(x,y) \otimes D_1 + \phi(x,y) \otimes D_2 + \\ + \phi(x,y) \otimes D_3 + \phi(x,y) \otimes D_4, \qquad (3)$$

where $\phi(x,y)$ represents the pseudo-phase of the speckle field, $\otimes$ is the convolution operator and

$$D_1 = \begin{pmatrix} 0 & 1 \\ 0 & -1 \end{pmatrix}; D_2 = \begin{pmatrix} 1 & -1 \\ 0 & 0 \end{pmatrix}; \\ D_3 = \begin{pmatrix} -1 & 0 \\ 1 & 0 \end{pmatrix}; D_4 = \begin{pmatrix} 0 & 0 \\ -1 & 1 \end{pmatrix}. \qquad (4)$$

It is to be noted that Eq. (3) represents a discrete evaluation of the topological charge that is expressed in Eq. (2). The location of a positive (negative) topological charge is called a positive (negative) vortex. Physically, the two different charges represent the two opposing senses of rotation, clockwise and anti-clockwise, of the phase of the speckle field in the complex plane. Tracking any particular vortex, as it traverses through the frames, results in what has been termed a vortex trail [11].

Physically, coherent light scattering from dynamic biological systems over a period of time leads to temporal decorrelation of the speckle pattern in the observation plane. In our simulations, the individual frames can be considered as snapshots of the speckle field as it decorrelates over time. Thus, traversing through frames is equivalent to the temporal movement of a vortex. In this context, frame numbers can be considered as discrete points in time.

Identifying the x and y coordinates of each optical vortex as it passes through the frames, gives rise to a trail from its point of generation to its point of annihilation. Occasionally, a trail also ends due the vortex leaving the field of observation. A trail is called either a positive or a negative trail, according to the sign of the topological charge contained in the vortex that created it. When a negative and a positive vortex intersect at a single spatial and temporal location, they annihilate each other and both trails that they were forming end [11].

A challenge in the simulations discussed herein was to draw the boundary between a continuous trail and a new trail starting close to where a trail ended in the previous frame. As the locations of the vortices were defined in the terms of discrete pixels, it was essential to decide how close two vortices in adjacent frames must be to be considered the part of the same trail. Based on empirical observations of multiple simulation results, it was determined that a change of four or more pixels in any direction would be considered to be the beginning of a new trail.

To create the vortex trail displays like the ones shown in Fig. 3, the vortices in each frame were located as described above, using the series of convolution operators. The location of each vortex, found in this fashion, was then stored on a frame-by-frame basis.

While this enabled us to obtain the visual representation of the vortex trails, the following algorithm was followed to investigate the statistics of the trails.

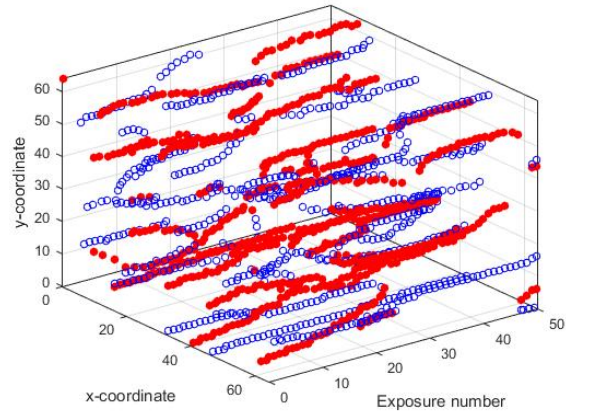

(a)

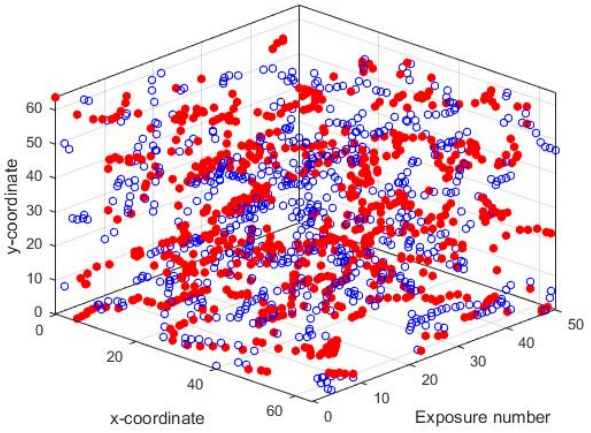

(b)

Fig. 3 Typical displays of vortex trails, as the vortices (red points: negative, blue circles: positive) are tracked through the 50 frames (a). Slow decorrelation with autocorrelation coefficient falling to $1/e$ in 11 frames (b). A faster decorrelation with autocorrelation coefficient falling to $1/e$ in 6 frames.

The coordinates of the vortices found in each frame were stored in an individual list. This was followed by locating the first vortex in the first frame (or equivalently, the first list) and searching for a vortex in the second frame such that it was within four pixels in any direction of the coordinates of the previous vortex found. If such a vortex did not exist, then the trail ended and a new trail began with the next vortex in the first frame. If a vortex was found within the pre-defined four pixel radius, we moved to the third frame and searched for a vortex within the same radius with the coordinates of the second frame as the center location. In this manner, each trail continued until no vortex was found within the set radius of 4 pixels, or all the frames were exhausted. After all the trails starting from the first frame were tracked, the algorithm searched for trails starting from second frame using vortices that were not already considered to constitute any of the previously formed trails. This process continued through the final frame. A pictorial description of this algorithm is shown as a flowchart in Fig. 4.

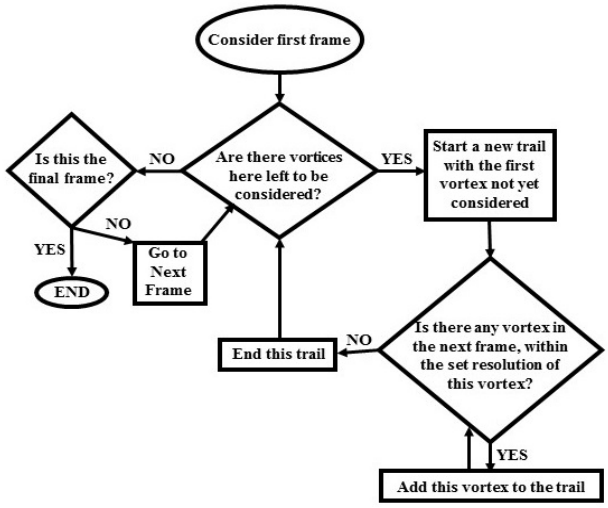

Fig. 4 Flow chart representing the algorithm followed to track individual optical vortex trails.

Once the individual trails were tracked, various parameters of the motion of the vortices were investigated. One parameter investigated was the average length of the positive and negative trails, as well as the overall average length of all trails regardless of charge. This was defined in terms of the number of frames the average trail survived. Another parameter studied was the average displacement of the vortices, as they traversed through the frames (equivalently, through time). For this, the positive and negative centers of the frames were determined. A positive (negative) center (X_c, Y_c) of a frame is defined as the mean location of all the positive (negative) vortices in the frame:

$$X_c = \frac{\sum_{i=1}^{n} x_i}{n}; Y_c = \frac{\sum_{i=1}^{n} y_i}{n}, \qquad (5)$$

where (x_i, y_i) is the coordinates of the i^{th} vortex in the frame and n is the total number of positive (negative) vortices in the frame. The overall center of the frame (X_{co}, Y_{co}) is the weighed mean location of the positive and negative centers:

$$X_{co} = \frac{n_p X_{cp} + n_n X_{cn}}{n_p + n_n}; Y_{co} = \frac{n_p Y_{cp} + n_n Y_{cn}}{n_p + n_n}, \qquad (6)$$

where (X_{cp}, Y_{cp}) is the location of the positive center and (X_{cn}, Y_{cn}) is the location of the negative center; n_p

Table 1 Average trail lengths and number of trails of each type (C: Constant; G: Gaussian; L: Lorentzian). The trail lengths are given as the number of frames the trail lasted. Total number of frames in the simulation = 50.

	Slow Decorrelation			Medium Decorrelation			Fast Decorrelation		
	C	G	L	C	G	L	C	G	L
Positive Trail Length	9.85	8.71	10.09	3.93	4.04	4.42	2.02	2.14	2.48
Negative Trail Length	9.78	8.64	10.39	3.73	4.21	4.51	1.94	2.05	2.45
Positive Trail Nos.	71	80	64	169	163	154	323	304	282
Negative Trail Nos.	68	83	61	176	164	148	331	314	274

and n_n represent the number of positive and negative vortices in the frame, respectively. We defined the mobility, M, for each type of vortex as the mean distance moved by their center, per frame (Eq. (7)):

$$M_{cp,cn,co} = \frac{1}{N-1} \times \sum_{i=2}^{N} \sqrt{({}^{i}X_{cp,cn,co} - {}^{i-1}X_{cp,cn,co})^2 + ({}^{i}Y_{cp,cn,co} - {}^{i-1}Y_{cp,cn,co})^2}, \quad (7)$$

where M_{cq} represents the mobility of the q^{th} type of vortex and $\left({}^{i}X_{cq}, {}^{i}Y_{cq}\right)$ is the location of the center of q^{th} type of vortex in the i^{th} frame. As indicated, q can represent positive (p), negative (n) or overall (o). N is the total number of frames in the simulation.

Additionally, the distance between the positive and negative centers of each the frame was studied. We have termed this distance as the charge separation, $G(i)$. Poincaré plots [30] were used to analyze the charge separation. Poincaré plots are used to display consecutive measurements against each other, *i.e.*, the i^{th} element of a series X, $X(i)$ is plotted against the $(i\text{-}1)^{th}$ element, $X(i\text{-}1)$. This is continued for all set of consecutive data points on X.

Once all the data points are plotted as above, standardized metrics $SD1$ and $SD2$ for the data set are measured [31] with the following definitions

$$SD1 = Var\left(\frac{1}{\sqrt{2}}X(i-1) - \frac{1}{\sqrt{2}}X(i)\right)^{\frac{1}{2}}; \quad SD2 = \left\{2\,Var\left(X\right) - SD1^2\right\}^{\frac{1}{2}}, \quad (8)$$

where $Var(X)$ stands for the variance of the data series X.

An ellipse fitting process is then employed over the Poincaré plots. This ellipse has semi-major axis length of $SD2$ and semi-minor axis length of $SD1$ with the major axis inclined at 45° to the horizontal axis of the Poincaré plot (Fig. 7). The metric $SD1$ represents the short-term variations of the quantity measured (such as standard deviation in successive differences), while $SD2$ is what remains when contribution of $SD1$ is removed from the variance (Eq. 7) and thus indicates the long-term variations. The shape of the obtained ellipse indicates the comparative effects of each type of variation. The more dominant long-term variations are, the higher is the magnitude of the semi-major axis (given by $SD2$), resulting in a more elongated ellipse.

3 Results and Discussion

The average trail lengths and number of trails for each type of vortex is noted in Table 1.

The effects of decorrelation line shapes and rates were investigated (see above). By weighting the trail length of each type (positive and negative) by the corresponding number of trails, the overall average trail length of each type and rate of decorrelation was obtained. These results are displayed in Fig. 5.

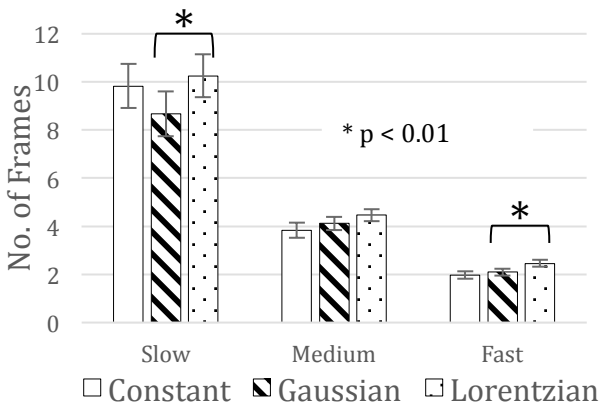

Fig. 5 Average trail length for each decorrelation type, under three different rates of decorrelation. (Slow: $(1/e)$ = 11 frames; Medium: $(1/e)$ = 6 frames; Fast: $(1/e)$ =3 frames; Total frames in simulation = 50. The statistics are from 20 measurements, each measurement comprising of all 50 frames initiated from a randomly generated speckle pattern; Error bars represent 1 standard deviation

The Lorentzian decorrelation behavior typically resulted in longer and fewer trails compared to Gaussian decorrelation, given the same rate of decorrelation ($p < 0.01$) for both the slow and fast rates of decorrelation shown in Fig. 5. The Student's t-test for

Table 2 The average displacement of each type of vortex center as they travel through the frames (C: Constant; G: Gaussian; L: Lorentzian). All distances are given in terms of coordinate points. Each frame was a square of 64 × 64 coordinate points.

	Slow Decorrelation			Medium Decorrelation			Fast Decorrelation		
	C	G	L	C	G	L	C	G	L
Positive Displacement	2.63	2.58	2.14	4.30	4.67	3.37	5.07	5.14	4.40
Negative Displacement	2.96	2.97	2.29	4.26	4.50	3.71	5.17	5.56	4.57
Overall Displacement	2.66	2.62	2.10	4.02	4.38	3.38	4.89	4.91	3.95

difference of means was used for all statistical significance testing in this study. Additionally, it was also observed that as the rate of decorrelation increases, the average trail length of each mode became shorter. For each type of decorrelation, the number of vortices in each frame roughly remained independent of all other simulation conditions. The number of vortices identified was on the order of half of the number of coherence areas in each speckle field [32]. Thus, longer trails directly resulted in fewer number of trails. In addition to elongated trail lengths, slower decorrelation was also found to be associated with lesser number of individual trails. The third mode, constant rate of decorrelation ($\Gamma_1 = 0.9984$ for slow, $\Gamma_1 = 0.99$ for medium and $\Gamma_1 = 0.96$ for fast decorrelation, respectively), formed the shortest, and by extension, the most number of trails at the medium and fast decorrelation modes. At the slowest decorrelation rate, the constant decorrelation mode formed trails longer than the Gaussian mode, but shorter than the Lorentzian mode.

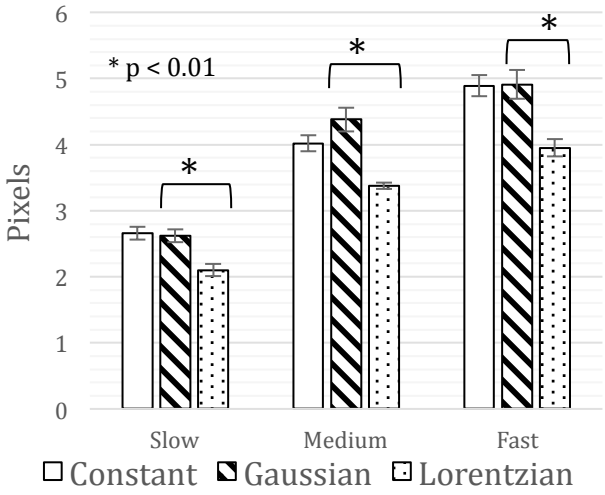

Fig. 6 Average vortex displacement (or mobility) for each mode, under three different rates of decorrelation (same as Fig. 5). The statistics are from 20 measurements, each measurement comprising of all 50 frames initiated from a randomly generated speckle pattern; Error bars represent one standard deviation

The next parameter that was investigated was the mobility, M, of the vortices. Mobility was defined in terms of the average displacement incurred by the center of each type of vortex field, while moving between consecutive frames. From Table (2), we can observe that the vortices experienced higher mobility under Gaussian decorrelation, as compared to Lorentzian decorrelation ($p < 0.01$). Additionally, increasing the rate of decorrelation resulted in higher motion of the vortices ($p < 0.01$). Combining the results from both the tables above, it can be seen that the longer trails were associated smaller displacements.

To study the variations in charge separation, Poincaré plots [7] were employed. As noted above, these plots are used to investigate the long-term and short-term variations in a variable. In this case, the variable in question was the charge separation over the 50 frames. A typical Poincaré plot from this set of measurements is shown in Fig. 7.

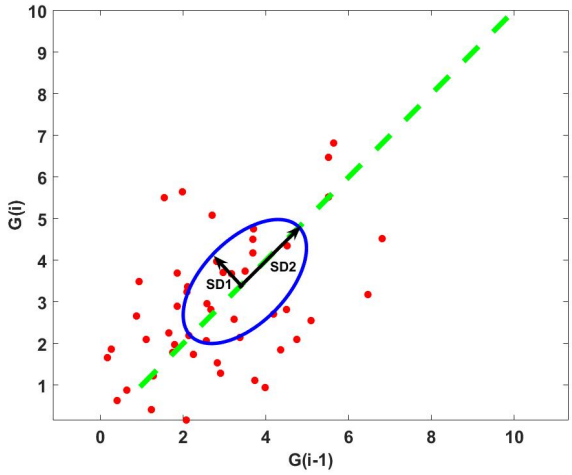

Fig. 7 A typical Poincaré plot obtained for charge separation $G(i)$. The magnitude of descriptor $SD1$ indicates short-term variability in the value of the separation, while $SD2$ indicates the long-term variability. In this plot, $SD1 = 1.01$ and $SD2 = 1.85$. The lengths are in terms of coordinate points. This simulation was done for a 64 × 64 pixel speckle field.

It was observed that slow decorrelation resulted in elongated ellipses on the Poincaré plot, which is a result of higher $SD2/SD1$ ratio. As mentioned earlier, this is

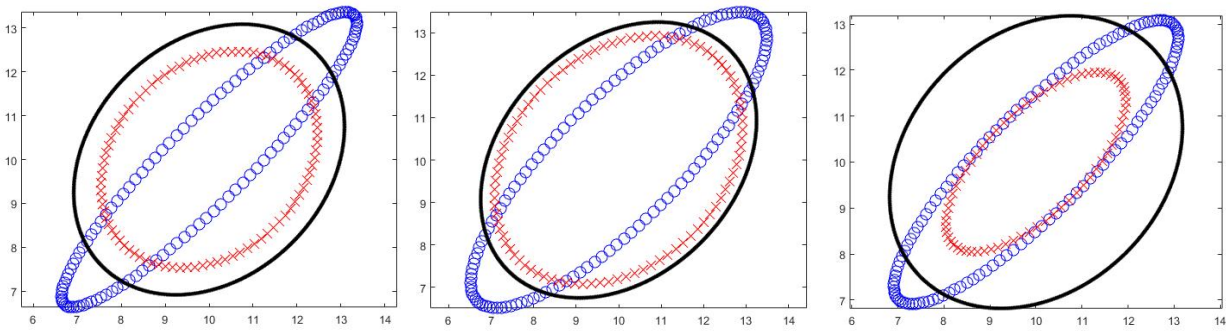

(a) (b) (c)

Fig. 8 Ellipses from the Poincaré plots of charge separation *G(i)* for (a) Gaussian (b) Constant and (c) Lorentzian decorrelation behavior. (O : Slow decorrelation; X : Medium decorrelation; - :Fast decorrelation). It can be noted that the ellipses are prominently elongated for the slowest rate of decorrelation, indicating a high *SD*2/*SD*1 ratio. This elongation of the ellipse indicates a greater effect of long-term variations on the conditions under which the measurement has been made.

the ratio of the long-term variability to the short-term variability. Thus, we notice that as the decorrelation rate increases, the short-term variations tend to become more prominent as compared to the long-term variations. This ratio tends towards a value of 1.0 at higher decorrelation rates. The *SD*2/*SD*1 ratios can be visualized by placing the obtained ellipses in overlap with each other, as shown in Fig. 8.

It can be seen that the use of Poincaré plots of charge separation gives a stronger indication of the rate of decorrelation, rather than the lineshape of the decorrelation. Thus, this can be used as an indicator of the rate of dynamics in a system as is discussed below

4 Conclusion

In this paper, a new approach to studying dynamic systems by tracking phase singularities (or optical vortices) has been presented. Speckle patterns for biological systems inherently contain phase singularities, or optical vortices, points around which the phase of the field rotates. In this work we have related the observed dynamics of the optical vortices in a simulated speckle field, to the type and rate of decorrelation in the field. This decorrelation is a representative of the dynamic behavior of scatterers that, under coherent illumination, produced the speckle field under observation [29].

Analyzing the location of vortices at discrete time points in a speckle field simulated using a pre-defined rate of decorrelation, we note the expected result that as the rate increased, the lengths of the vortex trails decreased. In this study, the rate of speckle decorrelation was assumed to correspond to the rate of activity in the scattering object. Thus, in a scattering medium with fast motion among particles, the individual phase singularities tend to survive for shorter periods of time. Faster activity was also shown to result in a higher degree of vortex displacement per frame in the location of the singularities. Additionally, we compared different modes of activity; a Lorentzian decorrelation relationship between frames, corresponding to Brownian or unordered form of activity among the scatterers and a Gaussian decorrelation relationship, corresponding to an ordered mode of activity among the scatterers. The ordered motion resulted in more mobile phase singularities as they traversed through time. This also corresponds to shorter durations for which the trails existed. We remind the readers that the mobility, *M*, is defined as the average displacement per frame of the mean location (center) of the vortices. A possible reason for low vortex mobility for Brownian motion could be the homogeneous line profile of the scatterer distribution in a Lorentzian flow model [33]. This homogeneity results in no preferential direction for the vortices to move. This results in the average summed motion to be less than the Gaussian flow model, which has an inhomogeneous line profile of the scatterers [33]. We also examined a technique of analyzing sequential vortex data using Poincaré plots, by separating the long and short-term variations and calculating their relative prominence with regards to each other. When applied to the average charge separation per frame, this technique did not indicate any significant difference between the different modes of decorrelation. However, reducing the rate of decorrelation did result in the Poincaré ellipses elongating, indicating a higher prominence of the long-term variations. A possible reason could be that faster decorrelation did not allow sufficient time for the long-term trends in the data to dominate over the short-term trends. We note here that at no point at all do the short-term variations *SD*1 dominate over the long-term variations *SD*2 . In the case in which $SD1 > SD2$ the ellipse would be more “broad” than “long’, i.e., the major and minor axes would have reversed. Thus, the use of Poincaré plots was more useful in comparing the different rates of activity, rather than the different modes of activity.

Note that actual phase information is not available in the intensity speckle patterns, and thus we took the approach of calculating pseudo-phase estimate maps

using convolution operators [11]. While this approach will not necessarily re-create the true phase of an imaged speckle pattern, the behavior of the vortices is not affected. Also, the simulation only takes into account a limited spatial window of the speckle field. Thus, there are instances of minor topological charge imbalance (about 1 extra vortex in 4000 total vortices) in some of the simulations. This usually occurred in situations where a vortex was close to the edge of the observation window, and the opposite topological charge corresponding to this lone vortex was just outside the window. This oppositely charged vortex typically appeared within the window in the very next frame, thus balancing out the charges. This can be thought of as a case where a pair production happens right at the edge of the window, but only half the pair is within the window at that instant. It is also to be noted we are currently not in a position to speculate on the physical significance of some of the parameters noted here (such as the charge separation, $G(i)$). As such, they are introduced only as a measureable feature with some sensitivity to the simulation dynamics (in the case of $G(i)$, sensitivity to the rate of activity).

We conclude by noting that the analysis in this paper can potentially be used to add to our current understanding of light scattering and propagation, the physics of coherent wave fields, and the field of singular optics. This can, in turn be used to improve existing microscopy and imaging techniques, particularly those aimed at quantifying biophysical dynamics. Simulating additional biological features such as tumors and other complex systems containing dynamics scattering elements, and identifying them using the dynamics of optical vortices as done in this paper, is among the possible directions in which this research can progress.

Disclosures

The authors have no relevant financial interests in this article and no potential conflicts of interest to disclose.

Thermal effect in laser perforation of liver

Olga I. Baum*, Alexander K. Dmitriev, Vladimir N. Kortunov, Olga A. Tiflova, and Valery A. Ulyanov

Institute of Photonic Technologies, Federal Scientific Research Centre 'Crystallography and Photonics' of the Russian Academy of Sciences, 2 Pionerskaya Str., Moscow (Troitsk) 142190, Russia

*** e-mail:** baumolga@gmail.com

Abstract. One of the trends in the development of modern regeneration medicine is the application of high-intensity laser radiation for deep perforation of biological tissues, stimulating the regeneration of structure and functions of the pathologically changed tissues. In the paper, the possibility to control the location and parameters of the biotissue thermal stimulation zones is studied theoretically and experimentally, depending on the conditions of laser perforation in application to the liver laser-induced regeneration problem. The results of numerical simulation revealed the basic trends in the behaviour of the thermal stimulation zone, which are in good agreement with the experimental data on laser perforation of soft biotissues *ex vivo* using an optical fibre.

Keywords: fibre laser; perforation; liver; regeneration; thermal fields.

Paper #3288 received 11 Apr 2018; revised manuscript received 25 May 2018; accepted for publication 25 May 2018; published online 17 Jun 2018. doi: 10.18287/JBPE18.04.020302.

References

1. I. I. Berishvili, Transmyocardial Laser Revascularisation, GEOS, Moscow, Russia (2016) [in Russian]. ISBN 978-5-89118-703-0
2. X. M. Mueller, H. T. Tevaearai, C. Y. Genton, P. Chaubert, and L. K von Segesser, "Are there vascular density gradients along myocardial laser channels?" The Annals of Thoracic Surgery 68(1), 125-129 (1999).
3. X. M. Mueller, H. T. Tevaearai, C. Y. Genton, P. Chaubert, and L. K von Segesser, "Improved neoangiogenesis in transmyocardial laser revascularization combined with angiogenic adjunct in a pig model," Clinical Science 99(6), 535-540 (2000).
4. D. I. Alyokhin, A. A. Fokin, "Prospects of using high-intensity laser radiation for the treatment of chronical ischemia of extremities," Patologiya krovoobrashcheniya i kardiokhirurgiya 2, 88-92 (2005) [in Russian].
5. S. V. Kapralov, I. A. Mel'nikova, U. G. Shapkin, and V. V. Alipov, "Experimental modelling of laser fenestration of liver," Byulleten' meditsinskikh Internet-konferentsii 1(2), 47 (2011) [in Russian].
6. I. A. Shved, T. E. Vladimirskaya, A. V. Vorobey, O. P. Shorez, S. V. Alexandrov, and A. C. Shuleiko, "Liver tissue regeneration after laser coagulation," Zdravookhraneniye (Belarus) 3, 4-8 (2014) [in Russian].
7. L. Lamalice, F. Le Boeuf, and J. Huot, "Endothelial cell migration during angiogenesis," Circulation Research 100(6), 782-794 (2007).
8. A. Briolay, R. Jaafar, G. Nemoz, and L. Bessueille, "Myogenic differentiation and lipid-raft composition L6 skeletal muscle cells are modulated by PUFAs," Biochimica et Biophysica Acta (BBA) – Biomembranes 1828(2), 602-613 (2013).
9. A. Dolganiuc, "Role of lipid rafts in liver health and disease," Would Journal of Gastroenterology 17(20), 2520-2535 (2011).
10. M. Troyanova-Wood, J. D. Musick, B. L. Ibey, R. J. Thomas, and H. T. Beier, "Observation of changes in membrane fluidity after infrared laser stimulation using a polarity-sensitive fluorescent probe," Proceeding of SPIE 8941, 89410I (2014).
11. L. Jin, C. Millard, J. P. Wuskell, H. A. Clark, and L. M. Loew, "Cholesterol-enriched lipid domains can be visualized by di-4-ANEPPDHQ with linear and nonlinear optics," Biophysical journal: biophysical letters 89(1), L04-L06 (2005).

12. A. J. Garcia-Saez, S. Chiantia, and P. Schwille, "Effect of line tension on the lateral organization of lipid membranes," Journal of Biological Chemistry 282(46), 33537–33544 (2007).
13. G. Muller, K. Dorschel, and H. Kar, "Biophysics of photoablation process," Lasers in Medical Science 6(3), 241-254 (1991).
14. N. N. Kalitkin, Numerical Methods, Nauka, Moscow, Russia (1978) [in Russian].
15. O. I. Baum, "Temperature control system for laser reshaping of nasal septum," Izvestiya Vysshikh Uchebnykh Zavedeniy. Priborostroenie 58(10), 847-854 (2015) [in Russian].
16. O. I. Baum, Y. M. Soshnikova, E. N. Sobol, A. Ya. Korneychuk, M. V. Obrezkova, V. M. Svistushkin, O. K. Timofeeva, and V. V. Lunin, "Laser reshaping of costal cartilage for transplantation," Lasers in surgery and medicine 43(6), 511-515 (2011).
17. A. V. Yuzhakov, A. P. Sviridov, E. M. Shcherbakov, O. I. Baum, and E. N. Sobol, "Optical properties of costal cartilage and their variation in the process of non-destructive action of laser radiation with the wavelength 1.56 μm," Quantum Electronics 44(1), 65 (2014).
18. O. I. Baum, E. N. Sobol, A. V. Bolshunov, A. A. Fedorov, O. V. Khomchik, A. I. Omelchenko, and E. M. Shcherbakov, "Microstructural changes in sclera under thermo-mechanical effect of 1.56 μm laser radiation increasing transscleral humor outflow," Lasers in surgery and medicine 46(1), 46-53 (2014).
19. O. Baum, S. Wachsmann-Hogiu, T. Milner, and E. Sobol, "Laser-assisted formation of micropores and nanobubbles in sclera promote stable normalization of intraocular pressure," Laser Physics Letters 14(6), 065601 (2017).
20. E. Sobol, A. Shekhter, A. Baskov, O. Baum, I. Borchshenko, V. Golubev, A. Guller, I. Kolyshev, A. Omeltchenko, A. Sviridov, and O. Zakharkina, "Regeneration of spine disc and joint cartilages under temporal and space modulated laser radiation," Proceeding of SPIE 7179, 71790B (2009).
21. E. Sobol, A. Shekhter, A. Guller, O. Baum, and A. Baskov, "Laser-induced regeneration of cartilage," Journal of Biomedical Optics 16(8), 080902 (2011).
22. E. Sobol, O. Baum, A. Shekhter, S. Wachsmann-Hogiu, A. Shnirelman, Y. Alexandrovskaya, I. Sadovskyy, and V. Vinokur, "Laser-induced micropore formation and modification of cartilage structure in osteoarthritis healing," Journal of Biomedical Optics 22(9), 091515 (2017).
23. M. N. Libenson, E. B. Yakovlev, and G. D. Shandybina, "Interaction of Laser Radiation with Matter (Power Optics)," Lecture Notes. Part II. Laser Heating and Material Destruction, V. P. Veyko (Ed.), ITMO, Saint-Petersburg (2006) [in Russian].

1 Introduction

One of the trends in the development of regeneration medicine is the application of high-intensity laser radiation for stimulating the recovery of tissue blood supply, structure and functions of vital organs of the human organism. Such approach, in particular, allowed the development of a new method of treatment of the ischemic heart disease, the transmyocardial laser revascularization revascularisation, in the process of which deep channels are created in the ischemic muscle by the high-power laser action. The laser perforation of the cardiac muscle initiates the process of angiogenesis, i.e., the growth of microcapillaries in the zone of the laser impact. The mechanisms of laser revascularisation include the following: i) the development of aseptic inflammation in the perforated region in response to the laser impact with subsequent regeneration and development of microcapillaries; ii) the thermal impact on the tissues surrounding the laser channel, activating different cell elements that are sources of growth factors playing the key role in simulating the angiogenesis process; iii) the formation of multiple microscopic ruptures of the tissue in the channel walls caused by the shockwave impact that establishes a new level of oxygen consumption in the affected volume, improving the blood supply. To date it is established that the improvement and long-term stability of the patient's clinical indicators depend both on the radiation wavelength and on the mode of laser tissue perforation (continuous-wave, pulsed, etc.), which determine the positive effect of the procedure [1]. It is experimentally shown that the neovascularisation of the ischemic myocardium is observed both directly in the region of the laser channel [2], and within 3-5 mm zone around the channel [3], thus essentially increasing the revascularisation domain in the ischemic myocardium.

The method of laser perforation is also developed in application to other human tissues and organs. The positive effect of laser revascularisation is known for the ischemic muscles of lower extremities, where it is implemented via an optical fibre with the lasers at the wavelength 0.98 and 1.06 μm [4]. After the laser optical fibre perforation of cirrhotic rat liver (wavelength 1.06 μm), the regeneration of the hepatic tissue with the signs of new microcapillaries and gall ducts formation in the region of laser channels was observed [5,6]. These studies were carried out according to the following scheme: the laser perforation of the biological object was carried out with the specified radiation power and exposure time. Then the histochemical and microscopic study of the tissue sections was performed, and the relation between the laser radiation parameters (power, exposure time) and the structural changes of the tissue was established. However, no information on the

laser-induced effects in the perforated region for these tissues is available. Other types of lasers are not used for these purposes at present time.

The thermal stimulation of angiogenesis is considered as the basic model of myocardium revascularisation using laser perforation [1]. The target for the laser-induced thermal angiogenesis induction can be the cell membranes. The interaction with the membrane short-lived microscopic domains (rafts) is a necessary stage of activating the key enzymes controlling the angiogenesis [7]. The differentiation of myoblasts in the process of muscle fibre regeneration is probably caused by the possibility of raft structure formation in the cell membranes [8]. The functioning and interaction of different types of cells comprising the liver in the process of regeneration is also largely dependent on the possibility of thermal induction of rafts in them [9]. The IR laser radiation enhances the fluidity of lipids in cell membranes *in vitro* [10], facilitating the modification of their microdomain raft structure [11]. The temperature of the phase transition of cell membranes from the unordered state to the ordered one depends on their composition and for natural lipids ranges from 38 to 66°C [12]. The creation of temperature fields initiating thermal induction of raft transition around the laser channels is a promising approach to the development of laser stimulation method for the regeneration of liver and muscle tissue.

The present paper is aimed at the study of the possibility to determine and control the location and parameters of the thermal stimulation zone in the tissue caused by laser perforation with an optical fibre at the wavelength 1.56 μm in application to the problem of laser-induced liver regeneration.

2 Materials and methods

As a source of radiation, we used the fibre LSP laser with the wavelength 1.56 μm (NPO "IRE-Polus") with the power up to 10 W, operating in the continuous-wave mode. The power of radiation at the output face of the fibre 600 μm in diameter was from 2 to 8 W, the velocity of the fibre movement into the tissue was changed stepwise from 0.1 mm/s to 1 mm/s. To measure the power at the fibre output we used the power meter (Coherent, Inc., USA).

The material for ex-vivo studies were the samples of liver from a one-year-old white pig.

The samples were placed on an immobile platform. The sample perforation was implemented by moving the fibre into the tissue using the motorised linear translator with the specified velocity. The straight-through perforation of biotissue samples was performed. After the perforation the samples were frozen, the longitudinal and transverse sections were prepared in the channel region, and the thermally damaged zone (TDZ) of the tissue was investigated microscopically around the laser channel, including the carbonisation and the coagulation zone (Fig. 1).

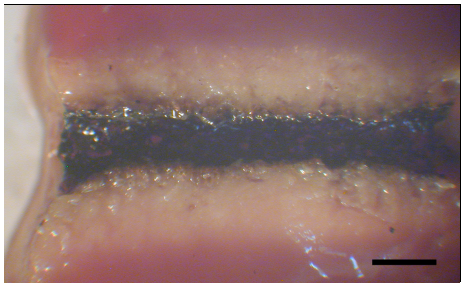

Fig. 1 A typical view of the thermally damaged zone (TDZ) of the tissue around the laser channel in the sample of liver in vitro after perforation with the optical fibre (the entrance of the fibre into sample occurs from the left), the scale bar corresponds to 1 mm.

The TDZ width was measured as the distance from the laser channel wall to the boundary of the coagulation zone, visually observed as the whitish tissue, its colour being a result of coagulation under the heating in the process of perforation up to the temperature 70°C [13]. The microscopy of TDZs was implemented using the MBS-10 microscope with 100× magnification.

The width of the thermal stimulation zone (TSZ) in the process of tissue regeneration corresponded to the temperature range 38-66°C [12] and was determined using the calculation method according to the developed theoretical model.

The temperature distribution over the tissue surface was measured using an infrared imager, the infrared camera FLIR A655sc (FLIR Systems, Inc. Sweden), with the resolution of 640×480 pixels at 50 Hz, 640×120 pixels at 200 Hz, and the response time 8 μs, operating in the wavelength range from 7.5 μm to 14 μm. The temperature sensitivity amounted to 50 mK within the temperature range (-20°C – +150°C). For comparison with the theoretical calculation, we measured the temperature in the process of fibre insertion into the sample at the outer side surface and at the face of the sample for the given distance from the fibre axis.

Fig. 2 presents a schematic diagram of the considered space domain, superimposed on the thermal image of the temperature distribution at the side surface of the biotissue sample separated from the fibre axis by the distance of 2-3 mm. The temperature distribution was measured along and across the axis of the optical fibre motion. The transverse distributions were measured at the fixed distances of 2 mm (Section 1) and 8 mm (Section 2) from the entrance (left-hand) surface of the sample at the moments, when the optical fibre reached these marks. Correspondingly, for different velocities of the optical fibre movement into the tissue sample, the transverse distributions were measured at different time intervals from the beginning of irradiation. For example, for the velocity 0.2 mm/s the time moments were t_1 = 10 s and t_2 = 40 s; for the velocity 0.5 mm/s they were t_1 = 4 s and t_2 = 16 s.

 doi: 10.18287/JBPE18.04.020302

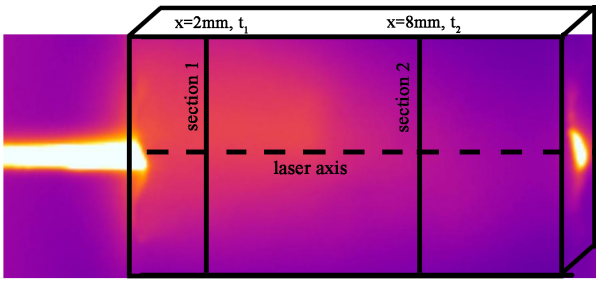

Fig. 2 Calculation scheme of moving the optical fibre into the tissue (from left to right) superimposed with the thermal image of temperature distribution. The boundaries of the biotissue sample and the sections 1 and 2 separated by 2 and 8 mm from the input surface of the sample are shown.

In the theoretical part of the study, in order to determine the thermal stimulation zones and their behaviour depending on the laser irradiation parameters, we constructed a theoretical model of heating the biotissue with the fibre, moving into it. The simulation of the liver tissue heating by the laser radiation is based on the heat conduction theory. We solved the heat conduction equation with the volume source, created by the laser radiation, damping with the depth according to the Booger-Lambert-Beer law, and expanding as the optical fibre is moved into the tissue.

The density of the incident energy flux at the biotissue surface, supplied by the optical fibre, has the Gaussian transverse spatial distribution with the effective beam radius that allows for the divergence of the beam with penetration depth. The divergence was approximated by a linear function determined from the comparison of numerical and experimental data in two sections, separated by the given distance.

For the numerical simulation, using the software package «Mathematica 5.0» the finite difference method and the Frankel-Dufort scheme were applied [14].

3 Theoretical model of laser perforation of biotissues using an optical fibre

The model is based on the heat conduction equation (1) with the moving source of heat $G(x, y, z, t)$, created by the laser radiation, delivered via the optical fibre with the diameter 600 μm, moved into the tissue with the velocity that can be varied from 0.1 mm/s to 0.5 mm/s

$$\frac{\partial T(x,\,y,\,z,\,t)}{\partial t} = a\left(\begin{array}{l}\dfrac{\partial^2 T(x,\,y,\,z,\,t)}{\partial x^2} + \\ + \dfrac{\partial^2 T(x,\,y,\,z,\,t)}{\partial y^2} + \\ + \dfrac{\partial^2 T(x,\,y,\,z,\,t)}{\partial z^2}\end{array}\right) + G(x,\,y,\,z,\,t), \quad (1)$$

where a is the thermal diffusivity.

A similar heat source was considered and the detailed description of the influence of different parameters of laser radiation on the result of thermal heating was presented in the paper [15], devoted to the design of the control system aimed at the conservation of the nasal septum functional properties in the laser reshaping procedure. The action of a similar heat source on the tissues of tendons [16-17] and sclera [18-19] of the eye was studied with thermomechanical stresses taken into account, and in Refs. [20-22] with the analogous source at the wavelength 1.56 μm the data on the biological tissue regeneration were obtained. The difference of the model used in the present paper from the earlier ones is the movement of the volume heat source.

In the present study, we solve the problem with moving source of radiation having the Gaussian distribution in the plane perpendicular to the direction of motion. The Booger-Lambert-Beer law with the effective absorption index κ (2) describes the damping of radiation with the depth of propagation into the biological tissue. The density of the incident energy flux at the sample surface has the Gaussian spatial distribution with the effective beam radius $r_0(x)$. The radiation passed through the optical fibre generates a thermal field that propagates in the liver. Due to the inhomogeneity of the biological tissue and multiple scattering inside it, the Gaussian source of heat expands with the motion into the sample. This expansion is considered by introducing the dependence of the effective radius $r_0(x)$ upon the coordinate x. In the first approximation for numerical simulation, this dependence was taken linear

$$G(x,y,z,t) = q(t,v)\exp\left[-\frac{y^2+z^2}{r_0(x)^2}\right]\frac{\kappa\exp(-\kappa x)}{c\rho}, \quad (2)$$

where $q(t,v)$ is the integral power of the laser radiation depending on time and the velocity of motion v of the heat source, c is the specific heat capacity, ρ is the density.

The boundary condition (3) corresponds to the continuity of heat flux and temperature at the boundary between two media, $x = h_m$:

$$\lambda_m \frac{\partial T^m(h_m,\,y,\,z,\,\tau)}{\partial x} = \lambda_{m+1}\frac{\partial T^{m+1}(h_m,\,y,\,z,\,\tau)}{\partial x}; \quad (3)$$
$$T^m(h_m,\,y,\,z,\,\tau) = T^{m+1}(h_m,\,y,\,z,\,\tau).$$

Here λ_m is the heat conductivity, m is the number of the considered layer.

For each considered layer of space m, the heat conduction equation can be written allowing for the form of the heat source and the reflection from the interface K_m^r between the media

$$\frac{\partial T(x,y,z,\tau)}{d\tau} - a_m \left(\begin{array}{l} \dfrac{\partial^2 T(x,y,z,\tau)}{\partial x^2} + \\ + \dfrac{\partial^2 T(x,y,z,\tau)}{\partial y^2} + \\ + \dfrac{\partial^2 T(x,y,z,\tau)}{\partial z^2} \end{array} \right) = \\ = (1-K_m^r) q(t,v) \exp\left[-\frac{y^2+z^2}{r_0(x)^2} \right] \frac{\kappa \exp(-\kappa x)}{c_m \rho_m}. \quad (4)$$

Here c_m is the layer heat capacity, ρ_m is its density, κ is the light absorption index.

For the biotissue region where the boiling of water is not achieved, only the thermal source is taken into account in the right-hand side of Eq. (4). With the increase of exposure time and the achievement of boiling temperature, the heat expenditures for evaporation become essential. The bulk growth of temperature in this region decelerates and the specific flow carried away by the vapour approaches the mean value of $(0.7 \div 0.8) * q(t,v)$, according to Libenson [23], which allows a correction of the right-hand side of the heat conduction equation near 100°C. In this case, a wave of evaporation propagates into the substance, the velocity of which increases, while the size of the heated domain $vt \approx \sqrt{at}$ gradually decreases. When the wave of evaporation overtakes the thermal wave, the role of heat conductivity is reduced to the determination of temperature before the steady-state evaporation front. Thus, the problem of localising the heat simulation zone, where the processes of angiogenesis are triggered at the cellular level (38-66°C) can be considered basing on Eqs. (1)–(3).

For the numerical modelling, we used the finite difference method and the three-layered Frankel-Dufort scheme for time variable. In the finite-difference form, the heat conduction equation for the numerical simulation is written as

$$\frac{T_{ix,iy,iz}^{j+1} - T_{ix,iy,iz}^{j-1}}{2dt} = \\ = a_m \left(\begin{array}{l} \dfrac{T_{ix+1,iy,iz}^{j} - T_{ix,iy,iz}^{j+1} - T_{ix,iy,iz}^{j-1} + T_{ix-1,iy,iz}^{j}}{(dx)^2} + \\ + \dfrac{T_{ix,iy+1,iz}^{j} - T_{ix,iy,iz}^{j+1} - T_{ix,iy,iz}^{j-1} + T_{ix,iy-1,iz}^{j}}{(dy)^2} + \\ + \dfrac{T_{ix,iy,iz+1}^{j} - T_{ix,iy,iz}^{j+1} - T_{ix,iy,iz}^{j-1} + T_{ix,iy,iz-1}^{j}}{(dz)^2} \end{array} \right) + \frac{(1-K_m^r)}{c_{vm}\rho_m} q(t,v) \times \\ \times \exp\left[-\frac{\left[(iy-1)dy - \frac{y_{\max}-y_{\min}}{2} \right]^2 + \left[(iz-1)dz - \frac{z_{\max}-z_{\min}}{2} \right]^2}{r_0(x)^2} \right] \times \\ \times \kappa_m \exp(-\kappa_m [ix-1] dx).$$

The temperature at the current step of the time evolution was expressed in terms of the temperature values at two preceding layers:

$$T_{ix,iy,iz}^{j+1} = T_{ix,iy,iz}^{j-1} \frac{1 - 2dta_m \left(\frac{1}{(dx)^2} + \frac{1}{(dy)^2} + \frac{1}{(dz)^2} \right)}{1 + 2dta_m \left(\frac{1}{(dx)^2} + \frac{1}{(dy)^2} + \frac{1}{(dz)^2} \right)} + \\ + 2dta_m \left(\begin{array}{l} \dfrac{T_{ix+1,iy,iz}^{j} + T_{ix-1,iy,iz}^{j}}{(dx)^2} + \\ + \dfrac{T_{ix,iy+1,iz}^{j} + T_{ix,iy-1,iz}^{j}}{(dy)^2} + \\ + \dfrac{T_{ix,iy,iz+1}^{j} + T_{ix,iy,iz-1}^{j}}{(dz)^2} \end{array} \right) + 2dt \frac{(1-K_m^r)}{c_{vm}\rho_m} q(t,v) \times \\ \times \exp\left[-\frac{\left[(iy-1)dy - \frac{y_{\max}-y_{\min}}{2} \right]^2 + \left[(iz-1)dz - \frac{z_{\max}-z_{\min}}{2} \right]^2}{r_0(x)^2} \right] \times \\ \times \kappa_m \exp(-\kappa_m [ix-1] dx).$$

The numerical problem was solved using the software package «Mathematica 5.0».

4 Discussion and comparison of experimental and numerical simulation results

Below we present the results of numerical simulation of temperature fields and the experiments with thermal imaging measurements of these fields at different velocities of the laser fibre moving into the tissue.

In the process of tissue perforation with the optical fibre, a layer of carbonised (charred) tissue is formed at the front face of the fibre, analogous to the carbonised zone around the channel. Its thickness at the fibre face was smaller than 80-100 μm, while the size of carbonisation zone around the laser channel amounted to 20-100 μm depending on the laser radiation power. As shown by direct measurements, the power change at the output fibre face covered with the carbonised tissue after the perforation does not exceed 7-10% of the initial power, i.e., not more than 10% of laser radiation is absorbed by the carbonised tissue at the fibre face. Therefore, in our calculations we did not take the absorption of radiation by the carbonised layer into account.

For the velocity of fibre motion 0.2 mm/s, we compared the experimental and theoretical temperature distribution curves (Fig. 3) and selected the rates of thermal source broadening with the depth, providing good agreement of theoretical and experimental results. The laser power at the face of the optical fibre was equal to 5 W.

 doi: 10.18287/JBPE18.04.020302

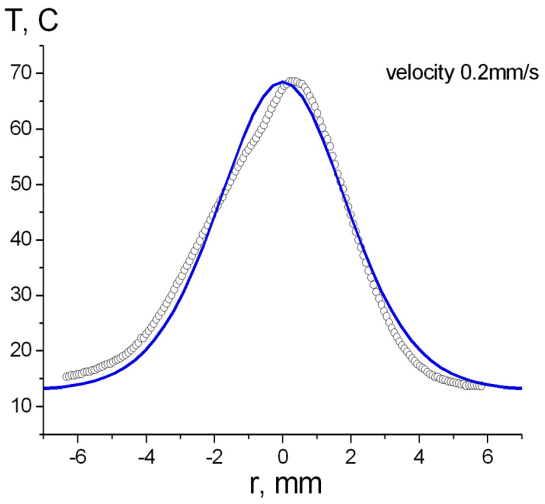

a

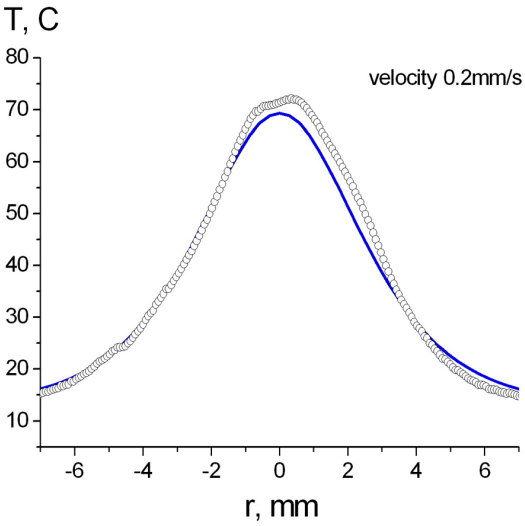

b

Fig. 3 Temperature fields at the distance 2 mm (in 10 s after the beginning of perforation) (a) and 8 mm (in 40 s after the beginning of perforation) (б) from the sample surface for the velocity of the fibre 0.2 mm/s. The empty circles show the data of thermal imaging and the solid curves plot the simulation results.

Basing on the selected rate of the heat source expansion, the temperature distribution curves for the velocity 0.5 mm/s were calculated and superimposed on the corresponding experimental curves. One can see good agreement between the computer simulation using the selected expansion rate of the heat source and the experiment (Fig. 4).

The temperature field was calculated at the back surface 20 s before the through perforation of the biotissue sample by the moving optical fibre. The results are confirmed well by the experimental data of thermal imaging (Fig. 5).

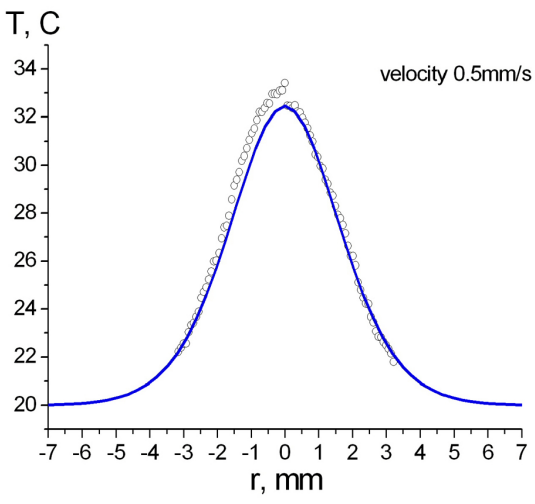

a

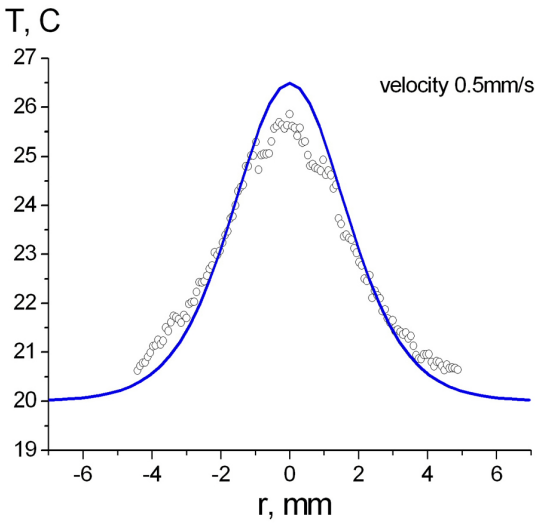

b

Fig. 4 Temperature fields at the distance 2 mm (in 4 s after the beginning of perforation) (a) and 8 mm (in 16 s after the beginning of perforation) (b) from the sample surface for the velocity of the fibre movement 0.5 mm/s. The empty circles show the thermal imaging data and the solid curves represent the simulation results.

We performed the calculation aimed at the determination of the TSZ position with respect to the axis of the laser channel and at the comparison with the experimental data. Fig. 6 presents the dependences of the TSZ width corresponding to the temperature range 38-66°C and the boundary of the zone, where the coagulation temperature was observed (70°C) on the radiation power for the motion of the fibre into the tissue sample with the velocity 0.5 mm/s. For comparison, the experimental data for the boundary of coagulation zone are presented.

 doi: 10.18287/JBPE18.04.020302

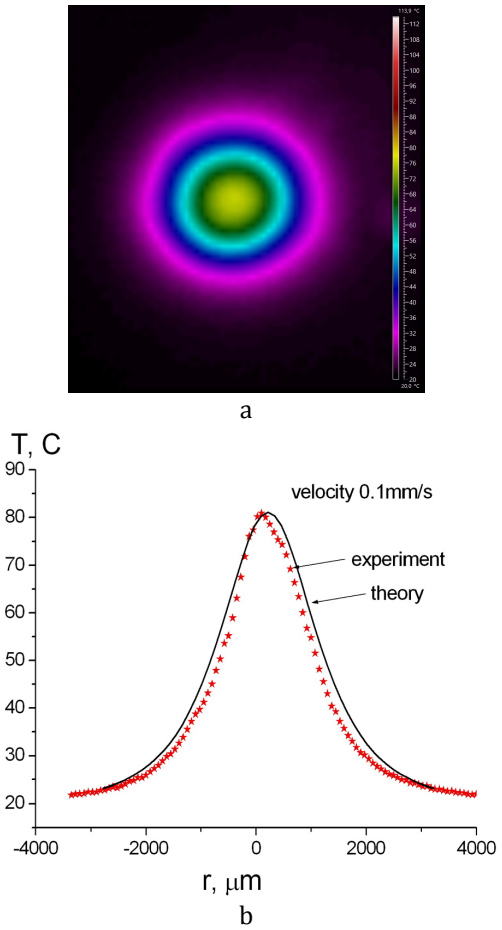

Fig. 5 (a) Temperature distribution at the back surface of the liver sample (perpendicular to the fibre axis) at the moment when the output face of the fibre moving with the velocity 0.1 mm/s was at the distance of 2 mm from this surface. (b) The asterisks show the data of thermal imaging and the solid curve shows the results of simulation.

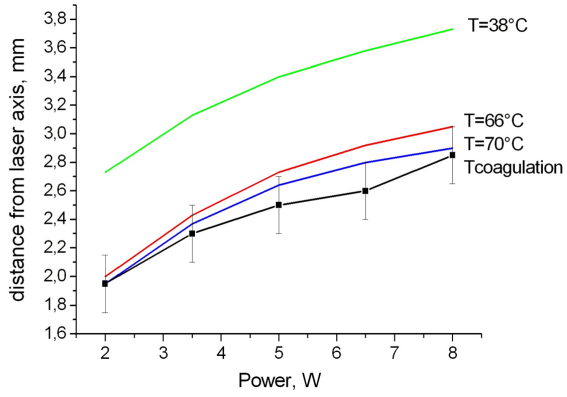

Fig. 6 Dependence of the TSZ width on the radiation power for the velocity of fibre movement into the biotissue sample equal to 0.5 mm/s. The experimental data for the coagulation zone boundary (Tcoagulation) are also presented.

Fig. 7 presents the calculated dependences of TSZ width and the boundary of coagulation zone on the velocity of the fibre movement into the biotissue for the radiation power 5 W.

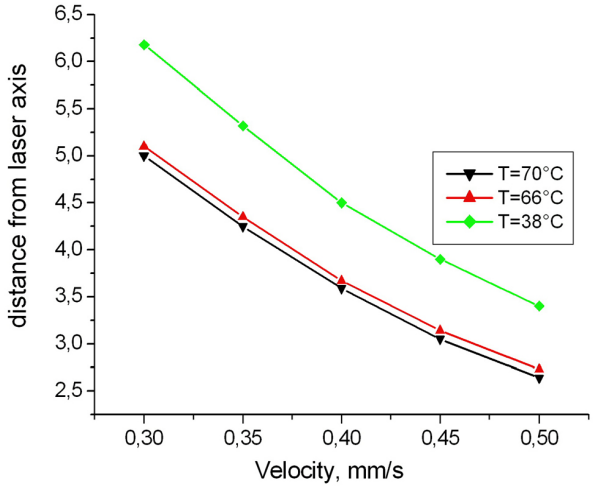

Fig. 7 Dependences of the TSZ width and the coagulation zone boundary position on the velocity of the optical fibre movement into the depth of biotissue at the power 5 W.

As follows from Fig. 6, good correlation is observed between the experimental and theoretical dependence for the tissue coagulation zone boundary. At the constant perforation velocity the TSZ width increases with the laser power and its boundary shifts into the tissue from the axis of the laser channel. At the constant power of radiation, the TSZ width decreases with the increase of the perforation velocity (Fig. 7), and its boundary shifts towards the axis of the laser channel.

5 Conclusions

The possibility to control the position and parameters of the zones of biotissue thermal stimulation depending on the conditions of the laser perforation in application to the problem of laser-induced regeneration of liver is investigated. For the fixed radiation power, with the increase of the fibre motion velocity the zones of thermal stimulation approach the axis of the laser channel. For the fixed velocity of the fibre motion, the same result is provided by the reduction of the laser radiation power, which offers the possibility of controlling the position of thermal stimulation zones.

Disclosures

All authors declare that there is no conflict of interests in this paper.

Acknowledgment

The work was carried out under support from the Federal Agency for Scientific Research (agreement No. 007-ГЗ/Ч3363/26) in the part of developing the experimental techniques and from the Russian Foundation for Basic Research (project No. 15-29-04816) in the rest part.

Mathematical model of skin autofluorescence induced by 450 nm laser

Dmitry N. Artemyev
Samara National Research State University, 34 Moskovskoye shosse, Samara 443086, Russia

e-mail: artemyevdn@gmail.com

Abstract. Optical methods are increasingly being used for the early diagnosis of skin cancer. This approach allows for detecting the component composition changes of tissue in a non-invasive manner. Autofluorescence spectroscopy is a sensitive method for tumor diagnosis and the method availability distinguishes it among other approaches. This work is devoted to fluorescence modeling of skin tissues induced by 450 nm radiation. A multilayer skin model was developed using a set of fluorophores (eumelanin, lipofuscin, riboflavin, beta-carotene, bilirubin) matched with excitation radiation. Model autofluorescence spectra of normal skin tissues of the northern phenotype and pathological changes were obtained. The results were compared with the results of previous experimental studies of *ex vivo* autofluorescence spectra of the skin and neoplasms. © 2018 Journal of Biomedical Photonics & Engineering.

Keywords: Autofluorescence; Monte Carlo Modeling; Skin Model; Skin Fluorophores; Optical Diagnostics.

Paper #3293 received 6 May 2018; revised manuscript received 10 Jun 2018; accepted for publication 16 Jun 2018; published online 30 Jun 2018. doi: 10.18287/JBPE18.04.020303.

References

1. A. D. Kaprin, V. V. Starinsky, and G. V. Petrova, "Malignant Tumors in Russia 2015 (Morbidity and Mortality)," Russia Ministry of health, Moscow (2017) [in Russian]. ISBN 978-5-85502-227-8.
2. V. P. Zakharov, I. A. Bratchenko, D. N. Artemyev, O. O. Myakinin, D. V. Kornilin, S. V. Kozlov, and A. A. Moryatov, "Comparative analysis of combined spectral and optical tomography methods for detection of skin and lung cancers," Journal of Biomedical Optics 20(2), 025003 (2015).
3. I. A. Bratchenko, D. N. Artemyev, O. O. Myakinin, Y. A. Khristoforova, A. A. Moryatov, S. V. Kozlov, and V. P. Zakharov, "Combined Raman and autofluorescence ex vivo diagnostics of skin cancer in near-infrared and visible regions," Journal of Biomedical Optics 22(2), 027005 (2017).
4. H. Lui, J. Zhao, D. McLean, and H. Zeng, "Real-time Raman spectroscopy for in vivo skin cancer diagnosis," Cancer Research 72(10), 2491-2500 (2012).
5. E. Borisova, L. Avramov, P. Pavlova, E. Pavlova, and P. Troyanova, "Qualitative optical evaluation of malignancies related to cutaneous phototype," Proceedings of SPIE 7563, 75630X (2010).
6. I. A. Bratchenko, D. N. Artemyev, O. O. Myakinin, M. G. Vrakova, K. S. Shpuntenko, A. A. Moryatov, S. V. Kozlov, and V. P. Zakharov, "Malignant melanoma and basal cell carcinoma detection with 457 nm laser-induced fluorescence," Journal of Biomedical Photonics & Engineering 1(3), 180–185 (2015).
7. V. V. Tuchin, Tissue Optics, Light Scattering Methods and Instruments for Medical Diagnostics, Third Edition, SPIE, Bellingham (2007). ISBN: 9781628415162.
8. I. V. Meglinski, A. V. Doronin, "Monte Carlo Modeling of Photon Migration for the Needs of Biomedical Optics and Biophotonics," Chap. 1 in Advanced Biophotonics: tissue optical sectioning, 1–72 (2013).
9. A. Yu. Setejkin, I. V. Krasnikov, Application of the Monte Carlo method for biophotonics problems, AmGU publisher, Blagoveshchensk (2014) [in Russian]. ISBN 978-5-93493-224-5.
10. C. Zhu, Q. Liu, "Review of Monte Carlo modeling of light transport in tissues," Journal of Biomedical Optics 18(5), 050902 (2013).
11. A. J. Welch, C. Gardner, R. Richards-Kortum, E. Chan, G. Criswell, J. Pfefer, and S. Warren, "Propagation of fluorescent light," Lasers in Surgery and Medicine 21(2), 166-78 (1997).

12. F. Jaillon, W. Zheng, and Z. Huang, "Beveled fiber-optic probe couples a ball lens for improving depth-resolved fluorescence measurements of layered tissue: Monte Carlo simulations," Physics in Medicine and Biology 53(4), 937–951 (2008).
13. K. B. Sung, H. H. Chen, "Enhancing the sensitivity to scattering coefficient of the epithelium in a two-layered tissue model by oblique optical fibers: Monte Carlo study," Journal of Biomedical Optics 17(10), 107003 (2012).
14. Y. P. Sinichkin, S. R. Utz, A. H. Mavliutov, and H. A. Pilipenko "In Vivo Fluorescence Spectroscopy of the Human Skin: Experiments and Models," Journal of Biomedical Optics 3(2), 201-211 (1998).
15. H. Zeng, C. MacAulay, D. I. McLean, and B. Palcic, "Reconstruction of in vivo skin autofluorescence spectrum from microscopic properties by Monte Carlo simulation," Journal of Photochemistry and Photobiology B: Biology 38(2–3), 234–240 (1997).
16. Q. Liu, C. Zhu, and N. Ramanujam, "Experimental validation of Monte Carlo modeling of fluorescence in tissues in the UV-visible spectrum," Journal of Biomedical Optics 8(2), 223-236 (2003).
17. V. V. Dryemin, Method and device for diagnosis of tissue metabolism disorders based on optical spectroscopy (for example, diabetes mellitus), Diss. Cand. Sci. in Tech., Oryol State University, Oryol, Russia, 2017 [in Russian].
18. I. V. Meglinski, S. J. Matcher, "Computer simulation of the skin reflectance spectra," Computer Methods and Programs in Biomedicine 70(2), 179-186 (2003).
19. S. L. Jacques, "Optical properties of biological tissues: a review," Physics in Medicine and Biology 58(11), R37–R61 (2013).
20. A. N. Bashkatov, E. A. Genina, and V. V. Tuchin, "Optical properties of skin, subcutaneous, and muscle tissues: a review," Journal of Innovative Optical Health Sciences 4(1), 9–38 (2011).
21. E. G. Borisova, L. P. Angelova, and E. P. Pavlova, "Endogenous and Exogenous Fluorescence Skin Cancer Diagnostics for Clinical Applications," IEEE Journal of Selected Topics in Quantum Electronics 20(2), 211–222 (2014).
22. K. Koenig, I. Riemann, "High-resolution multiphoton tomography of human skin with subcellular spatial resolution and picosecond time resolution," Journal of Biomedical Optics 8(3), 432 (2003).
23. A. C. Croce, G. Bottiroli, "Autofluorescence spectroscopy and imaging: a tool for biomedical research and diagnosis," European Journal of Histochemistry 58(4), (2014).
24. S. P. Nighswander-Rempel, J. Riesz, J. Gilmore, J. P. Bothma, and P. Meredith, "Quantitative Fluorescence Excitation Spectra of Synthetic Eumelanin," Journal of Physical Chemistry B 109(43), 20629-20635 (2005).
25. M. E. Darvin, I. Gersonde, M. Meinke, W. Sterry, and J. Lademann, "Non-invasive in vivo determination of the carotenoids beta-carotene and lycopene concentrations in the human skin using the Raman spectroscopic method," Journal of Physics D: Applied Physics 38(15), 2696–2700 (2005).
26. V. D. Silva, J. N. Conceição, I. P. Oliveira, C. H. Lescano, R. M. Muzzi, O. P. S. Filho, E. C. Conceição, G. A. Casagrande, and A. R. L. Caires, "Corrigendum to 'Oxidative Stability of Baru (Dipteryx alataVogel) Oil Monitored by Fluorescence and Absorption Spectroscopy," Journal of Spectroscopy 2015, 748673 (2015).
27. B. Thorell, "Flow-cytometric monitoring of intracellular flavins simultaneously with NAD(P)H levels," Cytometry 4(1), 61–65 (1983).
28. D. M. Gore, P. French, D. O'Brart, C. Dunsby, and B. D. Allan, "Two-Photon Fluorescence Microscopy of Corneal Riboflavin Absorption Through an Intact Epithelium," Investigative Ophthalmology & Visual Science 56(2), 1191–1192 (2015).
29. B. Zietz, A. N. Macpherson, and T. Gillbro, "Resolution of ultrafast excited state kinetics of bilirubin in chloroform and bound to human serum albumin," Physical Chemistry Chemical Physics 6(19), 4535 (2004).
30. N. Nandakumar, S. Buzney, and J. J. Weiter, "Lipofuscin and the Principles of Fundus Autofluorescence: A Review," Seminars in Ophthalmology 27(5–6), 197–201 (2012).
31. N. M. Haralampus-Grynaviski, L. E. Lamb, C. M. R. Clancy, C. Skumatz, J. M. Burke, T. Sarna, and J. D. Simon, "Spectroscopic and morphological studies of human retinal lipofuscin granules," Proceedings of the National Academy of Sciences 100(6), 3179–3184 (2003).
32. A. Periasamy, and R. M. Clegg, Flim Microscopy in Biology and Medicine, CRC Press, Taylor & Francis Group, Boca Raton (2009). ISBN 9781420078909.
33. G. F. M. Ball, "Flavins: Riboflavin, FMN and FAD (Vitamin B2)," Chap. 12 in Vitamins: Their Role in the Human Body, 289–300 (2008).
34. R. L. Barnhill, M. Piepkorn, and K. J. Busam, Pathology of Melanocytic Nevi and Malignant Melanoma, Springer, Berlin (2004). ISBN 978-0-387-21619-5.
35. A. A. Efimov, G. N. Maslyakova, "Lipofuscin role in involutive and pathological processes," Saratov Journal of Medical Scientific Research 5(1), 111-115 (2009) [in Russian].
36. A. Skoczyńska, E. Budzisz, E. Trznadel-Grodzka, and H. Rotsztejn, "Melanin and lipofuscin as hallmarks of skin aging," Advances in Dermatology and Allergology 2, 97–103 (2017).

37. P. A. van den Berg, J. Widengren, M. A. Hink, R. Rigler, and A. J. W. Visser, "Fluorescence correlation spectroscopy of flavins and flavoenzymes: photochemical and photophysical aspects," Spectrochimica Acta Part A: Molecular and Biomolecular Spectroscopy 57(11), 2135–2144 (2001).
38. A. Dontsov, A. Koromyslova, M. Ostrovsky, and N. Sakina, "Lipofuscins prepared by modification of photoreceptor cells via glycation or lipid peroxidation show the similar phototoxicity," World Journal of Experimental Medicine 6(4), 63 (2016).
39. A. Hennessy, C. Oh, B. Diffey, K. Wakamatsu, S. Ito, and J. Rees, "Eumelanin and pheomelanin concentrations in human epidermis before and after UVB irradiation," Pigment Cell Research 18(3), 220–223 (2005).
40. D. L. Fox, Biochromy, Natural Coloration of Living Things, University of California Press, Berkley and Los Angeles (1979). ISBN 0-52003699-9.
41. A. Vahlquist, J. B. Lee, G. Michaëlsson, and O. Rollman, "Vitamin A in Human Skin: II Concentrations of Carotene, Retinol and Dehydroretinol in Various Components of Normal Skin," Journal of Investigative Dermatology 79(2), 94–97 (1982).
42. A. Knudsen, R. Brodersen, "Skin colour and bilirubin in neonates," Archives of Disease in Childhood 64(4), 605–609 (1989).
43. I. A. Novikov, Y. O. Grusha, and N. P. Kiryshchenkova, "Autofluorescence diagnostics of skin and mucosal tumors," Annals of ophthalmology 129(5), 147-153 (2013).
44. K. S. Litvinova, D. A. Rogatkin, O. A. Bychenkov, and V. I. Shumskiy, "Chronic Hypoxia as a Factor of Enhanced Autofluorescence of Endogenous Porphyrins in Soft Biological Tissues," Proceedings of SPIE 7547, 75470D (2010).
45. M.-A. Mycek, B. W. Pogue, Handbook of biomedical fluorescence, Marcel Dekker Inc., New York (2003). ISBN: 0824709551
46. K. Konig, H. Meyer, and H. Schneckenburger, "The Study of Endogenous Porphyrins in Human Skin and Their Potential for Photodynamic Therapy by Laser Induced Fluorescence Spectroscopy," Lasers in Medical Science 8, 127-132 (1993).
47. E. Borisova, P. Pavlova, E. Pavlova, P. Troyanova, and L. Avramov, "Optical Biopsy of Human Skin – A Tool for Cutaneous Tumours' Diagnosis," International Journal Bioautomation 16(1), 53-72 (2012).

1 Introduction

Skin cancer is one of the most common forms of cancer in Russia and the world [1]. There are three main types of skin cancer: basal cell carcinoma (BCC), squamous cell carcinoma (SCC) and malignant melanoma (MM). Optical methods have been extensively used to diagnose neoplasms, since they are non-invasive and can be applied to real-time analysis [2-4]. One of the promising methods of non-invasive skin lesion examination is the analysis of the tissue intrinsic fluorescence. Laser induced autofluorescence (AF) spectroscopy is an effective method for early detection of skin cancer because of its high sensitivity, simple measurement technique, and the absence of contrast agents in the studied tissue [5]. Economic efficiency of AF spectroscopy for cancer diagnosis is an important factor in the possible use of the method in clinical studies.

The empirical analysis allows for distinguishing the diseased tissue, but in many cases, it is impossible to establish a clear connection between the final cancer diagnosis and biochemical changes in malignant tissues. For example, the registered fluorescence spectrum can be analyzed to determine the spectral contributions of constituent components to obtain the concentration of individual fluorophores. Nevertheless, the tissue is a multi-scattering medium, and fluorescence depends on various factors: the concentration of fluorophores, their localization, scattering and absorption of other chromophores, the geometry of the excitation / collection probe, and others. These effects can distort the shape of the spectrum and radiation intensity. For example, significantly altered AF spectra will be recorded for two skin tissues samples of different phenotypes with the same composition and concentration of fluorophores, due to the absorbing properties of melanin.

A proper measurement evaluation of fluorescence intensity in healthy tissue and pathology areas will be possible if the penetration depth of the probing radiation is known. This fact would provide information about fluorophores and blood vessels (upper or deep plexus of blood vessels) involved in the signal shaping.

Recent advances in computer modeling are an essential tool for studying the biological basis of the registered signals in the fluorescence studies. They contribute to better identification of important fluorophores present in specific tissues. The purposes of the study are qualitative assessment, modeling the autofluorescence spectral characteristics changes of healthy skin and tumors induced by 450 nm laser, and obtained results comparing with a previously experimentally registered AF spectra within this range [3, 6].

2 Modeling methods of skin autofluorescence

2.1 Modeling the light in tissues by Monte Carlo method

The mathematical description of light absorption and scattering characteristics may be performed in two ways: using analytical theory or radiation transfer theory (RTT). The analytic theory is based on the Maxwell equations and is the most fundamental approach. However, its use is limited by difficulty of accurate analytical solutions obtaining. On the other hand, the radiation transport theory estimates the transfer of photons through absorbing and scattering media, without considering Maxwell's equations. The RTT is widely used to describe the interactions of optical radiation in tissue. It has been experimentally confirmed in many cases that RTT predictions are sufficient [7-9].

The stationary equation of the radiation transfer theory for monochromatic light is studied in details in the book [7]. It describes the average power change of the flux density at a certain point and in a certain direction, taking into account the scattering properties of the medium. The main challenge of RTT is diffuse component definition of the beam intensity, since scattering of photons is random. Therefore, different approximations are used, according to the intensity change is caused by the absorption or scattering of light.

Several approximation classes have been proposed in recent decades, including analytical models based on the theory of probabilistic photon migration, Kubelka-Munk theory, diffusion approximation theory, and a combination of various analytical methods. The advantage of analytical models is a relatively simple form of solution, but specified boundary conditions are required. Alternative approaches are various modifications of the Monte Carlo method. It is able to take into account the probe geometry and the complex structure of the tissue. However, this method requires relatively high processing power.

Radiation transport in tissues is modeled by the steps tracking of photon random walk using the Monte Carlo (MC) method [10]. To simulate fluorescence, an additional parameter – the quantum yield is included to describe the probability that an absorbed photon can be converted to a fluorescent photon at a different wavelength [11]. The initial direction of the fluorescent photon is isotropic due to the nature of the fluorescent radiation. The absorbing and scattering properties of the tissue model will influence on the fluorescence intensity in addition to the quantum yield and lifetime. Fluorescence modeling is usually more time consuming task than simulating diffuse reflection due to the additional propagation of fluorescent photons.

The most common application of the MC method in tissue optics is the modeling of optical measurements, such as diffuse reflection, transmittance and fluorescence for a given tissue model and the geometry of illumination / collection probe [12, 13].

2.2 Review of Monte Carlo models of skin autofluorescence in the visible region

It is useful to consider the basic approaches of the MC models construction for AF spectrum registration of skin on the example of the following works. Ref. [14] presented the results of an experimental study of the autofluorescence spectra of human skin *in vivo* induced by UV radiation (337 nm) and external mechanical pressure applied to the skin. These results were compared with the results of Monte Carlo simulation of the skin autofluorescence with various blood content. The proposed skin model made it possible to evaluate changes in the blood and melanin content. The skin model consisted of four layers. The fluorescent properties of the model were determined by melanin, hemoglobin, and collagen. In fact, collagen was only chosen as the fluorophore, melanin and hemoglobin were absorbers in the path of the AF signal. In this model, the authors ignored epidermal fluorescence because of the low contribution of fluorescent photons passing through the dermis.

The contribution of each layer to the AF spectrum of skin registered *in vivo* was shown in Ref. [15]. A standard seven-layer model (stratum corneum, epidermis, papillary dermis, upper vascular plexus, reticular dermis, deep plexus of vessels, dermis) was used. The AF spectra for each layer were registered using a microscope and excited laser with a wavelength of 442 nm. The contribution of each layer to the resulting skin AF spectrum was assessed in the simulation, rather than the effect of individual fluorophores.

The effect of individual fluorophores on the final AF spectrum was demonstrated in Ref. [16]. The aim of the work was experimental confirmation of MC fluorescence modeling in turbid phantom models. A simulation of the absorption and scattering coefficients effect on fluorescence of a turbid medium was carried out. The phantom skin model consisted of three components: two fluorophores (flavin adenine dinucleotide and green fluorescent protein) and one absorber (India ink). The excitation wavelength of 460 nm was matched with the excitation maxima of both fluorophores. Optical properties and the quantum yield of fluorescence measured on tissue phantoms were experimentally obtained to MC simulation. The results of MC simulation showed a good agreement between the model and experimentally measured results.

In another paper on the AF modeling of tissue using a fiber-optic sensor [17], real skin fluorophores have been used. Fluorescence was excited by 450 nm radiation. NADH and collagen were chosen as fluorophores, although their excitation peak was shifted to the shorter wavelength range of 330-340 nm. The multilayer skin model included: stratum corneum, epidermis, papillary dermis, reticular dermis and was

implemented in the optical modeling system TracePro. The effect of melanin on the AF spectrum was also taken into account.

In the reviewed models, the choice of fluorophores was not obvious and modeling of the skin pathological stages was not performed. A detailed analysis of the possible skin components (fluorophores and chromophores) for modeling and their spectral characteristics are described in the following paragraphs.

3 Multilayer skin model for autofluorescence induced by 450 nm laser

Highlights were taken into account in constructing of skin AF model (a set of layers, fluorophores) based on an analysis of existing models and the literature. A wavelength of 450 nm was chosen to excite AF and compare the model results with experimentally registered AF of skin and neoplasms. The modeling environment was TracePro Expert - 6.0.2, Lambda Research Corporation. Multilayer skin model was designed. The main difference of the proposed model was a set of fluorophores for skin AF modeling induced by 450 nm radiation. The features of the absorption spectra (the maximum value located in the range 440-460 nm) determined the choice of each fluorophore.

To obtain a fluorescent response, human skin was represented as a model consisting of five planar layers: epidermis, papillary dermis, upper plexus of microvessels, reticular dermis and deep vascular plexus [7, 18]. The thickness of individual skin layers: the epidermis – 100 μm, the papillary dermis – 200 μm, the surface plexus of microvessels – 100 μm, the reticular dermis – 600 μm and the deep plexus of the vessels – 200 μm. To simulate AF the skin area was selected with the size of 40 mm × 40 mm.

The optical characteristics of individual layers were repeatedly studied [7, 14, 15, 19, 20]. The absorption and scattering coefficients, anisotropy and refractive indices of each layer for normal skin and neoplasms were presented in the book [7]. It is also necessary to set the following parameters for fluorescence modeling: 1) quantum yield, 2) molar extinction coefficient, 3) molar concentration, 4) excitation spectra, 5) emission spectra. The values of relative absorption, excitation, and emission must be normalized to import data in the TracePro environment.

Since the fluorescent properties of the skin are determined by the fluorescent properties of the fluorophores contained in layers, the choice of components is a key moment in the modeling of the skin AF signal. Most studies to detect and evaluate AF signals of skin and neoplasms are performed using radiation in the spectral range of 330-450 nm [21]. The excitation spectra of most endogenous fluorophores, such as structural proteins, coenzymes, pigments, endogenous porphyrins, are located in this spectral range. Excitation in the 280-330 nm region was used to study amino acids such as tryptophan and tyrosine. Their fluorescent signal is correlated with the tissue health. Endogenous fluorophores were chosen with an absorption maximum in the 440-460 nm region, which play an important role in the formation of fluorescent properties of normal and pathological skin tissues, based on the analysis of spectral characteristics (excitation and emission spectra). Spectral data and fluorescent properties (quantum yield, peak of molar extinction) were selected according to the analysis of review articles on the skin intrinsic fluorescence [21-23], and papers devoted to the investigation of individual skin components fluorescence [24-31]. Part of the spectral data was obtained using the OMLC web resource (https://omlc.org/index.html), which provides databases, software, articles and free web guides on biomedical optics, supported by Scott Prahl and Steven Jacques. The following fluorophores were chosen to the designed model: melanin (absorption range of 250-1100 nm), carotenoids (absorption range of 400-550 nm with maximum values at 440 and 480 nm), flavins (absorption range of 300-500 nm with maximum values at 370 and 445 nm), bilirubin (absorption range of 300-600 nm with a maximum value of 450 nm) and lipofuscin (absorption range of 430-600 nm with a maximum value of 480 nm).

3.1 Skin fluorophores

Each fluorophore is discussed in detail in the presented model. Melanin is a high molecular weight pigment that is synthesized in specialized cells called melanocytes, which are located in the basal cell layer [32].

Carotenoids are natural organic pigments of yellow, orange or red color. Carotenoids are antioxidants in the human body that come with nutrition. Natural sources of carotenoids are a mixture of lycopene, beta-carotene, alpha-carotene, lutein, and zeaxanthin, which can be converted into each other. Beta-carotene was chosen as an example of carotenoids in the model. It is one of the chromophores of the upper dermis layers [20, 25].

Flavins are complex enzymes, the prosthetic groups of which are riboflavin derivatives [33]. Riboflavin is a biologically active substance that plays an important role in health support. The biological role of riboflavin is determined by the occurrence of its derivatives: flavin mononucleotide (FMN) and flavin adenine dinucleotide (FAD), which are part of a large number of important oxidation-reduction enzymes as coenzymes. In the skin, flavins are located in the basal layer and dermis [32].

Bilirubin is a bile pigment, one of the main components of bile in humans and animals. It is formed normally as a result of the proteins cleavage containing heme: hemoglobin, myoglobin, and cytochrome. Hemoglobin exhibited absorbing properties and contained in the dermis and blood [20].

Lipofuscin is a yellow-brown, intracytoplasmic autofluorescent pigment, consisting of a glycolipoprotein matrix, it contains in all tissues and organs of human [34]. Lipofuscin is also called aging pigment, which accumulates in the skin with age. But,

the accumulation of lipofuscin can be associated with pathological processes in the body [35]. Lipofuscin has similar properties to melanin for dermatology specialists, but lipofuscin has a more intense fluorescent response [34, 36]. Lipofuscin was considered as a fluorophore in the modeling of non-melanoma neoplasms.

Based on the above-described data of fluorophores, the fluorescent properties of the epidermis were characterized by eumelanin located in the lower part of the layer. The fluorescent properties of the dermis are determined by beta-carotene and flavins localized in the upper and lower layers, respectively. The fluorescent properties of the dermis with superficial plexus of vessels were characterized by bilirubin. Lipofuscin in the modeling of the skin pathologies was placed in the upper layer of the epidermis. In the simulation of pigmented tumors (malignant melanoma) eumelanin with fold increased content was localized in the upper layers of the epidermis. The final distribution of fluorophores over the skin layers in the model is shown in Fig. 1.

To simulate fluorescence, the fluorescent properties of the components were set: the quantum yield, the peak of molar extinction. In addition to fluorescent properties, a possible fluorophore concentration in the skin was determined. The parameters of the fluorophores used in the model are presented in Table 1 [24, 29, 31, 37, 38].

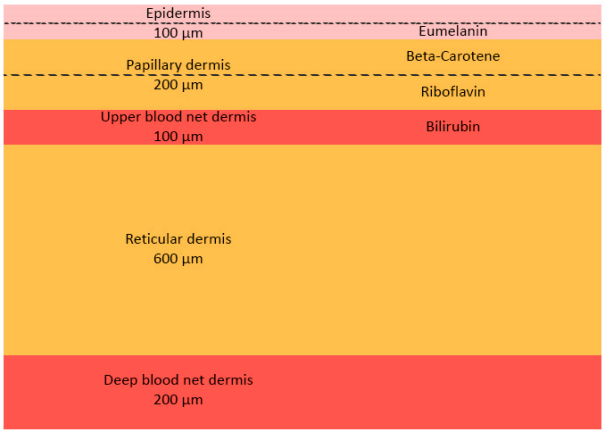

Fig. 1 Fluorophores localization in the multilayer model of healthy skin.

Table 1 Fluorescent properties of skin components.

Fluorophore	Quantum yield, γ	Peak of molar extinction, ε [l/mol·cm]	Molar concentration, C_{mol}, [mol/l]	Absorption coefficient, μ_a [cm^{-1}]
Eumelanin	0.0004	2500-3000	$0.88 \cdot 10^{-2}$	10
Lipofuscin	0.01	31 000	10^{-3}	23.6
Riboflavin (Flavins)	0.26	13 153	$6.4 \cdot 10^{-5}$	0.4
Beta-Carotene (Carotenoids)	0.0001	138 590	$2.3 \cdot 10^{-5}$	2.6
Bilirubin	0.003	55 016	$1.9 \cdot 10^{-4}$	10.5

The molar concentrations of fluorophores characteristic for the skin were taken from Refs. [38-42]. The table indicates that the absorption coefficient, which is directly proportional to the product of the molar concentration and the peak of the molar extinction, takes the highest values for eumelanin, lipofuscin and bilirubin. These components are mainly responsible for the absorption of radiation. Taking into account the quantum yield of fluorophores, the fluorescent contribution of each of them was estimated. Flavins and lipofuscin exhibit the strongest fluorescent properties.

3.2 Model of the optical scheme for skin fluorescence registration

The common optical scheme was used for registration of the skin fluorescent response. The scheme is shown in Fig. 2.

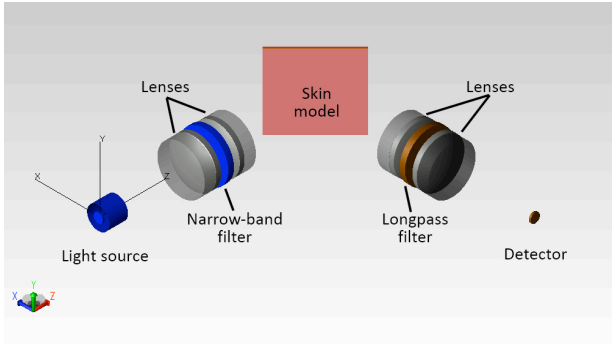

Fig. 2 Model of the optical scheme for skin fluorescence registration.

This optical scheme is standard for registration of samples fluorescence in TracePro. It consists of a detector, two focusing systems and a light source at 450 nm with a deflector for less scattering of rays. Each focusing system includes two lenses and a filter. The focusing system, which is closer to the source, is a

monochromator and serves to extract the radiation with a narrow wavelength. The second focusing system contains a longpass filter to suppress the probe radiation. The transmission and absorption characteristics of the filters elements and optical glass were matched for a wavelength of 450 nm (narrow-band filter - FF01-448/20, longpass filter - Di02-R442). The light source and the detector are perpendicular to each other to prevent the detector illuminating by the scattered radiation from the source.

4 Results and discussion

The depth of radiation penetration with a wavelength of 450 nm was initially analyzed in our model. This fact should be reviewed since the results of model experiments in published papers [15, 17] were applied for a combination of layers or for a limited set of fluorophores, respectively. The simulation results are shown in Fig. 3, each point corresponds to the average value of the radiation power at the upper boundary of each layer. The figure indicates that only 11% of the initial value (average power at the upper border of the epidermis) remains at the upper boundary of the reticular dermis (400 μm). And only 4% of radiation power falls on the layer with the deep plexus of the vessels. It follows that the main part of the incident radiation flux is localized in the three upper layers of the skin to 400 μm (epidermis, papillary dermis, surface plexus of vessels) in which the fluorophores under consideration are located. The obtained dependence is well correlated with the results of modeling in [15, 17]. In the work of Zeng group [15] the fluorescent properties of each layer were set by experimentally registered spectra and the propagation of 442 nm radiation was simulated. The main part of the radiation decayed to 300 μm, and at a depth of 570 μm, radiation was practically absent. In Ref. [17], radiation with a wavelength of 450 nm was also concentrated in the upper layers, the depth reached 450-500 μm and penetrated into the epidermis, the papillary dermis and captured the upper vascular plexuses. At the same time, the results of MC modeling were confirmed by analytical calculations, the difference was not more than 5%.

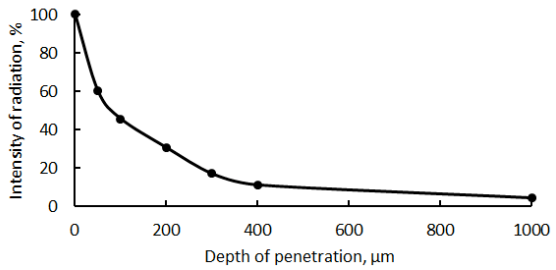

Fig. 3 The average power dependence of the incident radiation with a wavelength of 450 nm from the penetration depth in the skin model.

The main task of this work was skin model development using matched fluorophores for comparison with the experimental AF spectra of skin and neoplasms induced by 457 nm laser [6]. In Ref. [6], the analyzed spectral range of the registered values was shifted to the long-wavelength region relative to the excitation wavelength. Therefore, the AF response was modeled in the range of 540-720 nm for comparison with the experimental results. The signal in the near-IR region (720-750 nm) was not considered, since the last two intensity values (690 and 715 nm) were close to zero. The multilayer skin model was developed for the northern phenotype (concentration of eumelanin in the lower layer of the epidermis was $0.88 \cdot 10^{-2}$ mol/l). To model lesions in the skin model, the additional fluorophore was localized in the upper layers of the epidermis. For "tumor" model lipofuscin concentration was $0.4 \cdot 10^{-3}$ mol/l, for malignant melanoma the concentration was 10^{-1} mol/l. The simulation results are shown in Fig. 4.a, which are compared with the characteristic experimental AF spectra of basal cell carcinoma, malignant melanoma and healthy skin (Fig. 4.b).

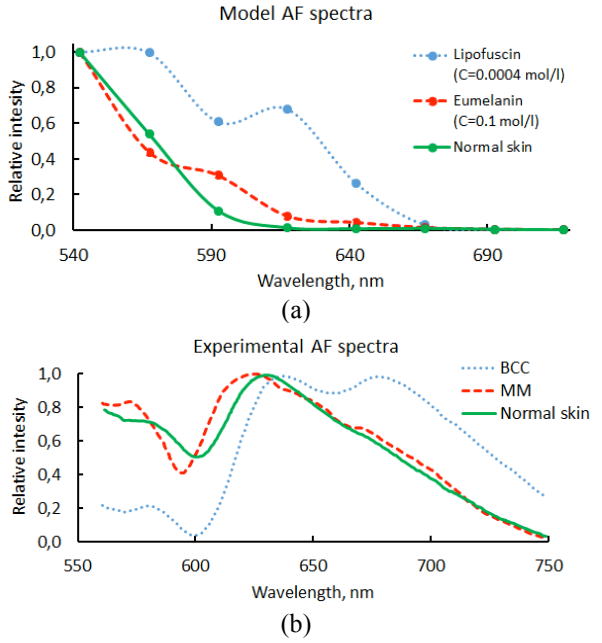

Fig. 4 Normalized model AF spectra of normal skin, tumor (lipofuscin) and malignant melanoma (eumelanin) for the northern phenotype (a) and experimental AF spectra of healthy skin, basal cell carcinoma and malignant melanoma (b).

Despite the small number of points, the figure highlights the characteristic common features: the relative intensity increase of the "tumor" AF signal in comparison with normal skin and "MM"; displacement of the "tumor" maximum in the long-wave region (620-640 nm); the presence of two characteristic peaks in the "tumor" spectrum (560 and 625 nm); a close arrangement for normalized spectra of normal skin and "MM". As was shown in Ref. [6], the positions and the maxima intensities of the AF spectra can provide information on the chemical composition of the examined samples. Thus, these features indicate the

changes in the pathological neoplasms compared to healthy skin. The main fluorophores emitting in the spectral range 550-700 nm are lipopigments, flavins and porphyrins [43, 44]. Lipids and flavins form the peak in the region 570-590 nm. Lipopigments have an absorption maximum at 340 nm and an emitting maximum at 560 nm. Flavins are characterized by strong absorption in a wide range from 200 to 500 nm with strong absorption maxima at 220, 260 nm, less absorption at 380, and 460 nm. The maximum intensity of flavin emission is located in a band centered at 555 nm [45]. Porphyrins are characterized by wide absorption in the region of 300-470 nm with a maximum value in the 400-410 nm band. The emission of porphyrins has a complex shape with two maxima around 615-630 and 660-670 nm [43, 44, 46]. Thus, the local maximum of AF spectra observed for the 560-570 nm band is characterized by the presence of flavins and lipopigments in the skin tissues, and the porphyrins determine the shape of the AF spectra in the red region of the spectrum.

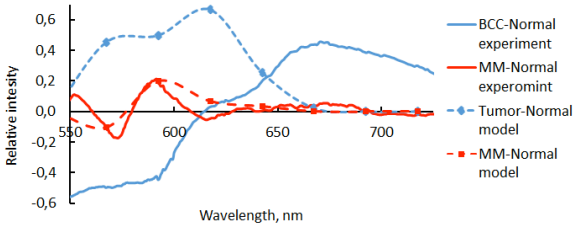

Fig. 5 The intensities changes of neoplasms normalized AF spectra relative to normal skin in model (dashed line) and experimental studies (solid line).

In this study, it was important to determine the fluorophores responsible for the intensity changes of the neoplasms AF spectra compared to normal skin. To analyze these dependence, normal skin spectrum was subtracted from the values of the neoplasms intensities for modeling and experimental study. Before subtraction, the experimental values were shifted to the shortwave region by 15 nm due to the calibration of the spectrometer. The obtained dependence of the AF spectra intensities changes is shown in Fig. 5. Fig. 5 indicates good qualitative agreement of the model results for normal skin and MM AF spectra with the experimental results. The greatest changes of the intensities were characteristic for the 580-600 nm band in both cases. The difference in the intensities of the normalized spectra in this band in the model and in the experiment does not exceed 20%. And the largest deviations of model values from the experiment do not exceed 10% over the entire spectral range. The modeling results of intensities change for tumor relative to normal skin are in poor agreement with experiment. For model values of AF tumor spectra, an increased intensity in the range of 550-640 nm was characteristic, and an inverse trend was observed for the BCC experimental study. This result figures out that model tumor can not be a BCC. The increased values of AF intensity in comparison with normal skin for the examined area are characteristic for squamous cell carcinoma [47].

The shape of the AF spectra differs between the model and the experiment. This is primarily due to the limited number of fluorescence sources (points on the abscissa axis) and an incomplete set of fluorophores. The model did not consider fluorophores whose absorption maxima do not locate within the 440-460 nm band. However, the part of radiation can be absorbed by fluorophores and re-emitted in the considered spectral range. Porphyrin is a fluorophore that can make significant changes to the model AF spectrum. This fluorophore was not presented in the model due to the shift of the absorption maximum to the short-wave region of the spectrum (400-410 nm).

The simulation results confirmed the differences of the pathology spectra in comparison with healthy tissue may be caused by different concentrations of melanin, flavins and lipopigments, while bilirubin and carotenoids do not significantly change the model spectrum.

5 Conclusion

The multilayer model of skin and pathologies using fluorophores (melanin, carotenoids, flavins, bilirubin and lipofuscin) was proposed. The fluorophores were matched with an excitation wavelength of 450 nm.
Model AF spectra of healthy skin and neoplasms were obtained. Because of the large number of simulation events (each count on the abscissa axis is essentially an independent source of fluorescence), the number of points in the model spectrum (540-715 nm) was limited. Thus, the analysis of the AF spectrum was carried out in specific positions with a step of 25 nm. For the considered positions, the intensities difference for the model spectra of the “malignant melanoma” and the normal skin had a good qualitative agreement with the experimental results. Higher values of intensities were obtained for the malignant formations in the long-wavelength region of the spectrum (550-640 nm) which are characteristic for squamous cell carcinoma. The presence of characteristic peaks in the model spectrum is primarily determined by flavins and lipopigments. And an increased concentration of lipopigments may indicate the pathological changes.

Disclosures

The author declares that there is no conflict of interests in this paper.

Acknowledgments

This research was supported by the Ministry of Education and Science of the Russian Federation.